ELECTROMAGNETIC ENERGY COUPLED TO NANOMATERIAL COMPOSITES FOR POLYMER MANUFACTURING

A Dissertation

by

CHARLES BRANDON SWEENEY

Submitted to the Office of Graduate and Professional Studies of
Texas A&M University
in partial fulfillment of the requirements for the degree of

DOCTOR OF PHILOSOPHY

Chair of Committee,	Micah J. Green
Committee Members,	Mohammad Naraghi
	James E. Harris
	Mustafa Akbulut
Head of Department,	Ibrahim Karaman

May 2018

Major Subject: Materials Science and Engineering

ABSTRACT

Polymer nano-composites may be engineered with specific electrical properties to achieve good coupling with electromagnetic energy sources. This enables a wide range of novel processing techniques where controlling the precise thermal profile is critical. Composite materials were characterized with a variety of electrical and thermographic analysis methods to capture their response to electromagnetic energy. COMSOL finite element analysis software was used to model the electric fields and resultant thermal profiles in selected samples. Applications of this technology are demonstrated, including the use of microwave and radio frequency energy to thermally weld the interfaces of 3D printed parts together for increased interlayer (Z) strength. We also demonstrate the ability to bond various substrates with carbon nanotube/epoxy composite adhesives using radio frequency electromagnetic heating to rapidly cure the adhesive interface. The results of this work include 3D printed parts with mechanical properties equal to injection molded samples, and RF bonded joints cured 40% faster than traditional oven curing.

DEDICATION

To my wife Lauren, my parents, brother, and grandfather. Thank you for loving and supporting me all these years. To God be the Glory forever and ever! Amen.

ACKNOWLEDGMENTS

First I would like the thank God, the creator of all things and the giver of wisdom: "The fear of the Lord is the beginning of knowledge..." Proverbs 1:7.

I would like to thank my dissertation advisor Dr. Micah Green, his constant guidance in both academic and personal matters has been a blessing throughout my graduate studies. Special thanks to Dr. Mohammad Saed for his patience in teaching me the principles of electromagnetism and microwave engineering. I would like to thank my dissertation committee including Dr. James Harris, Dr. Mohammad Naraghi, and Dr. Mustafa Akbulut, for their advice and guidance in assembling my dissertation and for graciously giving of their time to serve on my committee. I am grateful to Dr. Merid Haile, Dr. Jamie Grunlan, Dr. David Staack, Matthew Burnette, and Jacob Gruener for their help in collecting and reporting data for this dissertation. To those who came before me: Dr. Fahmida Irin, Dr. Dorsa Parviz, Rozana Bari, and Dr. Yueyi Xu, thank you for training me and going out of your way to make me feel welcome in the Green group. Thank you to my fellow colleagues in the Green group: Dr. Wanmei Sun, Smit Shah, Touseef Habib, and Martin Pospisil for helping me solve COMSOL problems. To the wonderfully talented undergraduates who helped collect much of the data in this work: Rob Fullerton, Shane Metzler, Matthew Hansen, Chris Klaassen, Francis Atore, Blake Lackey, Victoria Hicks, Thomas Achee, Aaron Moran, and Alex Strasser, thank you for your time and dedication. Thanks also to our study group: Dr. Blake Teipel, Dr. Kevin Holder, and Dr. Luke Johnson for helping me make it through the MSEN core courses.

Many thanks to my classmate, cofounder, and friend Dr. Blake Teipel for helping me endure grad school and mentoring me to become an entrepreneur. To my Essentium and TriFusion family: Dr. Blake Teipel, Dr. Elisa Teipel, Ryan Vano, Gene Birdwell,

Steve Birdwell, Bryan Zahner, Alden Warr, Josh Lawson, Alex Stockton, Kylen Perry, Garrett Harmon, Shannon Hazel, Rosemary Guzman, Tyllen Bicakcic, Leon Coe, Devaraj Gopalakrishnan, Iris Gisey Euan Waldestrand, Samuel Hager, John McNaughton, Kevin Holder, Nirup Nagabandi, and Rance Dollahite, thank you all for your hard work and dedication to making FlashFuse technology and TriFusion Devices a reality. I pray that our collective efforts will be light in the darkness, and a blessing to those in need.

I am very grateful to my friends and mentors at Startup Aggieland and the Texas A&M McFerrin Center for Entrepreneurship including professors Don Lewis and Richard Lester, Shelly Brenckman, Blake Petty, and Chris Westfall for pouring their time and energy into team TriFusion.

CONTRIBUTORS AND FUNDING SOURCES

Contributors

This work was supported by a dissertation committee consisting of Professors Micah Green, James Harris, and Mustafa Akbulut of the Artie McFerrin Department of Chemical Engineering, as well as Professor Mohammad Naraghi of the Department of Aerospace Engineering

The microwave and radio frequency data analyzed for Chapters 2 and 3 were provided by Professor Mohammad Saed in the Department of Electrical & Computer Engineering at Texas Tech University. The plasma data and analysis collected in Chapter 4 were provided by Professor David Staack and Matthew Burnette. The mechanical data on 3D printed samples in Chapter 4 was provided by the staff engineers at Essentium Materials LLC. The layer-by-layer samples and analysis in Appendix A were contributed by Professor Jamie Grunlan and Dr. Merid Haile. Appendix A appeared in the dissertation of Dr. Merid Haile; Brandon and Merid contributed equally to the work as co-first authors. All other work conducted for the dissertation was completed by the student independently.

Funding Sources

Graduate study was supported by a research assistantship from Texas A&M University This material is based on work supported by the U.S. NSF (CMMI-1561988) and by the U.S. Army Research Office (contract/grant W911NF-15-1-0039).

NOMENCLATURE

3D	Three-Dimensional
AuNP	Gold nanoparticle(s)
AgNP	Silver nanoparticle(s)
BAAM	Big Area Additive Manufacturing
CF	Carbon fiber(s)
CNC	Computer Numerical Control mill
CNT	Carbon Nanotube
COMSOL	Finite element multi-physics modeling software
dB	Decibel
DBD	Dielectric Barrier Discharge
DCB	Double cantilever beam
EPD	Electrophoretic deposition
FLIR	Forward-Looking Infrared camera (FLIR Inc.)
GHz	Gigahertz frequency
Hz	Hertz
LbL	Layer-by-Layer film deposition
LIRF	Locally-Induced Radio Frequency (welding)
MATLAB	Numerical computing environment by MathWorks
ME	Material Extrusion
MHz	Megahertz

MWCNT	Multi-Walled Carbon Nanotube
NIR	Near infrared
NMNP	Noble Metal Nanoparticles
PEG	Polyethyleneglycol
PEO	Polyethylene oxide
PID	ProportionalIntegralDerivative controller
PLA	Poly-Lactic acid (polylactide)
PMMA	Poly-methyl methacrylate
PVA	Polyvinyl alcohol
RF	Radio Frequency
SEM	Scanning Electron Microscope
SENB	Single edge notch bend
SMP	Shape Memory Polymer
SPR	Surface Plasmon Resonance
SWCNT	Single-Walled Carbon Nanotube
Tg	glass transition temperature
WT%	Weight Percent
XPS	X-ray Photoelectron Spectroscopy

TABLE OF CONTENTS

Page

LIST OF FIGURES

FIGURE Page

LIST OF TABLES

TABLE Page

1. INTRODUCTION

1.1 Thermal processing of polymers

Thermal-processing of materials is an important field for the manufacturing industry sector. Virtually all materials used in consumer or industrial products underwent some form of heating to set the final form and function of the object. Polymers and polymer composites, especially thermoplastics, require heating to shape and form feedstock into useful products [1]. Electrical energy, either direct or indirect, is almost exclusively used as the power source to process polymers. Two primary heating methods are implemented for thermoplastic processing: electrical resistance heating, and viscous heating [2]. Viscous heating of polymers involves converting mechanical energy, commonly in the form of rotational shear forces or vibrational shear, into thermal energy due to viscous heating losses. Extrusion molding, friction welding, vibration welding, and ultrasonic welding are all examples of viscous mechanical heating. Resistive (Joule) heating elements in the form of barrel heating cartridges and band heaters are used for extrusion and injection molding technologies as well as compression molding. Infrared lamps are extensively used for thermoforming applications. Serpentine resistance heating pads and ovens are used to cure thermosetting adhesives and fiber-reinforced composite structures.

1.2 New challenges in polymer processing: 3D printing interlayer adhesion

Recently, with the advent of additive manufacturing, new methods are being devised to process and fabricate polymer structures. Fused-deposition modeling^{TM} (FDM) or material extrusion (ME) 3D printing typically relies on a resistance cartridge or sleeve heater to liquefy a polymer feedstock filament for extrusion deposition [3, 4]. Interestingly, exotic heating methods using lasers or electron beams have been developed for powder bed fusion 3D printing technologies [5]. (One notable exception to the common thermal processing

techniques is stereolithography 3D printing which chemically polymerizes a photocurable resin when exposed to an ultraviolet light source) [6].

Additive manufacturing of thermoplastics pose a unique challenge for both the thermodynamics associated with heating the feedstock, and the kinetics of bonding the polymer interfaces. These challenges manifest a common engineering problem, 3D printed parts must be heated for sufficient time to allow for polymer diffusion and welding across the interface, and yet not disturb the form and dimensional tolerances of the part. These divergent process stipulations have resulted in a longstanding problem of weak interlayer bonding strength, commonly referred to as the "Z strength" problem [7].

The most effective way to model the mechanical properties of 3D printed ME parts is the micromechanics approach. In this method, the material bulk properties are defined from the constituent properties of a representative unit cell.

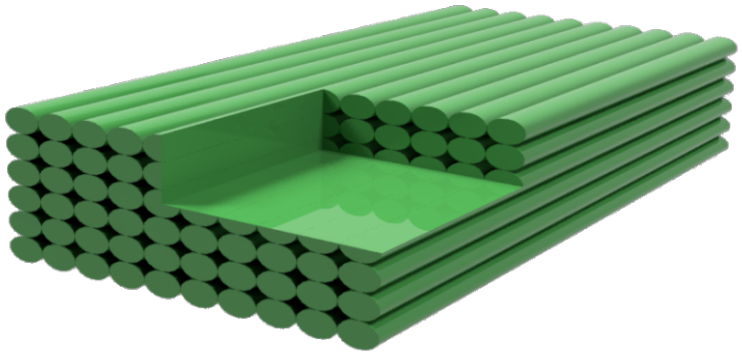

Figure 1.1: Unit cell of a material extrusion (ME) 3D printed part. This represents the most basic unit cell for which orthotropic properties may be measured.

For ME parts the simplest case of this unit cell block is a bundle of ME fibers aligned in the X direction (Figure 1.1). This unit cell bundle is recognized as having orthotropic

mechanical properties, that is, three orthogonal planes of symmetry. These three planes in the X, Y, and Z directions represent the mechanical properties of the extruded fiber, in-plane X-Y bonding, and out-of-plane Z bonding respectively. To evaluate the three principle mechanical properties of this unit cell, test samples may be printed with their tensile axis aligned in the X, Y and Z directions.

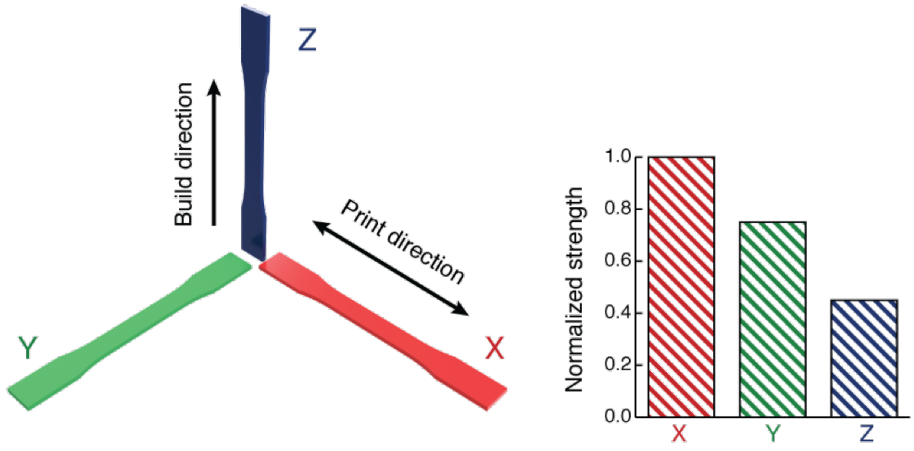

Figure 1.2: Tensile samples aligned in the three principle build directions (left). Mechanical properties typically associated with the three directions (right).

1.2.1 Polymer welding kinetics

Much work has been done to model the polymer welding process at the interfaces of 3D printed parts. From a historical perspective, Kim and Wool developed much of the theoretical background for the isothermal welding (healing) of polymer interfaces [8]. Using the reptation model of polymer motion from De Gennes, they describe four steps in the polymer crack healing process: surface rearrangement, surface approach, wetting, diffusion, and randomization [9]. In the context of 3D printing, the last three steps: wetting of the polymer interface, diffusion of polymer chains across the interface, and randomization

of the resulting polymer entanglements, are most relevant during the extrusion of the hot polymer bead onto a cool layer below it.

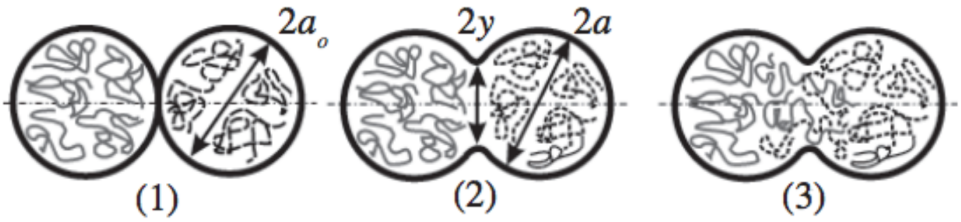

Figure 1.3: Bond formation between polymer traces. Reprinted from Journal of Manufacturing Processes, 6/2, Bellehumeur, C., Li, L., Sun, Q., & Gu, P., Modeling of Bond Formation Between Polymer Filaments in the Fused Deposition Modeling Process, 170-178, Copyright (2004), with permission from Elsevier

Perhaps the earliest report of the Wool model applied to ME printing is by Sun and Bellehumeur [10]. In their report, they accounted for the heat transfer mechanisms associated with a hot polymer bead heating the layers below it and in turn being cooled by the previously deposited layer. Experimentally, they conducted polymer sintering experiments on ABS to determine dimensionless neck growth profiles between the polymer particles.

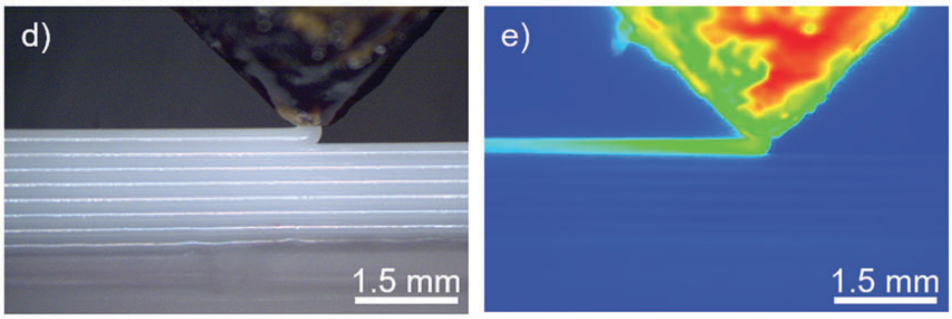

Figure 1.4: FLIR thermography image of a 3D printed layer being deposited. Reproduced from [11] with permission of The Royal Society of Chemistry

More recently, Seppala and Migler at NIST have greatly expanded on these models by performing *in-situ* thermography of the 3D printed layers while they are being deposited (Figure 1.4), determining equivalent weld times using rheology data and time-temperature superposition shift factors, and correlating these models to measurements of interlayer fracture strength [11].

1.2.2 Interlayer fracture strength tests

As shown by Seppala and Migler, it is important to couple and verify theoretical models of polymer welding to measurements of interlayer strength. That said, there is no single unified standard for measuring interlayer properties of ME 3D printed parts. The most straight-forward technique which is easily compared to industry-standard mechanical tests is uniaxial tensile tests of dogbone samples [12]. There are however several problems with this technique as related to ME 3D printed samples. First, tensile data is usually compared against injection molded or sheet-cut tensile bars which have been prepared to minimize surface flaws. 3D printed samples by nature contain many thousands of sharp interfaces between adjacent filament traces, both intra-layer (same XY plane) and inter-layer (Z-direction interfaces). Perhaps the most repeatable way to make tensile specimens is to print a standard coupon of material, then route out the desired dogbone shape with a CNC mill. Second, tensile strength is predominately governed by fracture mechanics and critical flaws within a material. With 3D printed parts where the interface is not fully welded, the tensile strength will be limited by the stochastic collection of welds, with the weakest weld being "the weakest link in the chain". Thus tensile samples are not a true predictor of inter-laminar fracture behavior, but rather the collective behavior of many welds. To address this issue, three fracture-specific tests have been proposed and studied recently for 3D printed parts: Mode III (trouser tear) [13], single edge notch bend (SENB) [14], and double cantilever beam (DCB) [15].

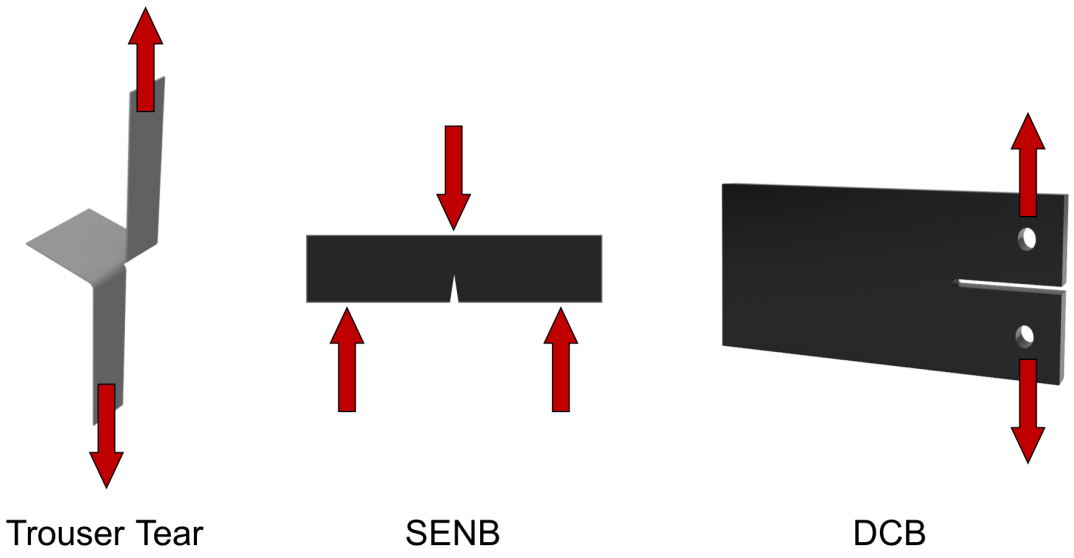

Figure 1.5: Three fracture test methods: trouser tear (left), single edge notch bend (SENB (middle), double cantilever beam (DCB) (right)

A common issue faced by all mechanical tests, is the absence of a standard print profile, raster pattern, nozzle diameter, print temperature or printer platform, with which to compare mechanical samples against. For this reason, most mechanical data is only useful for making relative comparisons between specimens of the same sample set in a particular study. Caution should be used when comparing data from separate studies and samples printed with different parameters.

1.2.3 Process optimization for 3D printed parts

In spite of the difficulties of measuring the mechanical properties of 3D printed parts, great efforts have been made both commercially and in academic settings to optimize the performance of 3D printed parts [16, 17, 18, 19, 20]. Most notably, Stratasys Inc. has gone to great lengths to control print settings, feedstock material, and the print chamber environment in order to achieve consistent performance in parts printed on their machines. In-fact,

most early academic studies on the mechanical properties of FDM printed parts were performed on a Stratasys machine. As open-source 3D printers have become more common, there has been renewed interest in analyzing and optimizing the mechanical performance of 3D printed parts. In spite of the heroic efforts to perfect process settings, only minor improvements in mechanical properties have been gained with such techniques. Developing universal process settings for isotropic mechanical perfomance remains a sisyphean task.

1.2.4 Non-traditional methods for improving strength

It is clear that traditional thermal control and process optimization approaches to solving the interlayer bonding problem can only yield incremental improvements in strength. Even if an optimized set of printing parameters were found for a certain part geometry, those parameters would be part, process, and material specific. One of the major benefits of 3D printing is the flexibility to print one-off bespoke parts; optimized print settings for one-off parts would require complex computational predictive models that do not yet exist. In response to this conundrum, many research and commercial solutions have been proposed and studied to solve the Z-strength problem in a non-traditional manner. The following techniques generally fall outside the scope of the traditional temperature and processing control techniques discussed above.

Most of the attempts to increase part strength fall into several major categories: layer preheating, annealing, mechanical mixing, surface modification, adhesives, and combinations thereof. The first instance of a layer pre-heating technique was reported by Partain [21]. For this system a forced air polymer welding kit was mounted to the 3D printer next to the nozzle. The goal was to raise the temperature of the polymer bead just ahead of the nozzle to above the “critical sintering temperature”, loosely defined as the glass transition temperature (Tg) for amorphous polymers. Another requirement imposed was

that the heat source should be non-contact so as not to disturb the surface finish of the part. The forced air however, was found to overheat or blow the printed part too much which resulted in poor mechanical properties. This idea was expanded on by Keng Hsu at Arizona State [22]. Instead of a forced air heater, they used an infrared laser to preheat the polymer trace ahead of the print nozzle. By carefully controlling the laser power, they were able to increase the interlayer bond strength by 50% compared to a control sample. This result highlights the aforementioned thermodynamic problem i.e. the previous bond line should be above the polymer Tg, and remain above the Tg for sufficient time to weld the interface, and yet the part as a whole cannot remain at these conditions else it would deform. The laser approach demonstrates an effective solution to the problem, however the ability to control a laser in real time for arbitrary shapes remains a daunting task. This concept was applied in a simplified, yet larger format by researchers at Oak Ridge National Labs for use in the Big Area Additive Manufacturing (BAAM) system [23]. Kishore *et al.* similarly saw improvements in interlayer fracture strength by preheating the deposition layer to above the Tg with a large infrared lamp. Both infrared heating techniques relied on the tenuous control of the infrared energy, as power levels too high resulted in polymer degradation and a subsequent decrease in mechanical properties.

Other non-thermal techniques to improve interlayer adhesion have been proposed and tested. An interesting method developed by Lind *et al.* at Oak Ridge National Labs is "Z-tamping" for the BAAM system [24]. They use an air cooled plate reciprocating at 20 Hz to tamp the extruded layers as they are being deposited. Although no data on the Z strength was reported for the tamping technique, the Y axis strength was reported to double with addition of the tamping technique.

In addition to thermal and mechanical bonding methods, chemistry and adhesion related approaches have been used to enhance the Z strength. Perhaps the simplest method reported is the concept of back-filling a 3D printed shell with a cross-linked thermoset

polymer [25]. This approach however involves complicated post-processing steps and resembles injection molding or resin transfer molding rather than a practical 3D printing process. Rize Inc. has reported a hybrid technique involving a thermoplastic extrusion head in conjunction with a polymer jetting head. This machine is able to deposit an epoxy adhesive layer between successive thermoplastic 3D printed layers to increase the interlayer bond strength.

Researchers from Kyushu Institute of Technology in Japan reported a method for surface treating 3D printed layers with an atmospheric glow-discharge plasma [26]. Such a technique appears quite promising as plasma surface treatment is a scientifically proven and widely used method for preparing polymer parts to be bonded [27]. Despite the theoretical improvements plasma treatments may have on 3D printed parts, the results for polylactide (PLA) indicate only minor improvements in the Z-strength. This may be due to insufficient treatment time or conditions, or perhaps PLA has favorable surface energy suitable for bonding and thermal considerations dominate the welding process. Larger improvements may be possible for polymers with low surface energy such as polyolefins, rigid backbone polymers, and halogenated polymers.

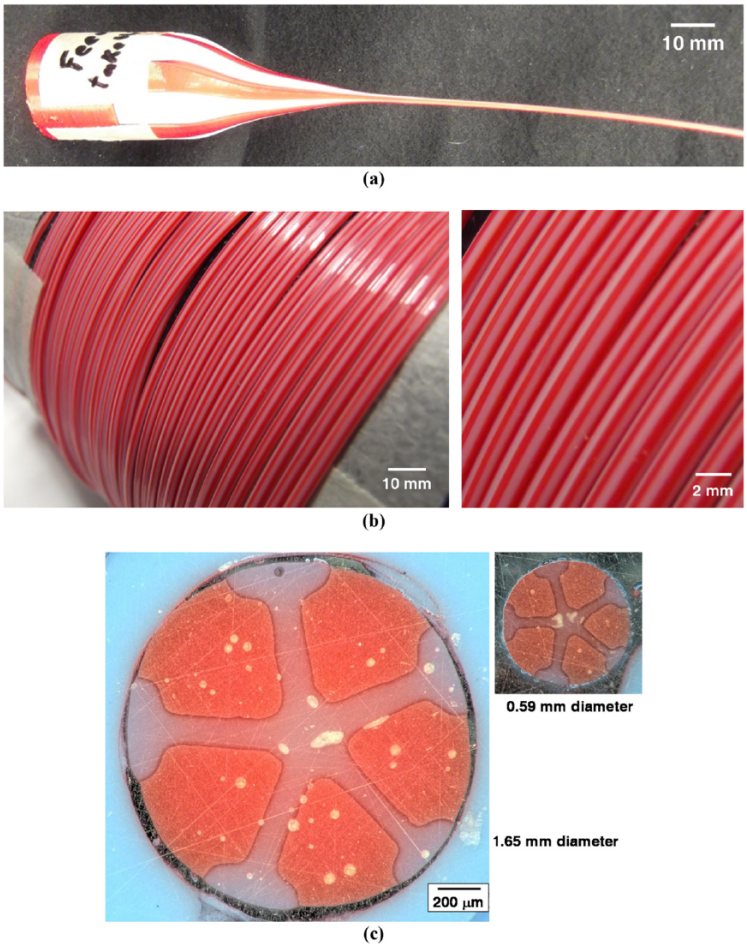

Figure 1.6: Heterogeneous polymer preform drawn into a thermoplastic filament. Extensional flow enables the initial cross-section composition to remain in-tact upon thinning of the structure. Reprinted from Additive Manufacturing,16, P.M. Toal Jr *et al.*, Microstructured monofilament via thermal drawing of additively manufactured preforms, 12-23, Copyright (2017) with permission from Elsevier

A final non-traditional method proposed for bonding the interfaces of 3D printed parts without causing dimensional warping is the use of heterogeneous filament feedstock. Stratasys Inc. first reported a core-shell filament feedstock for semi-crystalline polymers consisting of a shell with a lower melting point polymer than the core [28]. In the context of the patent this method was primarily meant to solve dimensional warping issues

associated with the non-linear volume changes in semi-crystalline polymers as they cool. The concept of a heterogeneous polymer feedstock filament for 3D printed parts was expanded upon by researchers at the Army Research Labs [29]. By 3D printing preform cylinders with complex cross-sectional shapes, they were able to fiber draw the preform down into filament for a 3D printer (Figure 1.6). Such a method with "candy cane" stripes of polymers with different Tg's or melting points may be useful for improving the Z-layer strength following a post-treatment in an oven; however no results on such a study have been reported to date.

While each of these non-traditional techniques have demonstrated some level of improvement or at least proof-of-concept to solve the Z strength problem, none have reported isotropic strength properties for a range of engineering-grade materials at a technology readiness level suited for commercial adoption. A large portion of this work will focus on our method to address the Z-strength problem in 3D printed parts. We do this by locally targeting the interface of the printed part by embedding an electrically-responsive nanomaterial as a coating on 3D printer filament, and applying an electromagnetic field to heat and weld the interface together. In order to control this heating effect, a high degree of knowledge about the material's response to electromagnetic energy is necessary.

1.3 Electromagnetic heating of nanocomposites

1.3.1 Carbon allotropes as susceptors

Polymers are commonly heated with electric resistance type heaters for processing. In this case the polymer is indirectly heated by conduction or radiation of the resistive heating element. Polymers however, are poor thermal conductors, which makes these methods difficult to control for certain applications (i.e. 3D printing). There are many scenarios where having more precise control over the thermal processing conditions of polymers are desirable. One such method for achieving more control is the concept of energy cou-

pled to matter, a termed coined by research directors at the Army Research Laboratory [30]. This concept is highly applicable to polymer and polymer composite materials which are susceptible-to and couple directly with electromagnetic energy. Most non-conducting polymers only have absorptions close to infrared wavelengths where penetration depths are short. Notable exceptions are polar polymers such as polyvinyl chloride (PVC) which have significant dipole interactions and thus losses at microwave frequencies. The bulk majority of polymers however are electrical insulators with good dielectric properties and very low losses across the electromagnetic spectrum. Polymer composites, especially nanocomposites containing electromagnetic susceptor materials are very attractive for energy coupled to matter processing techniques.

Since neat polymers do not typically absorb electromagnetic energy below terahertz frequencies, the selection of appropriate broad-band electromagnetic susceptor materials is critical. Carbon-based susceptors are excellent candidates because of their availability and common use as additives for plastics and composites. Carbon fibers, graphite, and carbon black have been used as additives and mechanical reinforcements for plastics for over a century. More recently, carbon nanomaterials including carbon nanotubes (CNTs) and graphene have attracted much attention because of their effectiveness at low concentrations. The primary benefits realized by these nanomaterials comes from their intrinsic extraordinary thermal and electrical properties as well as excellent mechanical properties. The high aspect ratio of these materials combined with their intrinsic properties, results in novel composite materials at low percolation thresholds.

Many models exist for the complex electrical behavior displayed by composites consisting of conductive fillers and dielectric matrices. One must decide the detail at which length-scale is necessary to account for the observed macroscopic behavior. In the low frequency limit, i.e. direct current electric fields, the behavior of composites is most often described in terms of the percolation behavior. Percolation is achieved when loading levels

of the conductive filler are high enough to achieve a continuous conductive pathway from one point to another in the sample.

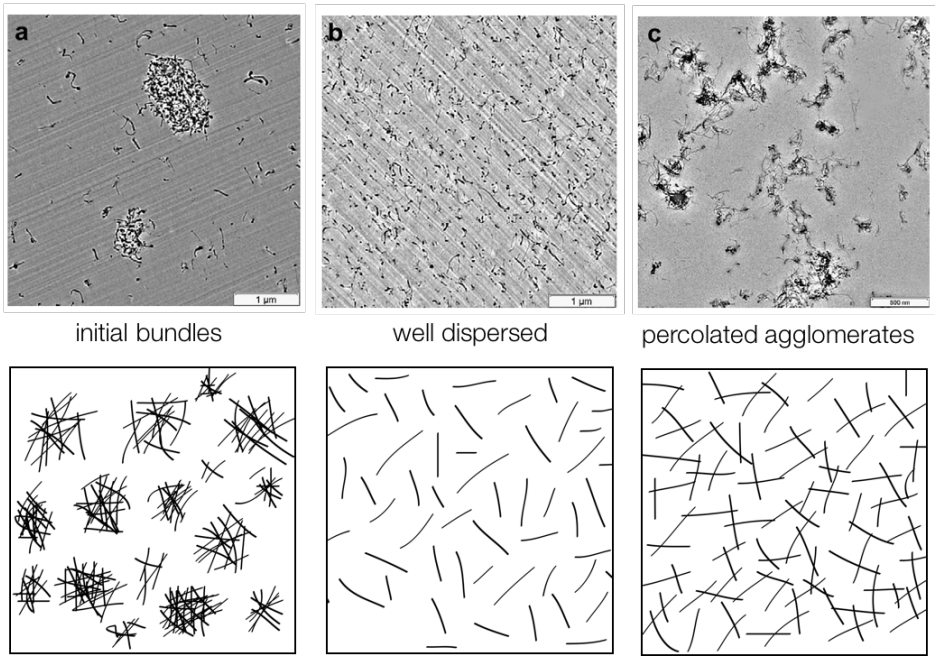

Figure 1.7: States of a CNT nanocomposite dispersion: initial bundles indicative of poor dispersion (left), well dispersed CNTs but isolated with a low electrical conductivity (middle), secondary agglomerates which force an artificially low percolation threshold (right). TEM images reprinted from Polymer, 53/1, S. Pegel *et al.*, Establishment, morphology and properties of carbon nanotube networks in polymer melts, 4-28, Copyright (2008) with permission from Elsevier

Below the percolation threshold the composite generally exhibits the electrical resistivity (inverse conductivity) of the host matrix. Well above the percolation threshold the conductivity generally tends towards the bulk conductivity of the filler. At the percolation threshold, a transition occurs as particle-to-particle interactions become significant enough to allow for electron hopping or tunneling. Percolation is highly dependent on the filler loading level, the geometry, especially the aspect ratio, as well as the dispersion state and

intrinsic electrical properties of the filler and matrix. Both carbon nanotubes and graphene fillers have attracted great attention in the past decade due to their extraordinarily low percolation values.

1.3.2 Differences between DC and AC heating

In the context of Joule heating, significant differences exist between direct current and alternating current electric fields. Direct current Joule heating requires the composite to be directly connected to the power supply with conductive electrodes. For loading levels at or below the percolation threshold it can be difficult to couple a DC source to the composite load at reasonable voltages. For instance, a 0.1wt% carbon nanotube polymer composite with a DC conductivity of $1x10^{-9}$ S/m would require an electric field many orders of magnitude greater than its dielectric breakdown strength to produce a current density significant enough to heat it.

On the other hand, alternating current Joule heating affords much greater flexibility over the electric field application method and the frequency parameters. Both direct electrode contact and non-contact methods are viable for heating susceptible composites. Non-contact heating is especially useful in situations where buried interfaces, discrete domains, and complex geometries need to be heated. Moreover, AC heating, especially in the radio frequency and microwave bands, enables a much wider range of composite loading levels and dispersion states to be coupled to the source due to capacitive effects.

The frequency-dependent response of composites is markedly different from the static field behavior, owing primarily to the capacitive-coupling of the discrete conductive elements making up the percolating network. Non-conducting inter-particle gaps that are too large to tunnel electrons, will instead behave like a vast array of capacitors which can pass significant current densities through the volume of the composite at high enough frequencies. The effective overall conductivity is a combination of the static, frequency-

independent conductivity, and the frequency-dependent capacitive conductivity. The transition from the DC conductivity behavior to the frequency-dependent AC conductivity at a given frequency value is referred to as the crossover frequency. The crossover frequency generally increases with increasing loading levels of conductive filler [31].

1.3.3 Considerations for coupling electromagnetic energy to composites

Two primary benefits of electromagnetic heating of susceptible composites are explored in this field of study: targeted heating and volumetric heating. The concept of targeted heating is particularly relevant in the context of polymer bonding or welding. By specifically placing susceptors within discrete locations of a non-absorbing medium, one may precisely target regions to be heated upon the application of electromagnetic energy. This technique has been used to bond thermoplastic microfluidic devices, pipes, and films. One of the primary advantages of targeted heating is to rapidly raise the temperature of buried interfaces so that polymer bonding may be achieved without thermally warping or degrading the bulk components to be joined. The other primary benefit realized by electromagnetically heating composites is volumetric heating. In contrast to conduction or convective heating methods, electromagnetic heating enables the entire volume of a composite to be heated uniformly. This is particularly useful when polymer parts having relatively thick cross sections need to be processed. The most common analogy would be the difference in cooking time of a potato in an oven vs. a microwave.

Several factors should be considered for electromagnetic heating of susceptible composites. The first consideration is efficiently coupling the electromagnetic source to the load, commonly defined as impedance matching [32]. The next consideration is on the uniformity of heating based on the electromagnetic frequency used, the applicator configuration and thus electric field applied to the composite part. For volumetric heating, the penetration depth of the applied electric field or electromagnetic wave should be consid-

ered. In all cases, there are constraints that must be taken into consideration. First and foremost, AC heating equipment (signal generator, amplifier, matching network, etc.) is generally more expensive than a DC counterpart due in part to the simplicity of DC power equipment. Notable exceptions are household microwave ovens which can output over 1kW for less than $100 in capital equipment. Other limitations include heating uniformity and penetration depth with microwave frequencies, complex adaptive impedance matching networks for radio frequencies, shielding requirements for both sensitive electronics as well as biological health and safety. It is important to note, that although electromagnetic energy in the RF (<100 GHz) spectrum is non-ionizing radiation, significant safety hazards do still exist including excessive heating of susceptible human tissues, localized cauterization and burns, and electrical shock. Nonetheless, when used appropriately, electromagnetic heating of composite materials unleashes many exciting novel techniques for material processing.

1.3.4 Electromagnetic heating of noble metal nanoparticles

The ability to couple electromagnetic energy to appropriately tuned nanoparticles affords unique opportunities for thermally manipulating matter. Particularly, photothermal heating of noble metal nanoparticles (NMNPs) has shown very promising applications in multiple scientific disciplines. This section aims to introduce the fundamental physics responsible for this phenomenon and summarize the novel applications of the photothermal effect in literature. Special emphasis will be placed on biomedical and polymer heating applications. Future directions for research are proposed in the area of localized photothermal healing of polymer interfaces by swelling induced intimate contact pressures.

1.3.4.1 Fundamental physics

Perhaps one of the most promising developments in materials science in the past century has been the discovery, characterization, and applications of nanoparticles. The study

of nanotechnology primarily deals with particles or structures, which have at least one dimension below 100 nanometers (nm). When reduced to such small dimensions, nanoparticles begin to exhibit properties that deviate from those of the bulk constituent element(s). This is largely due to the confinement of possible quantum states for electrons and phonons in the particle, as well as surface area effects which dominate over bulk properties [33]. Metallic nanoparticles and specifically noble metal nanoparticles (NMNPs) have been studied extensively due to their wide range of applications, ease of synthesis, and stability against oxidation or corrosion. In this context, noble metals are defined elementally as silver, gold, platinum, ruthenium, rhodium, palladium, osmium, and iridium. Out of these, silver and gold dominate the literature in terms of their use, with gold being the most common.

Several popular routes for synthesizing noble metal nanoparticles exist. Considerations for the synthesis of these nanoparticles include the ability to control size and morphology with precision, since obtaining a narrow size distribution is desirable. Size and shape are important for the purposes of controlling the optical properties of the nanoparticles and in turn the photothermal response to a specific illumination frequency [34]. The selected method should be repeatable given the same synthesis conditions so that consistency in future experiments may be obtained. It is desirable to use methods that are scalable and environmentally friendly so that industrial production of selected nanoparticles is feasible.

1.3.4.2 Surface plasmon resonance (SPR)

Of all the peculiar properties of NMNPs, their interaction with electromagnetic energy, particularly light, is perhaps most interesting. Common sense would suggest that the yellow luster of gold or the white flash of silver and platinum is a property inherent of the element itself and remains unchangeable. It is however, possible to produce brilliant colors of various tones simply by producing nano-sized particles of these noble metals.

Although the mechanism was not understood at the time, this phenomenon has been exploited for centuries by glassmakers who could obtain crimson and ruby red colors with the addition of gold salts. It is now well known that this coloration is a result of surface plasmon resonance (SPR), which is a polarization of the conduction electrons in the NMNPs [35]. From fundamental physics we know that light is both a particle and a wave, if treated as a wave it is characterized by its frequency, wavelength, speed, and polarization. When light interacts with a NMNP, the alternating electric field causes a displacement of the outer conduction electrons relative to the collective atomic nuclei. The electron cloud then oscillates in a coherent manner due to the linear restoring force of the Columbic attraction between electrons and nuclei in the NMNP [36]. It is important to note that SPR is not a quantum effect in the same way that quantum dots made with semiconductor materials behave; instead, it is a surface effect that may be treated with classical Maxwell electromagnetics equations [37].

A result of the NMNPs SPR response to light is an intense optical absorption peak, which may be tuned by controlling the properties of the particle and the medium in which it resides. Although many crystallographic morphologies of NMNPs have been synthesized, the most commonly researched are spheres, cubes, octahedra, tetrahedra, rectangular prisms, octagonal rods, right bipyramids, decahedra, icosahedra, pentagonally twinned rods and wires, triangular and hexagonal plates [34]. Complex geometries including hollow porous nanocages and hybrid structures, such as nanoshells, have been exploited for more precise control over optical properties [38, 39]. With these variations in geometry come a host of complex optical modes. In general it is recognized that electric fields will be maximized at sharp corners, such as the corners of a pyramid [40]. This enhanced electric field causes surface charges to accumulate at the corners, reducing the Columbic linear restoring force, which creates a bathochromic shift in the optical absorbance. Xia et. al. have simulated the spectral response of various silver particle geometries using Mie and

discrete dipole approximation theories [34]. The overall extinction spectra and ensuing observed color of the NMNP, is a combination of both the absorption and scattering of incident photons.

Size plays an important role in the optical absorption spectra of NMNPs. As the particle size is increased, a bathochromic (red) shift is observed, along with an increase in the bandwidth of the peak absorption wavelength [37]. Contrariwise, a decrease in the particle size leads to a hypsochromic (blue) shift and sharpening of the absorption peak. For one-dimensional NMNPs including nanobars, rectangular prisms, and nanowires, two optical modes exist: transverse and longitudinal. The dual plasmon band of 1D NMNPs arises from the split resonant harmonic modes formed as the electron cloud is polarized normal and orthogonal to the particle axis. Optical properties of these 1D particles may be controlled by tailoring their aspect ratio, with higher aspect ratios corresponding to greater bathochromic shifts [40].

An interesting technique for engineering the optical properties of NMNPs is to create nanoparticles with thin surfaces. Three techniques for this approach have been demonstrated: nanoshells, nanomatryoshkas, and nanocages. Nanoshells consist of a dielectric core (i.e. silica) and a thin conformal coating of a noble metal, usually gold. Halas et. al. demonstrated that by controlling the core-to-shell thickness ratio the peak optical absorption could be tuned from the visible end of the spectrum far into the near infrared (NIR) region, opening many applications in the biological sciences where infrared excitation is desirable [41]. Similar to nanoshells, nanomatryoshkas are concentric jawbreaker-like structures consisting of alternating layers of noble metals and dielectrics. Hogan and Halas have found that nanoshells are more likely to scatter incident light whereas nanomatryoshkas are more effective at absorbing incident photon flux [42]. This difference could potentially be exploited to allow for imaging applications or heating applications respectively. The other popular approach for tailoring the optical response of NMNPs is to create

a hollow nanocage [38]. The primary benefit of this nanocage structure is the ability to tune the absorption peak in the ideal NIR range while keeping all particle dimensions below 50nm. Li et. al. noted that due to the unique structure and high absorption cross section, the same therapeutic treatment of cancer cells was possible at far less laser radiation intensity levels.

1.3.4.3 Photothermal effect

As a result of their extraordinary light absorption efficiency, NMNPs posses the ability to act as nanoscale heaters. With this localized control of heat generation comes a host of unique and stimulating applications. Link and El-Sayed were early investigators of this phenomenon and were largely responsible for coining the heating effect as a photothermal response [43]. They later discovered that by using pump-probe femtosecond laser pulses to heat gold nanorods, they could observe a bleaching effect in the transient spectral response [44]. This offered insights about the photon-electron cloud interactions, as well as the phonon-phonon relaxation process. Experimentally, they used a 400nm laser with 100 fs pulses to irradiate a solution of gold nanorods and recorded the time-dependent decay of the photo bleaching. From this measurement they calculated the relaxation time of the various stages of the photothermal heating effect. The first step is the absorption of incident photons resulting from the SPR of the nanorods, as discussed earlier. Following this absorption, the electrons of the nanoparticle become excited and are said to be hot. In a period of 1-4 picoseconds these hot electrons thermally equilibrate their electrodynamic potential energy with the atomic lattice in the form of harmonic phonon potential energy, a process termed electron-phonon relaxation. The final step, and perhaps the most important for photothermal heating applications, is the kinetic transfer of heat to the surrounding host medium. This transfer of energy occurs on the order of 100 picoseconds and is commonly referred to as phonon-phonon relaxation. Interestingly, at high illumination intensities, if

the rate of energy absorbed by the NMNPs is greater than the rate of energy dissipation to the host medium, the particles can undergo phase transformations or even fragment as a result of the rapid local heating [43].

Efforts have been made to analytically define the heat transfer equations governing the temperature rises and thermal heat generated from both single NMNPs and ensembles of multiple scattering NMNP systems. Govorov and Richardson sought to quantify and calculate the time-dependent spatial temperature of AuNPs suspended in ice, using calorimetric experiments coupled with Raman mapping, to determine the local surface temperature during photothermal heating [45]. They validated their findings by applying the elementary one-dimensional heat transfer equation for spherical coordinates with a heat generation term for the incident light in the form:

$$\rho(r)c_p(r)\frac{\partial T(r,t)}{\partial t} = \nabla k(r)\nabla T(r,t) + \langle j(r,t)\cdot E(r,t)\rangle$$

where r is the radial distance from the nanoparticle center, t is time, $T(r,t)$ is the spatial and time-dependent temperature, $\rho(r)$ is the particle mass density as a function of radial distance, $c_p(r)$ is the specific heat at constant pressure as a function of radial distance, $k(r)$ is the thermal conductivity as a function of radial distance, with the final collective term representing the thermal heat source resulting from the photothermal effect where $j(r,t)$ is the time-dependent incident current density as a function of the radial distance, and $E(r,t)$ is the time-dependent electric field interacting with the NMNP. For a single particle, this equation may be solved analytically to yield the following form of the spatial temperature of a NMNP:

$$\Delta T(r) = \frac{V_{NP}Q}{4\pi k_0 r}$$

where V_{NP} is the volume of the NMNP, and k_0 is the thermal conductivity of the host

medium. For an ensemble of particles, it has been shown that collective plasmon resonance effects can amplify the photothermal heating response and create local hot spots in polymer matrices [46]. Hogan and Halas were successful in using a version of the Beer-Lambert law derived from conservation of energy principles solved analytically with Monte Carlo simulations to model multiple scattering and absorption events of NMNPs in solution [42]. Using the results of the Monte Carlo simulations, they calculated the power dissipated in the NMNP solutions and the resultant temperature rise of the host medium and found the results to be in agreement with experiments. This information lays the groundwork for a host of practical applications where localized and intense heating of a nanoscale target volume may be achieved.

1.3.4.4 Applications

Virtually every other accessible bulk heat transfer method relies on surface or volumetric heating by means of conduction, convention, or radiation. Coupling electromagnetic energy to a nanoscale susceptor particle enables discrete domains of matter to be thermally manipulated. With this ability to transfer heat spatially on-demand at the nanoscale, researchers have developed many techniques for biomedical procedures, chemical reactions, and polymer processing. The two primary applications for the photothermal heating of NMNPs in biomedical applications are imaging and hyperthermia. As a result of the SPR effect, it is well known that in comparison to dyes and fluorophores, NMNPs have absorption cross-sections several orders of magnitude greater, and are therefore excellent for diagnostic imaging of biological samples [47, 48, 49, 50]. Beyond imaging, once a NMNP has been grafted or bioconjugated onto a desired host cell, it becomes possible to carry out targeted hyperthermia of a diseased or tumorous region because of the selective accumulation of the NMNPs in the targeted area [48]. Additionally, an intriguing method for healing minimally invasive surgical incisions has been developed by Matteini et. al.

wherein a chitosan film with embedded gold nanorods is heated with a laser and bonds tissue together [51]. This method has resulted in successfully bonding muscular and skin tissue to their bulk tensile strength as well as in vivo sealing of a rabbit carotid artery post incision [52, 53].

1.3.4.5 Polymer heating

In the realm of photothermally heating polymers, two primary applications have been explored; shape memory polymer (SMP) actuation and controlled polymer heating. In both applications the SPR effect has been exploited to gain precise control over the mechanism of localized heating by tuning the incident irradiation frequency and the light polarization. As a result of this control, multidirectional shape memory actuation and anisotropic thermal annealing have been achieved respectively.

Shape memory polymers are a special class of polymers that may be mechanically actuated by stimulated temperature changes. When using NMNPs as the local heating elements, precise control of the actuation may be accomplished by selecting the appropriate frequency of light to stimulate a resonant collection of nanoparticles. Early reports of this technique were documented by West et. al. in their ability to remotely control the flow of a solution at a microfluidic T-junction by shrinking two different light-responsive hydrogel composite actuators [54]. In their method they relied on gold nanoparticles and gold nanoshells with absorption peaks at 532 nm and 832 nm embedded in poly[N-isopro- pylacrylamide-co-acrylamide] hydrogel to act as valves. Upon irradiation at approximately 2 W cm-2, efficient valve actuation of each respective valve was accomplished in under five seconds. Using a similar approach, Sukhishvili et. al. were able to precisely control the morphological shape evolution of photothermally actuated polymer brush films formed using layer-by-layer (LbL) techniques [39]. By grafting the SMP brushes directly to the surface of NMNPs, they achieved unprecedented control over

the anisotropic swelling and actuation of bulk polymer assemblies. Similar to the photothermal control of SMP structures, the processing of thermoplastic polymers has also seen many intriguing practical applications enabled by the illumination of embedded NM-NPs [55, 56, 57, 58, 46, 59, 60, 61, 62, 63]. Govorov et. al. were the first researchers to show that a thin polymer shell consisting of polyethyleneglycol (PEG) could be heated and melted using the photothermal heating of AuNPs [46]. Their work was expanded upon greatly by the Clarke research group at NC State University; specifically for applications in photothermal processing of electrospun polymer fiber mats [55, 56, 62, 63]. Early experiments carried out by Maity and Clarke revealed that selective melting and densification of PEO electrospun mats was possible with illumination intensities as low as 25 mW cm-2; this low intensity was unprecedented considering similar applications in biomedical research requiring intensities 5 orders of magnitude greater [62].

In the same vein of studies described above, several intriguing reports of polymer healing exist in literature. Zhao et. al. led pioneering work on healing PEO and low-density polyethylene (LDPE) films doped with low concentrations of AuNPs [58]. By scanning a 2.2 W cm-2 532 nm laser across a razor-cut PEO film for 10s, they observed that nearly the entire tensile strength was recovered due to melting of the crystalline interfaces and recrystallization across the interfacial width. Observing the sample under a cross-polarizing optical microscope revealed the healed interface morphology, which consisted of a distinct polycrystalline phase with spherulites constrained in size due to the discrete area heated by the laser light [58]. In a follow-up study reported by Zhao, photothermal heating was used to activate both a shape memory effect and a healing process in cross-linked PEO films [64]. It is notable that in their study of the healing process only the laser-induced photothermal heating was successful in repairing the crack, whereas conventional heating in an oven was unsuccessful. This result is remarkable considering the laser healing took only three seconds, in comparison to the unsuccessful oven healing at 140C for 3

minutes. The discrepancy was explained in terms of the shape changes during the heating process; specifically, the oven heating caused the entire sample to expand isotropically, which resulted in the crack pulling away from itself and thus no healing occurred. On the other hand, laser photothermal heating caused a localized expansion just at the crack width, resulting in swelling of the interface alone and mixing of the molten polymer.

Wang et. al. have recently demonstrated a fascinating technique for healing interfaces between carbon fibers (CFs) and the host resin matrix by coating AuNPs on the surface of CFs using electrophoretic deposition (EPD) [61]. By selectively depositing AuNPs on the surface of the fiber rather than dispersing them throughout the polymer matrix, they were able to achieve melting in a nanoscale thin region surrounding the fiber. This resulted in local melting of the poly-methyl methacrylate (PMMA) and concurrent volume expansion of the melt region resulting in compressive forces induced by the radial confinement of the melt by the distal solid PMMA. Confirmation of this analysis by the authors could have been performed by initiating a control sample wherein AuNPs were dispersed in the PMMA matrix and photothermally heated to test the healing behavior. In this manner they could have gained deeper insights about the confined melt swelling process in comparison to melting the entire PMMA matrix surrounding the CF. It is curious that both Zhao and Wang found that selective melting and concurrent swelling in a local region surrounding the healing zone were advantageous for achieving high healing strength. These results of photothermal healing warrant further study for the merit of extraordinary control over polymer physical properties and the ability to selectively heal discrete areas of a polymeric component.

The following chapters focus on locally induced microwave welding of 3D printed parts, radio frequency heating of polymer composites, *in-situ* kilohertz heating of 3D printed parts assisted by a novel asymmetric-resistively coupled dielectric barrier discharge applicator, and microwave heating of polymer/carbon nanotube layer-by-layer thin

films.

2. WELDING OF 3D-PRINTED CARBON NANOTUBEPOLYMER COMPOSITES BY LOCALLY INDUCED MICROWAVE HEATING*

2.1 Overview

Additive manufacturing through material extrusion, often termed three-dimensional (3D) printing, is a burgeoning method for manufacturing thermoplastic components. However, a key obstacle facing 3D-printed plastic parts in engineering applications is the weak weld between successive filament traces, which often leads to delamination and mechanical failure. This is the chief obstacle to the use of thermoplastic additive manufacturing.

We report a novel concept for welding 3D-printed thermoplastic interfaces using intense localized heating of carbon nanotubes (CNTs) by microwave irradiation. The microwave heating of the CNT-polymer composites is a function of CNT percolation, as shown through *in-situ* infrared imaging and simulation. We apply CNT-loaded coatings to a 3D printer filament; after printing, microwave irradiation is shown to improve the weld fracture strength by 275%. These remarkable results open up entirely new design spaces for additive manufacturing and also yield new insight into the coupling between dielectric properties and radio frequency field response for nanomaterial networks.

2.2 Introduction

For typical three-dimensional (3D)printed parts, the extruded filament traces display tensile properties similar to injection-molded samples in the print (x) direction Figure 2.1A. However, the filament traces are aligned orthogonal to the y and z (build) directions such that tensile properties in these directions are limited by the interfacial bonding

*From Sweeney C.B., Lackey B.A., Pospisil M.J., Achee T.C., Hicks V.K., Moran A.G., Teipel B.R., Saed M.A., Green M.J. Welding of 3D-printed carbon nanotubepolymer composites by locally induced microwave heating. Science Advances. 2017 Jun 1;3(6):e1700262. Copyright 2017 American Association for the Advancement of Science. Reprinted with permission from AAAS.

strength of the filaments. Thus, despite additive manufacturings versatility and speed, the mechanical properties of 3D-printed parts currently lag behind those of conventionally manufactured parts. This is one of the principal barriers to widespread adoption of material extrusion (ME) as a means to industrial manufacturing, along with speed and cost [65].

The reason for this limitation is because polymer interfacial diffusion and filament bonding only occur if the polymer is heated above its critical sintering temperature [66, 67, 68]. Because of the limited time at these high temperatures, conventional ME yields incomplete filament bonding and creation of mechanical failure points. Previous efforts to increase this heating time using heated air nozzles have resulted in morphology disruption, particularly in small samples [21]. This creates a critical processing trade-off, where uniform heating warps the structure, but a lack of heating results in poor welds. This processing difficulty prompts a more fundamental scientific question of how the filaments can be thermally bonded without bulk heating and deformation of the structure.

A solution to this problem is to apply heat directly at the polymer interface at a length scale much smaller than the filament trace dimensions, analogous to traditional macroscale metal welding. We posit that the use of nanoscale radio frequency (RF) susceptors, localized at the interface, may provide vigorous, targeted heating. In particular, carbon nanotubes (CNTs) are known to rapidly evolve heat upon exposure to microwave radiation [69, 70, 71, 72, 73, 74, 75]. This effect occurs for both single and multi-walled CNTs (SWCNTs and MWCNTs, respectively); other nanomaterials such as graphene nanoribbons have demonstrated similar heating, albeit at far slower heating rates [76, 77]. The first report of using CNTs to bond polymer substrates using microwave heating was by Zhang and co-workers [78]. Other groups have demonstrated that strong welds may be achieved between thermoplastic interfaces using microwave heating of CNTs [79, 80, 81].

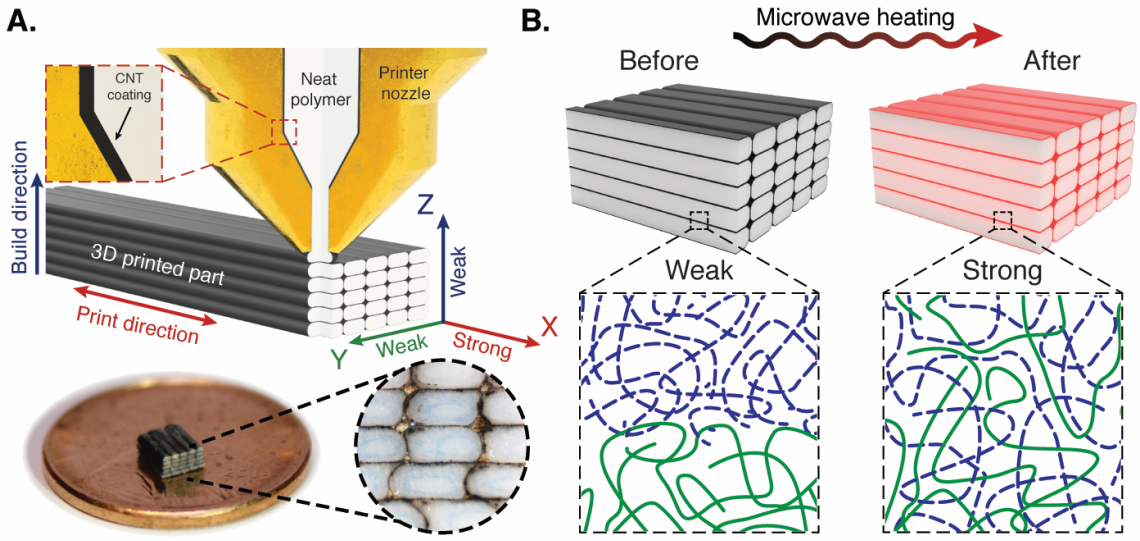

Figure 2.1: (A) 3D-printed parts tend to display weak tensile properties in the y and z directions due to poor interlayer welding. To address this, we coated thermoplastic filament with a CNT-rich layer; the resulting 3D-printed part contains RF-sensitive nanofillers localized at the interface. (B) When a microwave field is applied, the interface is locally heated to allow for polymer diffusion and increased fracture strength.

We now introduce a new technology called locally induced RF (LIRF) welding that uses MWCNTs local heating properties to enable additive manufacturing of high-strength materials (patent pending). After thermoplastic filaments are coated with an MWCNT-rich polymer film Figure 2.1A, 3D printing of these filaments results in a macroscopic structure, with MWCNTs localized only at the interfaces between each trace. Upon exposure to microwave irradiation Figure 2.1B, these MWCNT loaded interfaces selectively heat, which promotes increased local polymer mobility and entanglement across the interface. LIRF technology solves the problem described above by creating interfaces loaded with nanoscale, microwave-responsive heating elements.

2.3 Results

2.3.1 Coated filament

To deploy LIRF technology in a 3D-printed part, a material embodiment new to additive manufacturing is necessary. Our new coaxial filament structure is fabricated by way of a bath coating process Figure 2.2A, wherein a thin coaxial MWCNT ink is applied to the exterior of a feedstock polylactide (PLA) 3D printer filament Figure 2.2B.

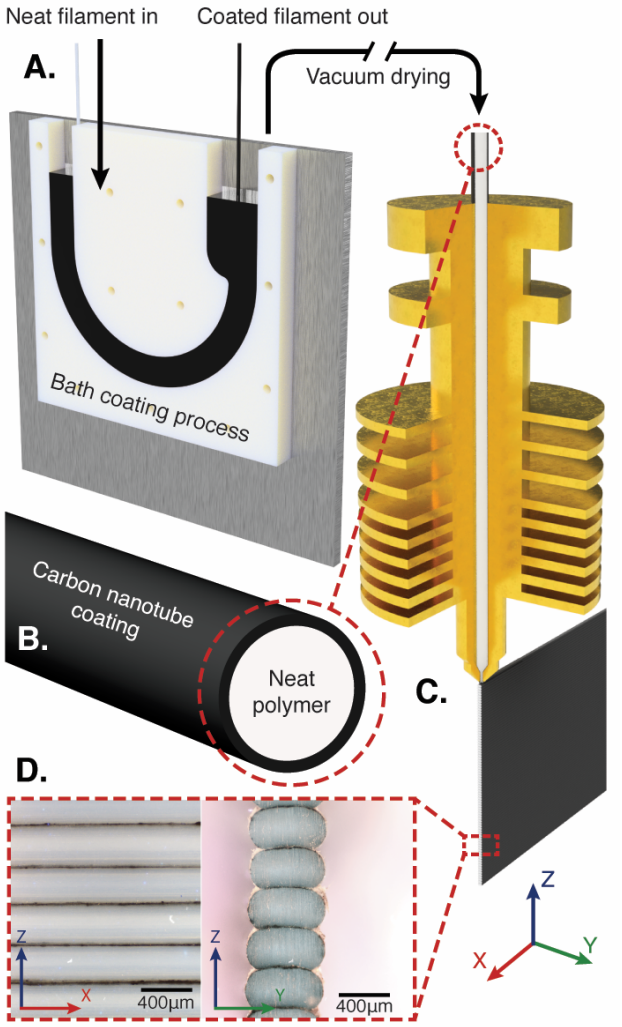

Figure 2.2: (A) Thermoplastic filaments are coated with a CNT/polymer ink and dried to create (B) coaxial filaments, where only the exterior is RF-sensitive. (C) These filaments may be 3D-printed to form structures with CNTs localized at each interface. (D) Optical micrographs of sanded cross sections show that CNTs do not migrate into the filament interior during printing.

In addition, we have demonstrated that a similar coated filament structure may be accomplished with a melt extrusion process by co-extruding a CNT masterbatch over a neat polymer core, proving that this technology is industrially scalable. We selected an engineering grade of PLA as a model 3D printing polymer, given its balance of strength

and stiffness relative to conventional engineering-grade plastics. The low melt temperature allows for processing on standard open-air desktop 3D printers. The ink is made by sonicating MWCNTs in chloroform and shear-mixing with a PLA/chloroform solution. When melt extruded through a standard 3D printer nozzle, the coating remains intact and thins because of extensional flow of the polymer Figure 2.1A and Figure 2.2C. Optical microscopy shows that the as-printed structure has the desired MWCNT-loaded interfaces Figure 2.2D.

This technology relies on the precise composition and microwave responsiveness of the coating. The specific MWCNT content in the coating and the relative thickness of the coating must be chosen to allow for microwave heating even after the printing process, which thins the coating considerably. Hence, we examined the properties of homogeneous MWCNT/PLA coatings by hot pressing solution-cast MWCNT/PLA films with MWCNT mass loadings from 0 to 20 weight % (wt %).

CNTs were first sonicated in 50ml of chloroform for 30min, whereas the PLA was dissolved in 50 ml of chloroform. The solid content of each solution was held constant at 4 mg/ml, whereas the CNT wt % was varied. Solutions were produced in a 0.5, 1.0, 2.5, 5.0, 7.5, 10, and 20 wt % CNTs. After sonication, CNTs were mixed with the dissolved PLA and placed in a glass petri dish. The petri dish was left in a fume hood overnight to let most of the chloroform evaporate off. The next day, the CNT/PLA film was placed in the vacuum oven for 24 hours to remove the remaining chloroform. After vacuum drying, the films were then removed from the petri dish.

The vacuum-dried cast films were then compacted and pressed with a parallel plate hot press (Carver 3856) at 150°C and 27.6 MPa. Two machined steel shims 0.5 mm in thickness were placed on either side of the films to maintain a constant thickness between all samples.

2.3.2 Hot pressed film characterization

The prepared hot pressed films were electrically characterized using four-point-probe (Signatone HR4-620850FN) resistivity measurements to determine the DC conductivity. Samples approximately 3.4 cm by 7.2 cm were centered on a four-point-probe stand (Lucas Labs) and measured using a differential voltage system (two Keithley 6514 electrometers, Keithley 2000 digital multimeter) with current sourced by a Keithley 6221. Starting at the lowest possible current for each sample, voltage drops were measured at three increasing decades to ensure the linear Ohmic behavior of the samples. Three measurements were taken inside the linear region for each sample and the voltage drop was taken from the average of these measurements. Volume resistivity (inversely conductivity) was calculated according to the following formula:

$$\rho = \frac{\pi}{ln2} * \frac{V}{I} * t * k$$

where ρ is the resistivity in Ohm-m, V is the voltage drop in Volts, I is the current in Amps, t is the thickness in meters, and k is a correction factor for geometry based on the probe spacing to sample diameter. For the sample geometry tested, k is taken to be 0.983 (short sample dimension 3.4 cm divided by probe spacing 0.15875 cm and correction applied from lookup table). The DC conductivity results are shown in Table 2.1 and plotted in Figure 2.3A.

Table 2.1: DC conductivity measurement details.

wt%	thickness (m)	Current (mA)	Voltage 1 (mV)	Voltage 2 (mV)	Voltage 3 (mV)	Mean Voltage Drop (mV)	StdDev Population	Resistivity (Ohm*m)
0.1	0.00048	–	–	–	–	–	–	–
0.5	0.00048	–	–	–	–	–	–	–
1.0	0.00048	–	–	–	–	–	–	–
2.5	0.00048	1.00	1.75E+02	2.21E+02	2.03E+02	2.00E+02	1.89E+01	4.27E-01
5	0.00048	1.00	1.68E+01	1.81E+01	2.23E+01	1.91E+01	2.35E+00	4.08E-02
7.5	0.00048	1.00	1.02E+01	8.05E+00	8.41E+00	8.89E+00	9.40E-01	1.90E-02
10	0.00048	1.00	5.55E+00	4.34E+00	6.05E+00	5.31E+00	7.18E-01	1.14E-02
20	0.00048	1.00	9.84E-01	1.32E+00	1.14E+00	1.15E+00	1.37E-01	2.46E-03

We then performed AC dielectric measurements to characterize the percolation behavior of the MWCNT network at microwave frequencies Figure 2.3A. In addition, we measured the transmitted, reflected, and dissipated power of the films using a two-port coaxial line technique [82].

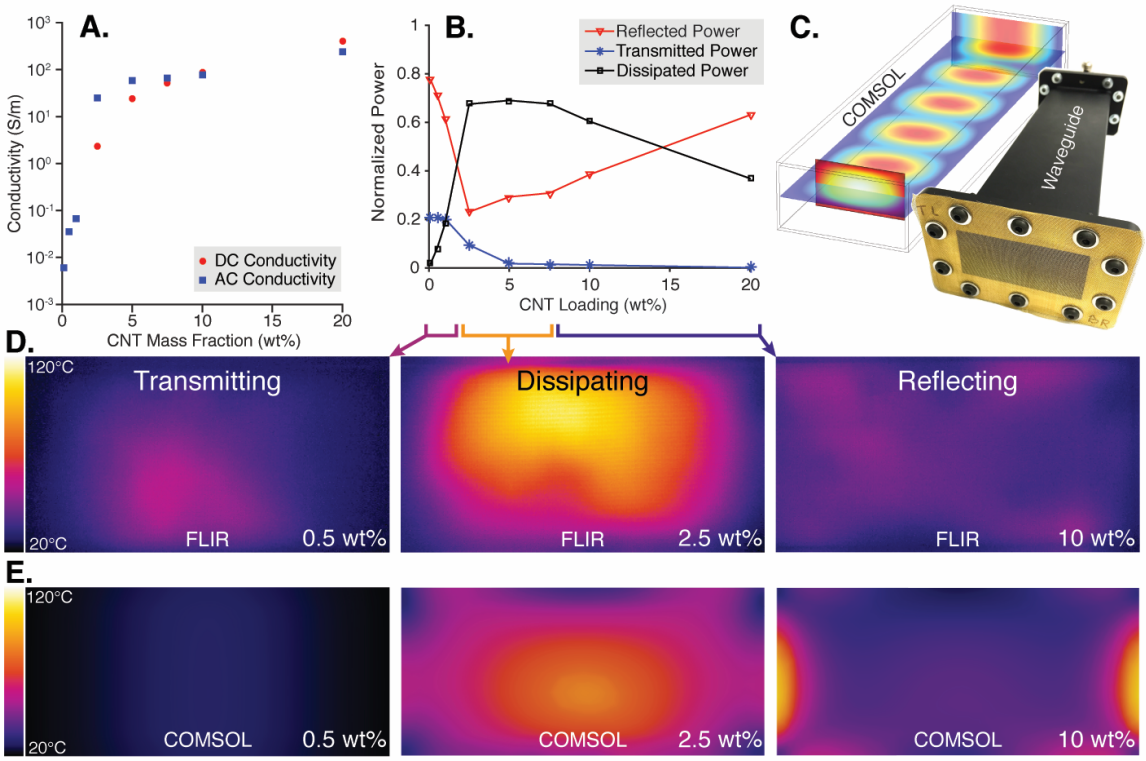

Figure 2.3: (A) Classic percolation behavior is observed for these nanotube networks. (B) Percolation is associated with a marked increase in the dissipated power, but at high loadings, the conductive network becomes reflective. (C) *In-situ* infrared imaging is used to capture the (D) heating response of the nano-filled films, and the same two transitions are observed. This trend is corroborated by (E) COMSOL finite-element simulations of RF heating and heat transfer.

Microwave AC dielectric properties of the films were measured using a coaxial measurement technique using a microwave network analyzer (Agilent E5071C) that measures the scattering (S) parameters of two-port networks. The measurement technique uses a disk shaped sample sandwiched between two transmission lines, as shown in Figure 2.4.

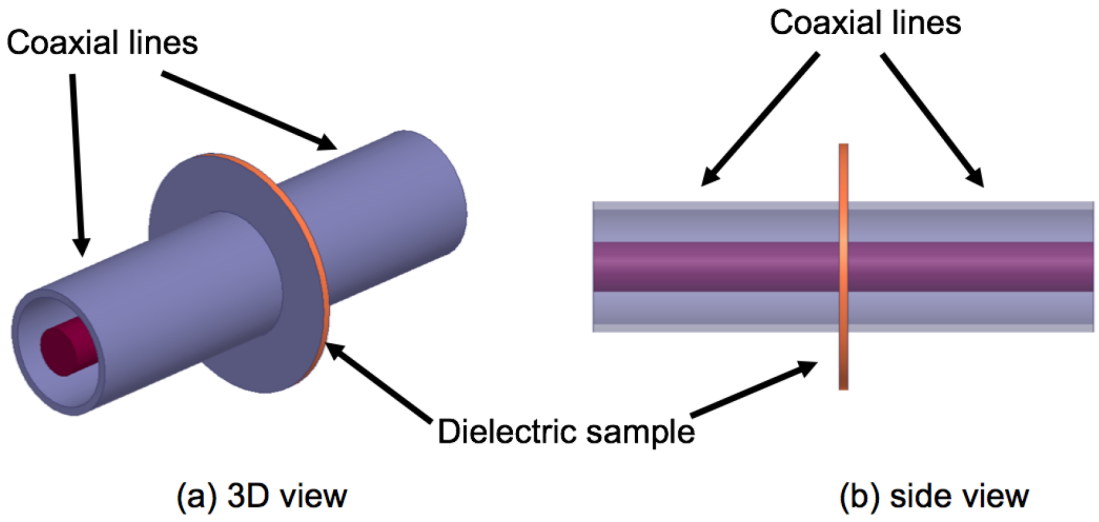

Figure 2.4: Dielectric measurements using a sample holder placed between two coaxial transmission lines.

The parts of the dielectric disk that are outside the coaxial lines are completely enclosed with a conductor. For convenience, two 7 mm Amphenol Precision Connectors (APC-7) where used to act as the sample holder. A disc punch was used to punch out samples 14.8 mm in diameter ensuring the films would fit precisely in the sample holder with minimal air gaps at the edges. The sample thickness was 0.5 mm. The method for extracting the complex permittivity (or the dielectric constant and conductivity) is based on full wave electromagnetic analysis of the structure. Two completely different methods were used, one is based on the method of moments and the other uses a commercial software based on the finite element method (ANSYS HFSS). Determining the complex permittivity from measurements is an inverse problem. Therefore, in both methods optimization techniques are necessary where an objective function describing the error between computed and measured quantities is minimized. We used the S21 parameter (the transmission coefficient), which is a complex quantity, in the optimization objective function to retrieve

the complex permittivity, and ensured that the iterative optimization procedure had proper convergence for all the measured samples.

To better understand the mechanism for the rapid heating response, we measured the microwave absorbing properties of the hot pressed PLA films using a microwave network analyzer (Agilent E5071C) and a two port coaxial transmission line technique. Round discs of each film thickness were fitted into a coaxial adapter while ensuring that air gaps were eliminated. The network analyzer measures the scattering parameters (S11 and S21) by detecting the incident, reflected, and transmitted microwave signals. The ratios of the reflected and transmitted powers to the incident power are equal to |S11|2 and |S21|2, respectively. The power absorbed by the sample and dissipated as heat, normalized to the incident power, is calculated using the following formula:

$$\frac{P_{diss}}{P_{inc}} = 1 - |S_{11}|^2 - |S_{21}|^2$$

The measured AC dielectric properties including the real part of the relative permittivity, the loss tangent, and the AC conductivity are plotted in Figure 2.5.

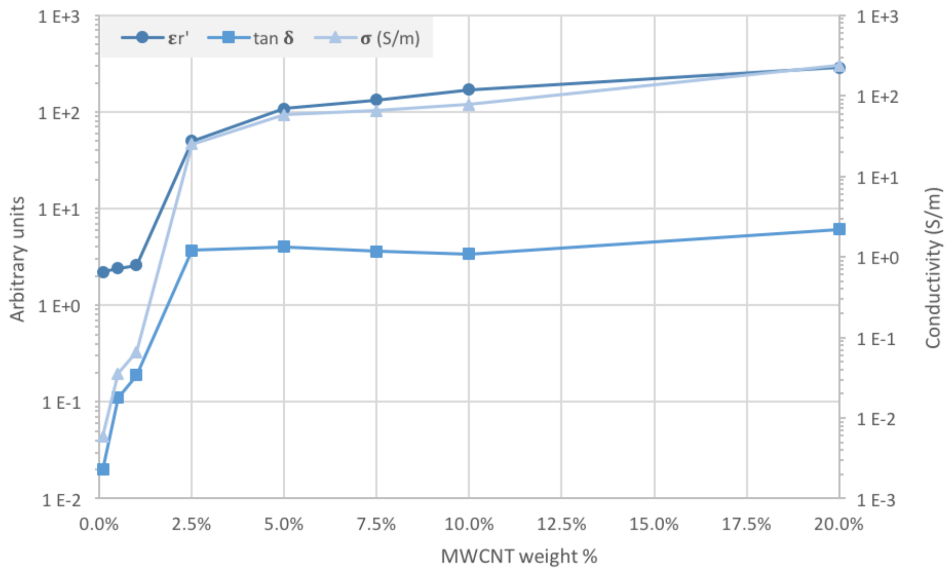

Figure 2.5: AC dielectric properties including the real part of the relative permittivity, the loss tangent, and AC conductivity.

2.3.3 Waveguide heating of hot pressed films

These dielectric measurements are then correlated with thermal imaging during microwave exposure. The hot pressed films were heated in a rectangular waveguide (AMCSS-284-F/F-12-B, AMC LLC.) powered by a solid state microwave source (GMP 150, Opthos Instruments Inc.) operated at 2.45 GHz at various power levels for 30 seconds. Spatial temperature measurements were carried out using an infrared camera system (A655sc, FLIR Systems Inc.) calibrated to measure temperatures of a sample located behind a brass mesh covering the open end of the waveguide (Figure 2.3C and Figure 2.3D) [83]. The samples were inserted into the waveguide at the location of the first maximum of the electric field standing wave, approximately 57.9mm from the brass mesh. This ensures the samples were exposed to the strongest and most uniform electric field in the closed waveguide. Various power levels were used to heat the samples and their temperature response

was recorded using the FLIR supplied software (ResearchIR MAX).

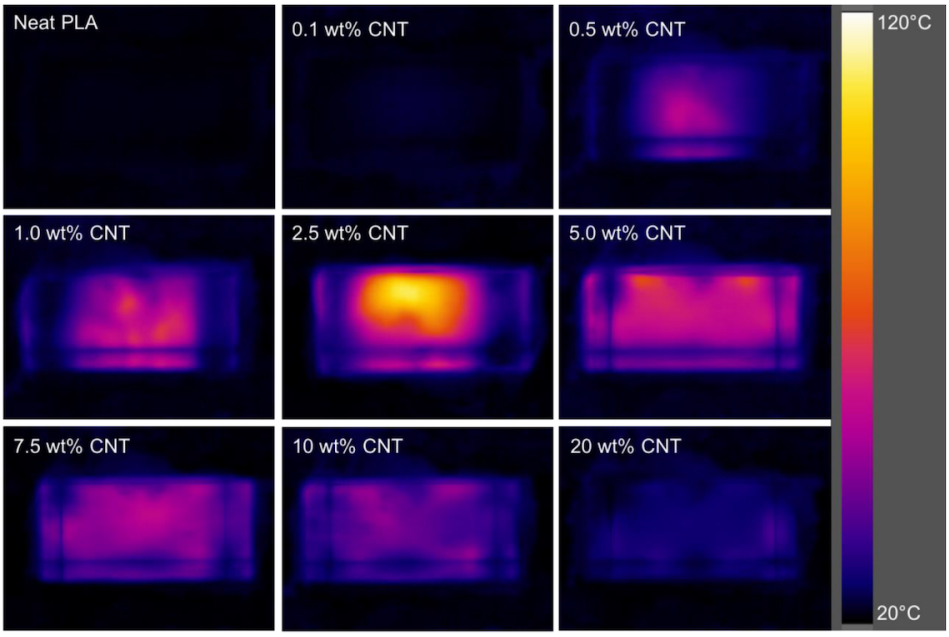

Figure 2.6: FLIR thermal image screenshots of hot-pressed PLA films after 30 s of heating at 15 W.

We observed a strong correlation between electrical percolation and the heating response of the films, with a major increase in the heating rate above the percolation threshold [75]. This implies that there is a minimum MWCNT loading in the film to achieve a rapid heating response. Counterintuitively, the heating response then decreases Figure 2.6 and becomes less uniform at higher MWCNT loadings.

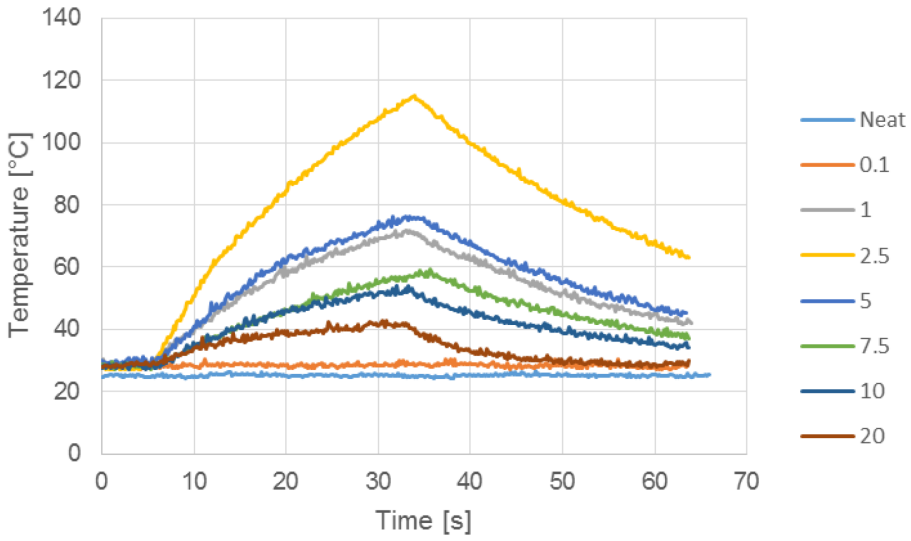

Figure 2.7: Max temperature versus time for various wt % of CNTs in waveguide, 15-W microwave power.

As shown in Figure 2.7, the 2.5wt% CNT film achieved the highest maximum recorded temperature when heated in the waveguide at 15 Watts of incident power. This surprising result occurs because, at higher loadings, the films become more reflective and thus less absorptive to incident microwaves Figure 2.3B. This finite range of loading, where there is strong coupling between the electromagnetic field and composite, is necessary for maximizing both heating rate and uniformity. This phenomenon has not been applied to composite processing in previous literature. We also conducted finite-element simulations of microwave adsorption and heat transfer using COMSOL Multiphysics Figure 2.3E; similar trends appear (Figure 2.8), showing that these concepts can be accurately simulated from first principles.

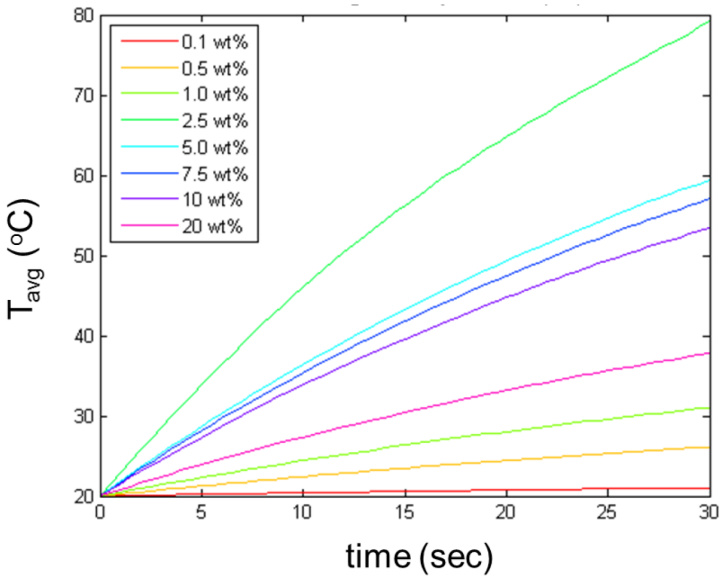

Figure 2.8: COMSOL simulation predictions for temperature (average) versus time for all samples.

2.3.4 Coating composition and heating

2.3.4.1 Heating response as a function of thickness

We also investigated how thin MWCNT/PLA films respond to the microwave as a function of film thickness. These films were created by spray-coating composite films onto glass slides. To do so, 9 g of PLA pellets were dissolved in 100 ml chloroform. Separately, 1 g of MWCNTs were added to 150 mL of chloroform and sonicated for 30 minutes. The two solutions were mixed to give a 10 wt% solids in solution at a concentration of 40 mg/ml MWCNT. This ink was then diluted in 1:4 and 1:16 ratios to give inks suitable for spray coating. These diluted inks were then sprayed onto PLA films and glass slides using the apparatus pictured Figure 2.9.

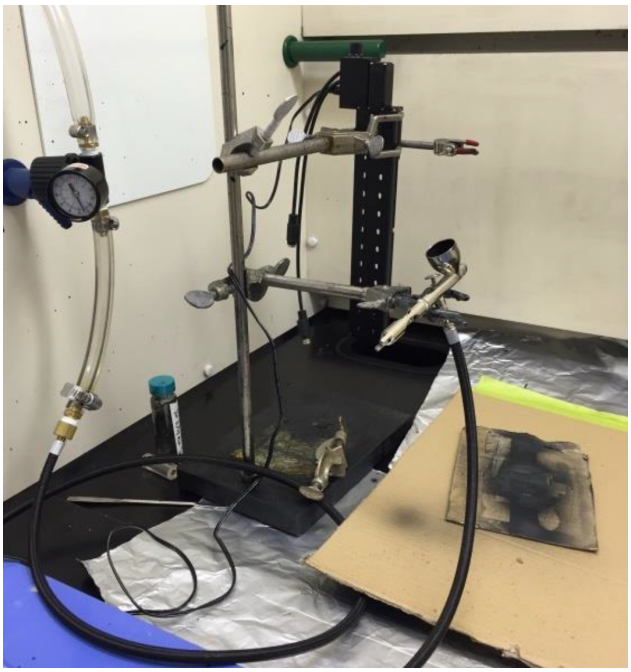

Figure 2.9: Setup for spray coating PLA films of varying thickness. The linear actuator held by the far lab stand arm moves a piece of cardboard in front of the hobby sprayer as it sprays a constant stream of 10wt% solids MWCNT / PLA / chloroform ink.

This apparatus consisted of a lab stand with an arm that held a motorized track and an arm that held a hobby airbrush. The track arm and the airbrush arm were perpendicular. On the end of the track arm was a motorized track that moved vertically, with an arm taped perpendicularly to the direction of movement of the track. A hobby airbrush was placed in the airbrush arm and directed at a piece of cardboard that was held in the arm on the motorized track. This piece of cardboard held a glass slide and a piece of PLA film to which the coatings were applied. The track moves up and down at a constant speed of 0.554 cm/s, with the films applied by allowing the airbrush to spray at a constant rate while the track moved the slide and PLA through MWCNT ink stream. Pressure, spray rate, and dilution were varied per sample to achieve smooth, even films of varying thickness. Because the glass and PLA are coated under the same conditions, the same

thickness of film is applied. Remaining solvent was driven off under vacuum.

The PLA films heating response due to microwaves was characterized, and the thickness of the glass slide was measured by profilometry (KLA Tencor P-6). These data were matched up and used to plot heating of films against thickness in Figure 2.10. A positive, exponential relationship between heating response to microwaves and thickness is visible in the graph.

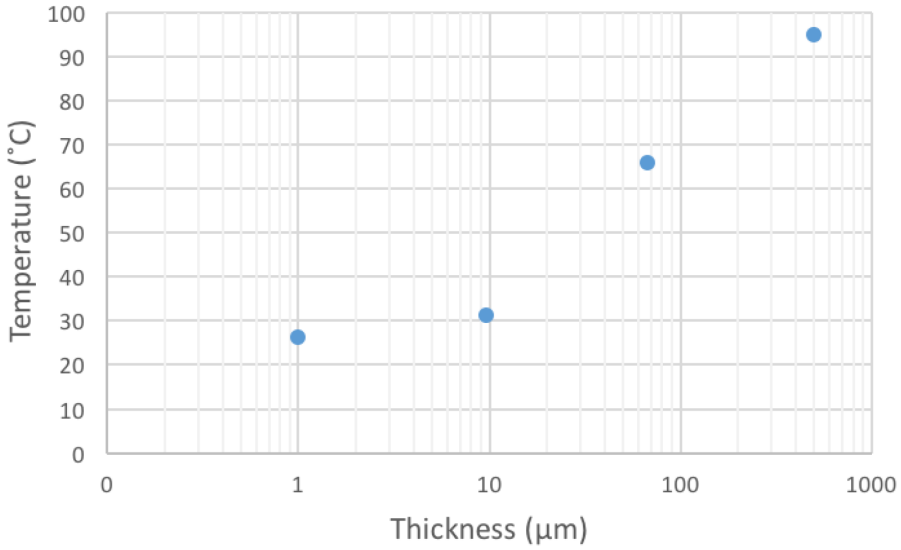

Figure 2.10: The microwave response of 10 wt % MWCNT spray-coated PLA films (as quantified by the mean temperature of the film at 30 s) versus film thickness.

2.3.4.2 Microwave bonding of thermoplastic interfaces

To create the ink used in coating the films, 3.6 g of PLA pellets were dissolved in 50 mL of chloroform. Separately, 0.4 g of MWCNTs were added to 50 mL of chloroform and then sonicated for 30 minutes. The two solutions were mixed to give a 10 wt% solids in solution at a concentration of 40 mg MWCNT/mL. The ink was then sprayed onto the

PLA films using a hobby airbrush. The area of the sprayed region was about 6.45 cm^2.

The prepared samples were layered end over end like a typical lap joint. The samples were placed between two glass slides then two rubber bands were wrapped around the slides to keep tension on the films. The samples were then placed in a faraday cage and irradiated at different times and powers using a 1250 W Panasonic microwave oven with Inverter technology.

Lap shear and tensile strength measurements of the welded PLA films were conducted using an Instron with a 500 N load cell. BlueHill software was used for data acquisition and analysis. The area of the weld was entered into the software before each run. The sample was then placed vertically into the clamps and secured. The clamps started extending the samples at a constant crosshead speed of 1.25 mm/min until the sample failed. Once the sample failed, the clamps automatically returned to their starting positions, and the sample was removed and a new one was placed in the clamps.

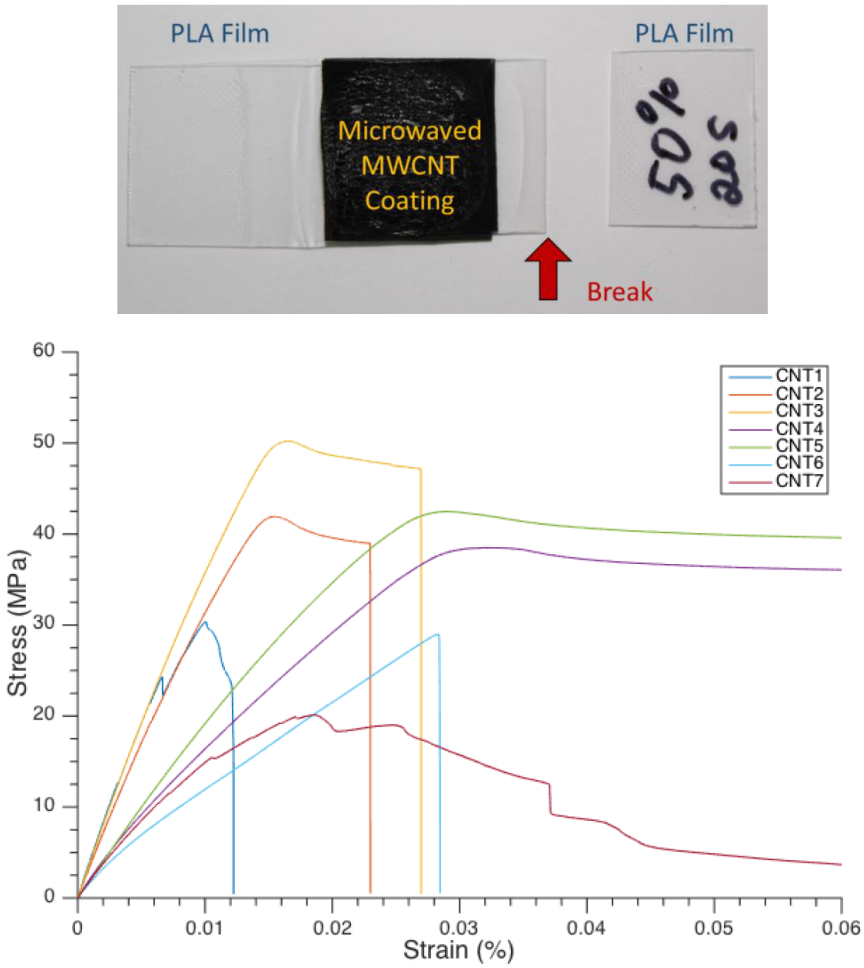

Figure 2.11: Stress versus strain for lap-shear samples. For all samples, the break occurred outside the weld (inset above).

Our data (Figure 2.11, 10wt% MWCNT/PLA ink spray coated onto PLA film, bond area 2.5cm x 2.5 cm, microwaved in 1250W chamber at 50% duty for 15 s) show that microwave radiation of thin MWCNT coatings can induce sufficient polymer diffusion to cause tensile failure to occur outside the weld. For some samples (see sample CNT7 in the figure), over-heating in the microwave can cause the surrounding polymer to fail.

2.3.4.3 Filament coating method

A bath coating process was employed to achieve a thin conformal coating of CNTs + polymer on the exterior of the feedstock PLA filament (Zen Toolworks, ZTW 3D Filament PLA 1.75mm Natural, Polylactide supplied by NatureWorks). The filament diameter as measured by calipers was found to be 1.70 mm $\pm$ 0.4 mm. Material properties for the PLA supplied from the manufacturer are listed in table 2.2.

Table 2.2: Material properties of PLA filament.

Properties	**Test Method**	**Test Condition**	**Unit**	**Value**
Specific Gravity	ASTM D792	-	-	1.25 - 1.28
Melt Flow Index	ASTM D1238	230°C	-	1.08 - 1.12
Glass Transition Temperature	ASTM D3417	-	°C	55 - 60
Melting Temperature	ASTM D3418	-	°C	145 -155
Melt Flow Rate	ASTM D1238 A&B	210°C	g/10min	5 - 15
Tensile Strength	ASTM D638	-	MPa	48
Impact Strength	ASTM D256	-	J/m	0.16
Flexural Strength	ASTM D790	-	MPa	83

CNT composite ink was prepared in a similar manner to the solution-cast hot press films and ink used for spray coating. Specifically, 3.6 g of PLA pellets were dissolved in 50 mL of chloroform. Separately, 0.4 g of MWCNTs were added to 50 mL of chloroform and then sonicated for 30 minutes. The two solutions were mixed to give a 10 wt% solids in solution at a concentration of 40 mg MWCNT/mL. This ink was then shear mixed in an ultra-high shear mixer (Silverson L5MA with 5/8 Micro SL mixing head) at 5,000 RPM

for 1 hour. To coat the neat PLA filament, first the dip coater was loaded with 10 wt% CNT ink. The neat PLA was drawn through the dip coater (Figure 2.12) and kept vertical during the drawing and drying process to ensure an even radial coating was deposited. The excess chloroform was allowed to evaporate off in the fume hood. Next the coated filament was placed in the vacuum oven at 100°C and left for 24 hours to drive off any remaining solvent.

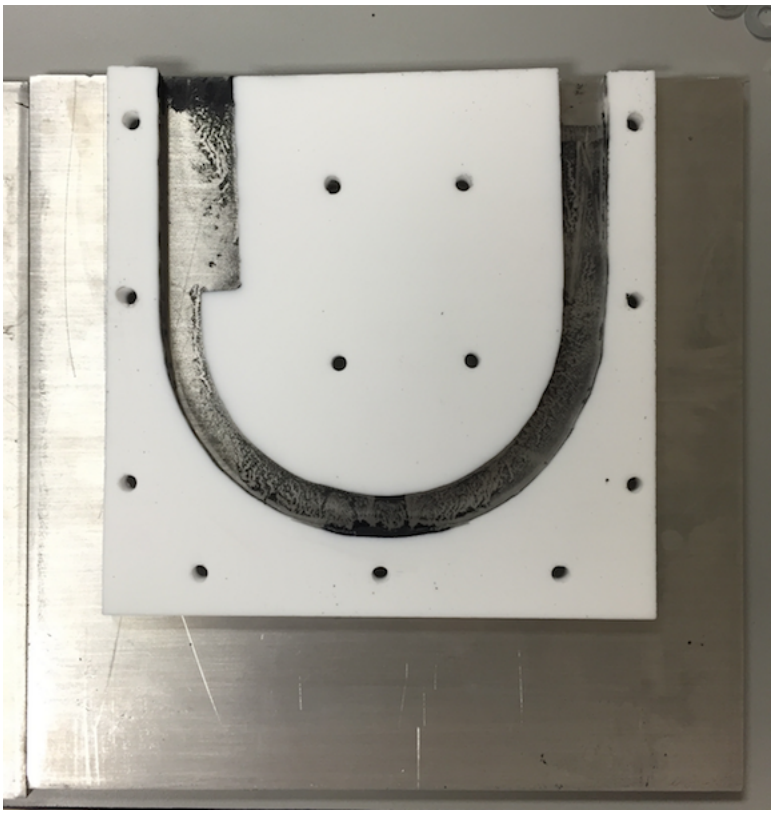

Figure 2.12: Coating bath internal view. The structure is comprised of Teflon guide sandwiched between two aluminum plates.

The coated filament was characterized by SEM and optical microscopy and correlated with linear mass density measurements to determine the areal coverage (Figure 2.13).

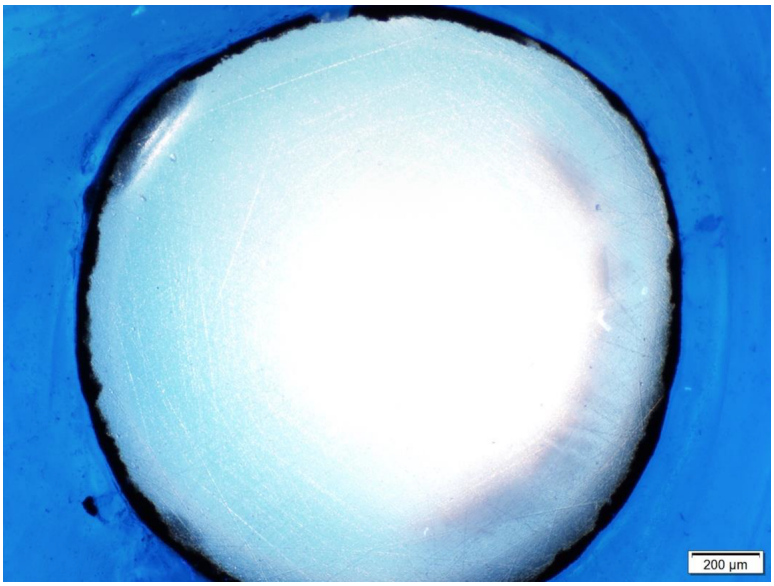

Figure 2.13: Microscope image of the 1.75 mm printer filament with CNT coating.

By weighing a section of filament before and after the coating process and dividing the differential weight by the length of filament, an average linear mass loading of approximately 1 mg/cm of filament was achieved with the coating process. Assuming the CNT composite has a density of 1.34 g/cm^3 (0.9*1.25 g/cm^3 + 0.1*2.1 g/cm^3 weight average of PLA and MWCNTs) and the neat filament has a diameter of 1.7mm, the thickness of the coating would be approximately 14.0 μm. This value agrees well with optical micrographs of filament cross-sections. As coated filament is fed through the 3D printer extruder nozzle, it is thinned out due to extensional flow. From optical micrographs of printed unit cells (Figure 2.14), we conclude that with careful selection of printer parameters, very little mixing between the CNT composite sheathing and inner polymer core occurs.

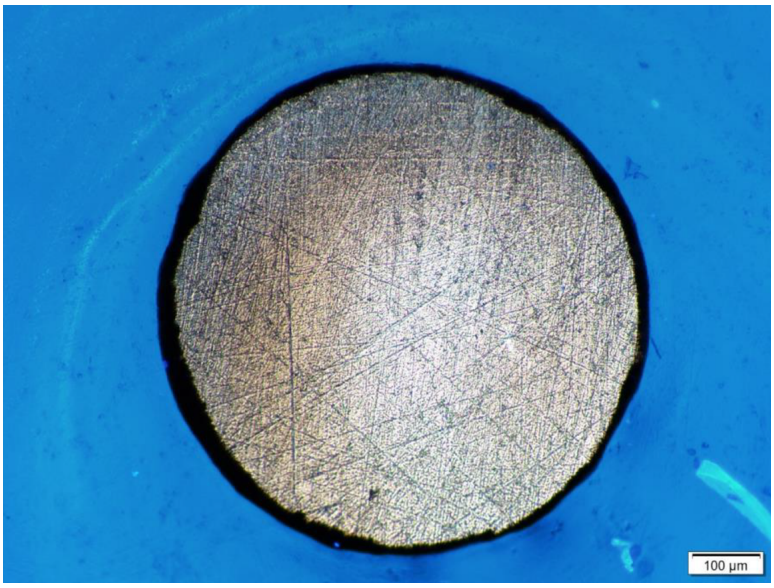

Figure 2.14: Microscope image of the coated filament after being extruded from a 0.5 mm nozzle.

Therefore, using volumetric consistency between the coated filament feedstock and the extruded filament, the thickness of the coating after extrusion may be calculated as follows:

$$coating\ thickness = R_0 - R_I$$

$$area\ coat = \pi(R_0^2 - R_I^2)$$

$$E_{coat} = R_{EO} - \frac{R_I R_{EO}}{R_O}$$

where E_{coat} is extruded coating thickness, R_{EO} is extruded outer radius, R_I is filament inner radius, and R_O is filament outer radius as in Figure 2.15. We compute E_{coat} = 3.9 μm.

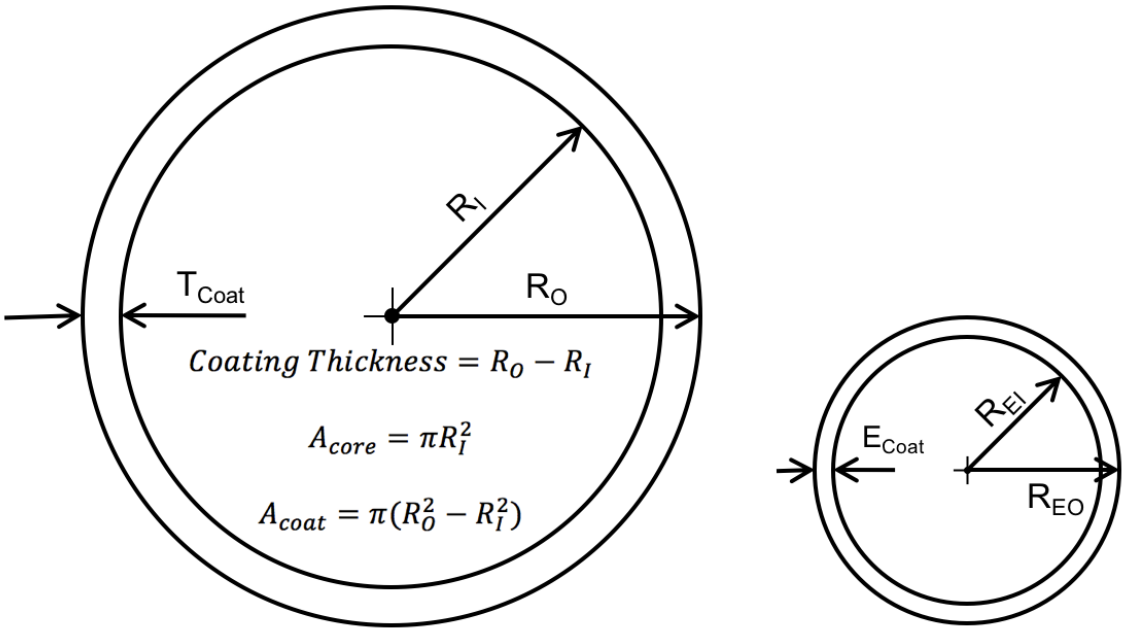

Figure 2.15: Schematic for calculation of coating thickness.

2.3.4.4 Heating response of coated filaments

These heating experiments and simulations directly inform the choice of coating composition, the coating thickness, and the microwave parameters used for the actual heating process. Of course, all this characterization is for homogeneous MWCNT-loaded polymer films; to relate this work back to our 3D-printed structures, we both measured and simulated MWCNT-coated filament bundles. Cross sections of coated filaments were super glued to a PLA film to create a bundle (Figure 2.16).

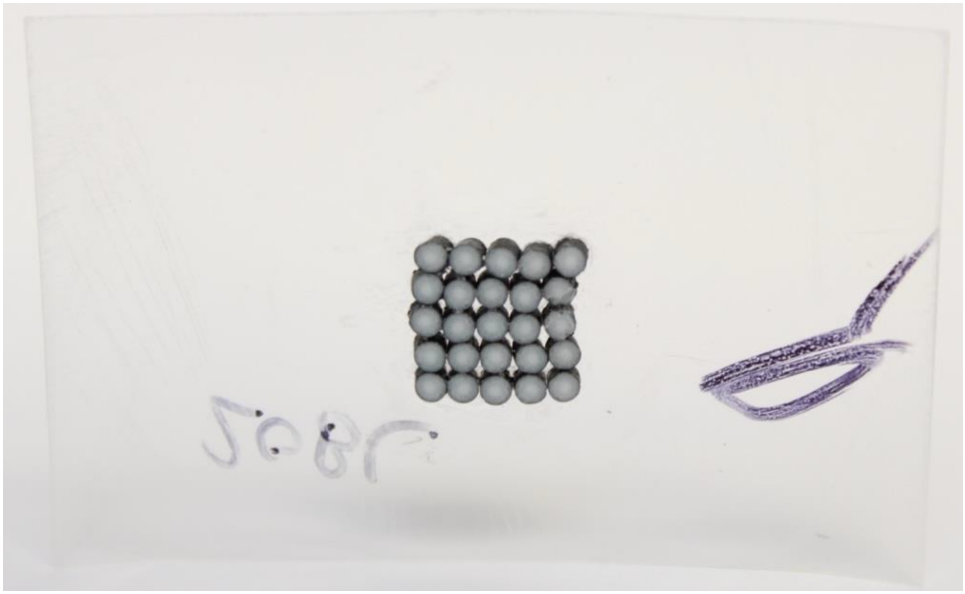

Figure 2.16: Coated PLA filament array glued to polymer film.

The bundle was then placed in a waveguide and irradiated at 150 W. The temperature was monitored using a FLIR camera equipment with a microscopic lens and FLIR software. Figure 2.17 clearly demonstrates that there is only heating at the interfaces instead of throughout the entire bundle or only at the edges of the bundle. Heat emanates from the peripheral circumference of the filaments in the bundle, which coincides directly with the nanotube coating. This site-specific heat source sets up a thermal gradient between the coating and the interior of the neat PLA filament.We simulated the same bundle geometry in COMSOL with an applied electromagnetic boundary surface heat source at the filament circumference and observed a thermal gradient consistent with the temperature profile observed in the FLIR recording.

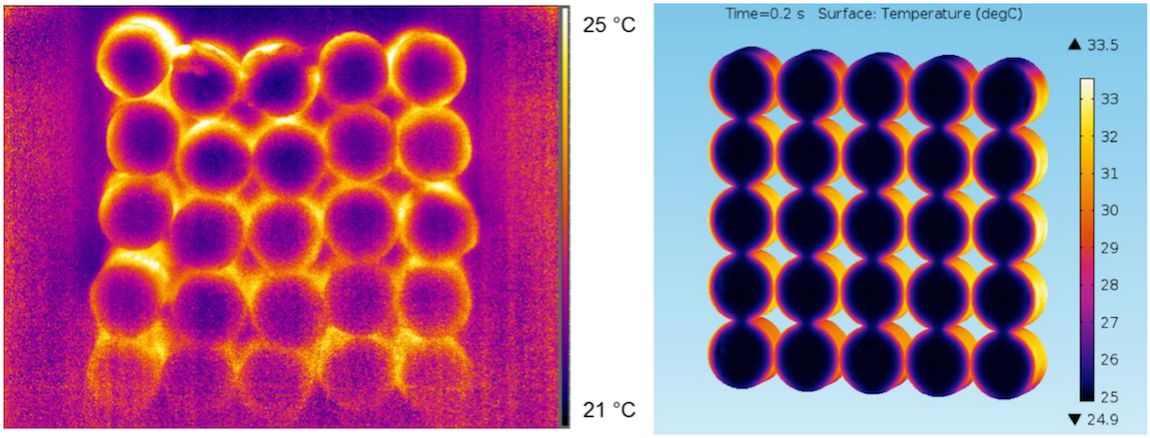

Figure 2.17: FLIR image of coated filament bundle heating in waveguide and corresponding COMSOL simulation of filament bundle heating in a waveguide. Edge heating phenomena consistent between the simulation and experiment. Right: FLIR image of coated filament bundle heating in waveguide. Left: COMSOL simulation of filament bundle heating in a waveguide. Edge heating phenomena consistent between the simulation and experiment.

Heating only at the interfaces instead throughout the entire structure improves the mechanical properties of the print. Heating in an oven would cause uneven heating. The interfaces near the edges of the part would become stronger than the interfaces in the interior of the part. Using the microwave procedure all the interfaces receive a similar amount of heating without overheating the structure which would result in dimensional changes and warping of the printed structure.

2.3.4.5 Additional coating constraints

Additional constraints on the coating composition are imposed by the extrusion process during printing. There is a maximum MWCNT loading in the coating based on the ability of the coating and filament core to co-flow during extrusion; at higher loadings, flow instabilities may result. Similarly, the coating thickness is determined by a trade-off between the need to generate heat and the need to localize that heat. For our experiments, we

selected a coating containing 10wt%MWCNTs and a coating thickness of approximately 14 μm.

2.3.5 LIRF welding of 3D printed coupons

For the microwave exposure process itself, the underlying polymer physics are an example of classic polymer welding; three critical parameters define the system: time, temperature, and pressure. In an additive manufacturing context, one cannot control pressure, and uniform heating warps the as-printed structure. Therefore, we use the embedded MWCNT coating to control the temperature at the interface for a given time. The CNT compositecoated filament was used to print the coupons used for the microwave heat treatment and mechanical testing. Samples were printed on an ME or fused filament fabrication style 3D printer (Stacker 500) shown in Figure 2.18.

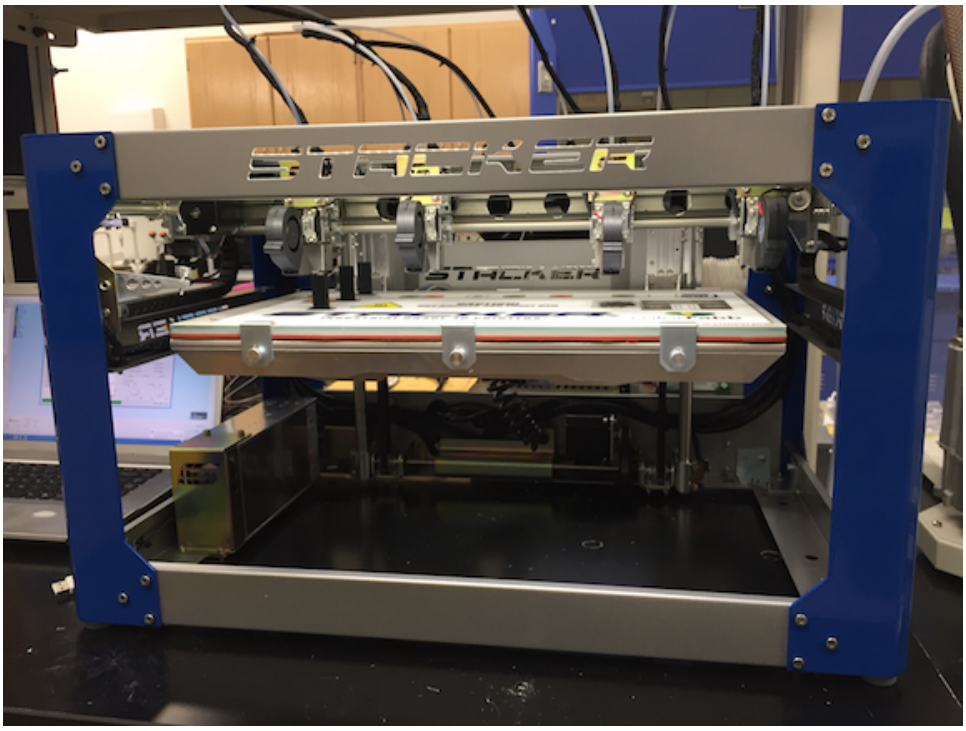

Figure 2.18: Stacker 500 desktop material extrusion 3D printer.

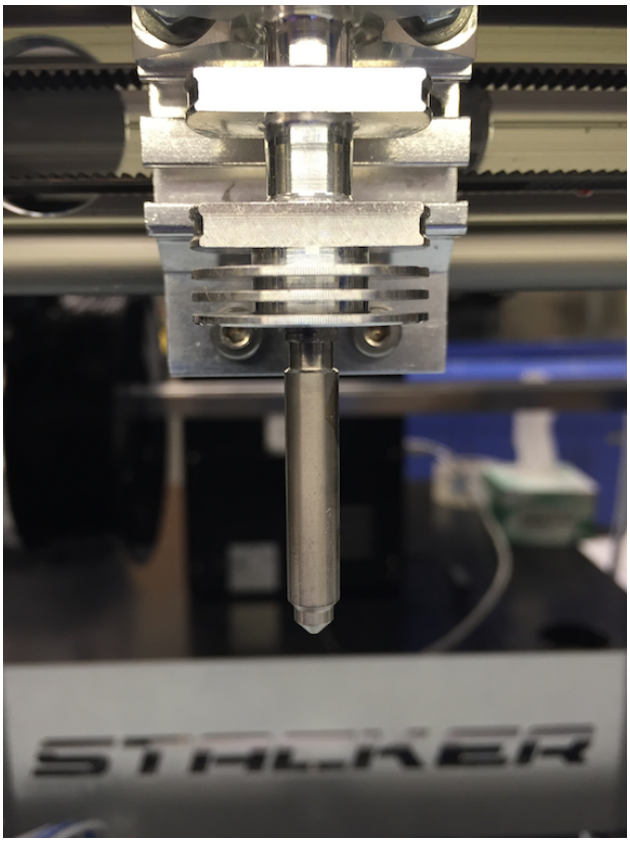

Figure 2.19: Stacker printer nozzle showing heat sink.

The nozzle bore on the Stacker 500 was fixed at 0.5 mm in diameter (Figure 2.19). Rectangular sample coupons, a single trace in width, were printed in the vertical (z) direction in a continuous spiral pattern to ensure that each layer had a spatially uniform thermal history during printing (Figure 2.20). The edges of each double-wall sample were trimmed with shears yielding a rectangular sample with dimensions in accordance with ASTM D1938. The sample is torn such that the fracture propagates along a single Z direction weld line.

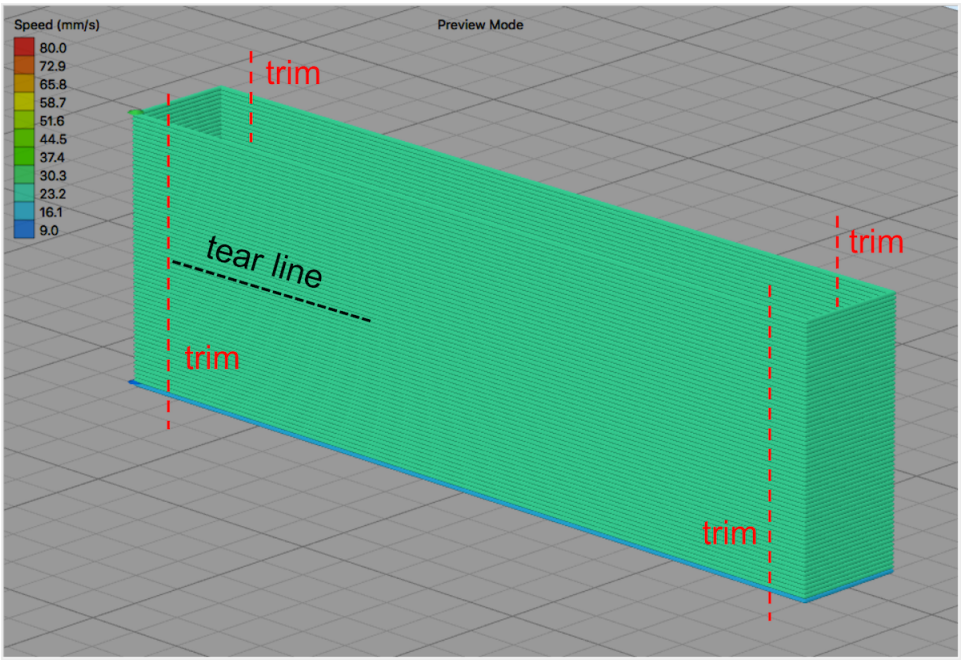

Figure 2.20: Slicing pattern and G-code preview of the rectangular tear specimens.

We then exposed the samples to microwaves in our waveguide apparatus, and the temperature was monitored using a FLIR camera as before (Figure 2.21. The waveguide was positioned vertically and a Teflon block was fixed at the maximum electric field node. The tear samples were positioned in the waveguide, resting on the Teflon block, such that the printed traces were aligned parallel to the electric field. This orientation resulted in the most uniform and repeatable heating pattern.

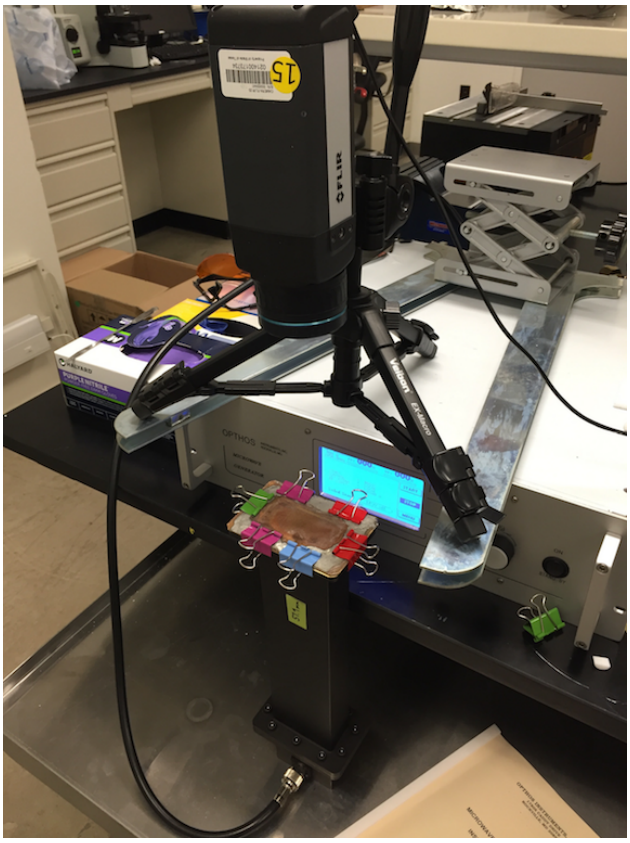

Figure 2.21: FLIR camera positioned over the waveguide to directly measure sample temperature during exposure to microwaves.

To achieve the most accurate temperature reading on the samples, a microwave choke tube was fashioned to allow direct viewing of the samples, instead of viewing through a mesh. The choke tube attenuates the microwaves down to a level that is safe for both the camera equipment and human exposure limits [32]. The choke tube dimensions were selected to have a 30dB attenuation of the microwave power, according to the following equation:

$$\alpha = 0.18\sqrt{\frac{22,500}{a^2} - f^2}$$

where α is the attenuation constant (in dB/m), a is the long dimension of the choke tube in meters, and f is the frequency in MHz. A choke tube 3cm wide results in an attenuation constant of 785 dB/m, which means a choke tube 3.8 cm or longer is appropriate. The choke tube used in our setup is shown in Figure 2.22.

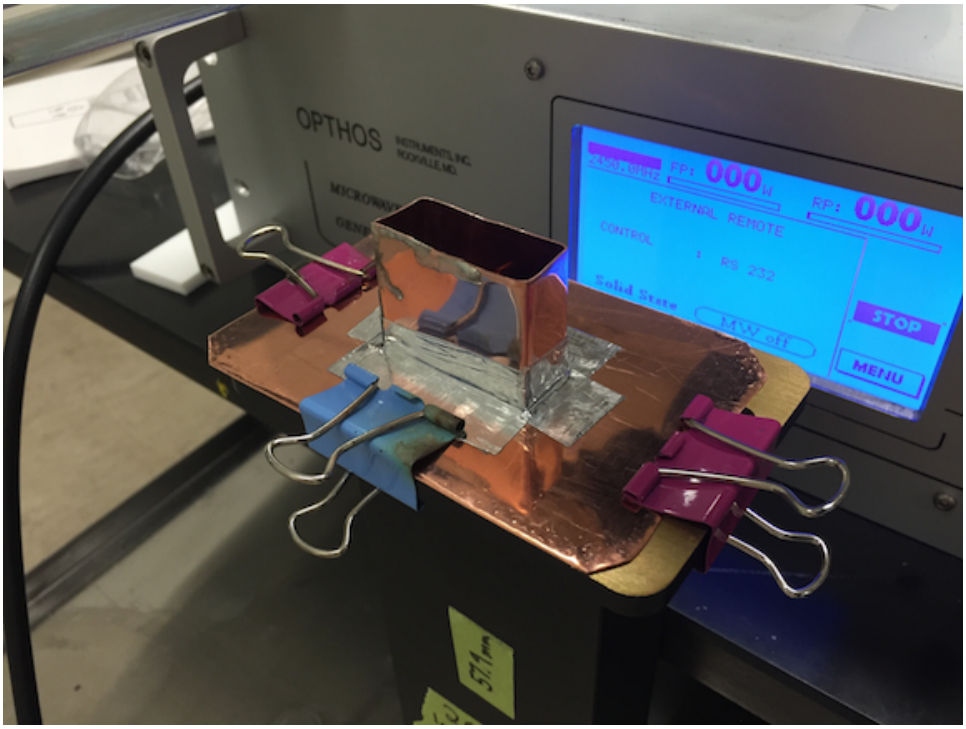

Figure 2.22: Microwave choke tube designed to attenuate and contain microwave energy yet still allow for direct viewing of sample.

From a processing standpoint, it is desirable to minimize the time required to weld the interfaces. Therefore, we controlled the microwave power to achieve high heating rates at the start of the exposure to bring the sample up to the welding temperature as quickly as possible, and manually regulate the power once the sample reached the desired temperature. Semicrystalline polymers, including PLA, benefit from having the interface above

the melting point of the polymer so that crystalline regions can melt, diffuse, and recrystallize across the weld line [84, 85, 86, 11]. For our microwave heat treatments, we used an exposure time of 60 s at 160°C as shown in Figure 2.23. Note that these temperatures are too low to induce structural changes or covalent alterations in the MWCNTs [69, 73].

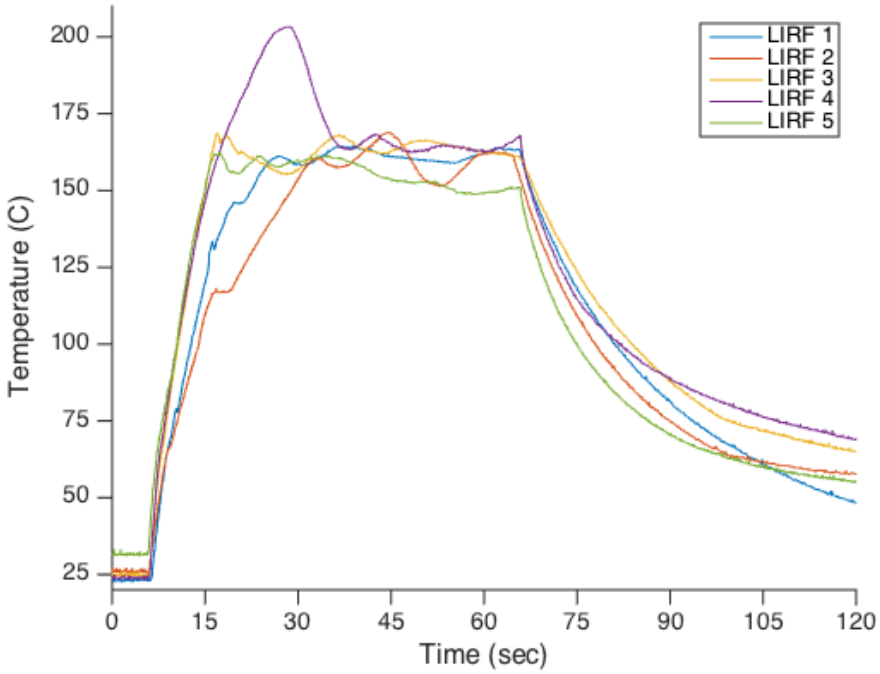

Figure 2.23: Maximum temperature versus time for all five LIRF samples.

From a process control standpoint, this type of temperature control could be computer-controlled via a closed-loop proportional-integral-derivative (PID) controller. The solid-state microwave source used in this study has the ability to be controlled via serial communication protocol. In the future, if such a closed-loop power control system could be implemented, it is likely that more consistent improvements in the mechanical properties of the samples would be observed.

2.3.6 Tear tests

To determine the strengthening effect of the LIRF welding process on 3D-printed interfaces, we selected a mode III tear propagation resistance (trouser tear) test suitable for thin plastic sheets (ASTM D1938) illustrated in Figure 2.24A.

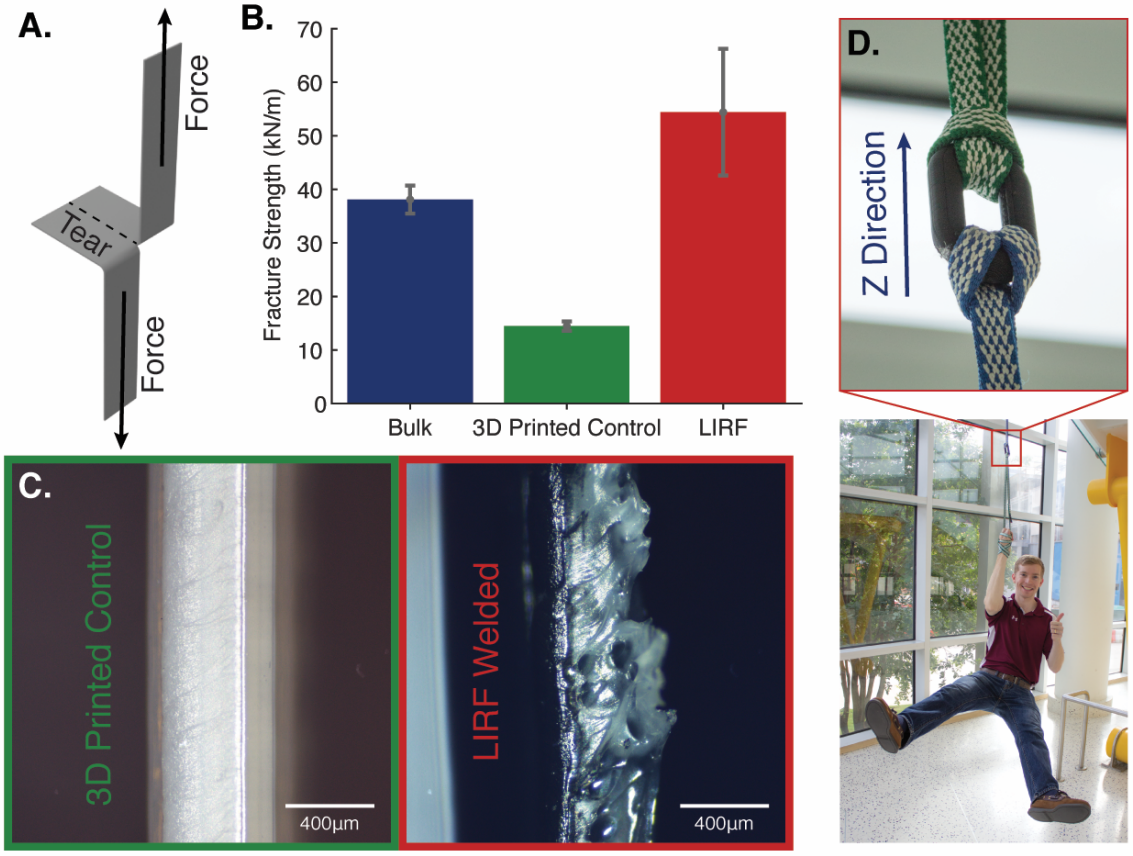

Figure 2.24: (A) Tear tests are used to determine that (B) the fracture strength of 3D-printed PLA coupons is increased by 275% when CNT coatings and LIRF welding are applied. (C) Optical micrographs of the fracture surfaces reveal significant necking and crazing in the LIRF-welded sample, whereas the smooth surface of the 3D-printed control sample indicates a brittle fracture. (D) A nanotube-coated, LIRF-welded PLA chain link printed in the z direction is able to support the weight of C.B.S. This LIRF welding enables new, high-strength applications of additive manufacturing.

This technique was identified as a standard test to gauge the fracture strength of 3D-printed interfaces [11]. The sample is torn such that the fracture propagates along a single z direction weld line. This test method accurately gauges the fracture strength of a single 3D-printed layer weld line as it fails via the slip-stick mechanism; this is a mode III analog to a double cantilever beam (mode I) test [23]. The results of the trouser tear tests are presented in Figure 2.24B for neat hot-pressed films (that is, bulk polymer with no-weld line) and 3D-printed coupons including both neat- and CNT LIRFwelded specimens. CNT-coated specimens without the LIRF treatment behave similarly to the neat specimen.

Figure 2.25: Instron 5944 load frame used for tensile and tear tests.

Trouser tear test samples were tested according to ASTM D1938 standards on an Instron 5944 mechanical tester (Figures 2.25 and 2.26) fitted with a 500-N load cell and equipped with Bluehill software.

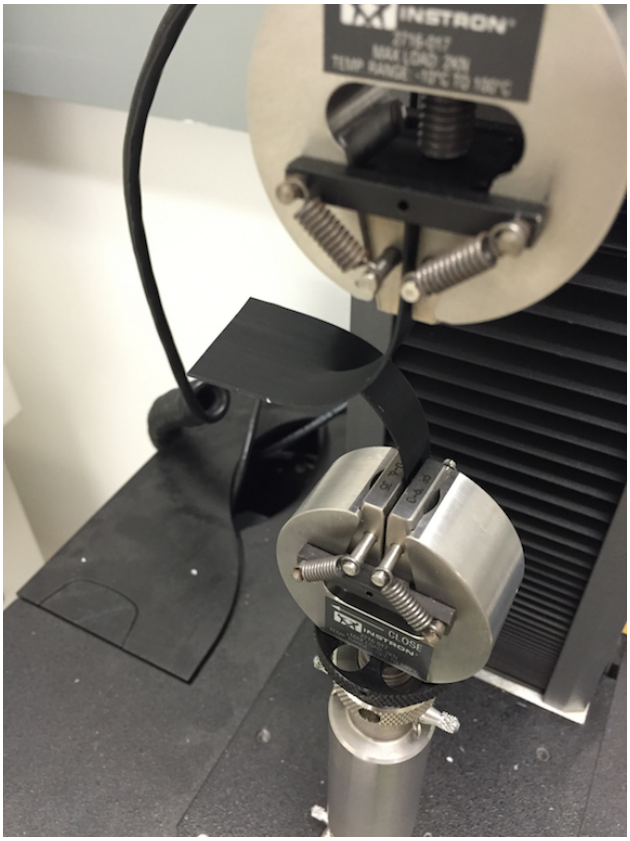

Figure 2.26: Close-up view of sample gripped in the tensile load frame.

Samples were tested at a strain rate of 100 mm/min. The thickness of the fracture surface was calculated from end-view fracture surface images as shown in Figure 2.27; the mean value for 3D-printed samples was found to be 0.419 mm. Note that it is important to use the actual thickness of the 3D printed interface, since nominal values measured from the outer edges of the sample will result in values below the actual fracture strength. For

the bulk samples, no ridges from the printing process are present, so a micrometer is an appropriate tool to measure the film thickness.

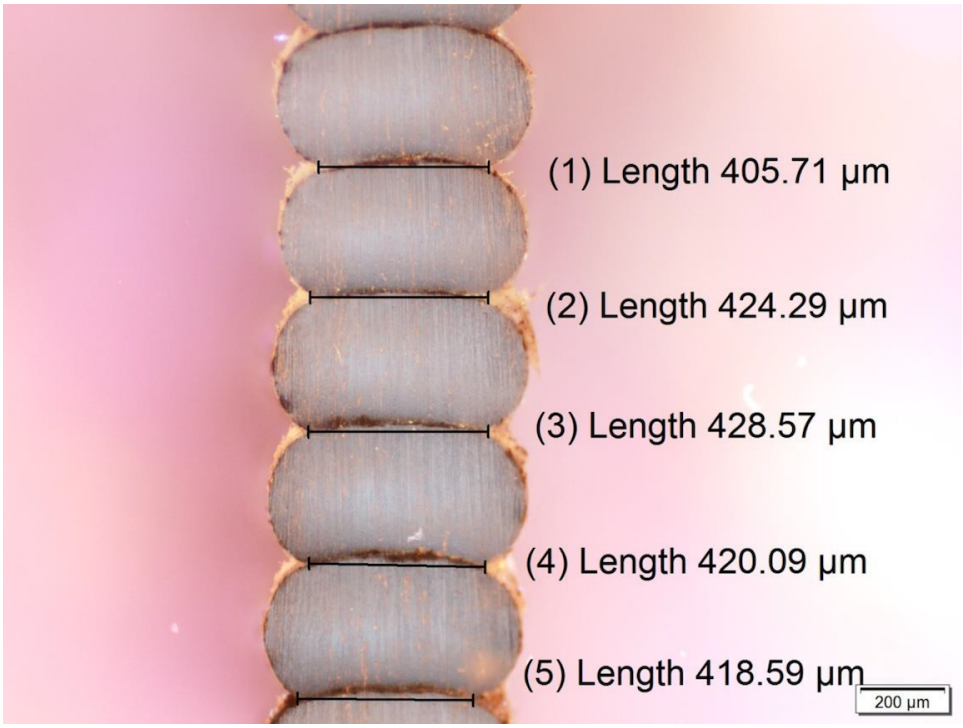

Figure 2.27: Optical microscope image of a tear test sample viewed edge-on to determine the mean weld line thickness.

The thickness for the bulk PLA hot press films was measured for each sample using a micrometer as specified by ASTM D1938. Samples were loaded into the Instron grips and pulled until the tear had propagated along the entire sample length. Load versus extension was recorded in the Instron Bluehill software. These plots were converted to fracture strength versus extension plots to normalize for the thickness of the sample. The fracture strength was calculated using the following formula:

$$S_F = \frac{2F_N}{t}$$

where S_F is the fracture strength, F_N is the normal force, and t is the thickness of the sample as determined above.

Fracture strength plots for all the samples including the bulk hot pressed PLA, printed neat and CNT control samples, and the printed LIRF-welded samples are shown in Figures 2.28 to 2.31. Note: These are fracture strength vs. tear extension tests for trouser tear tests; these are not typical stress-strain diagrams.

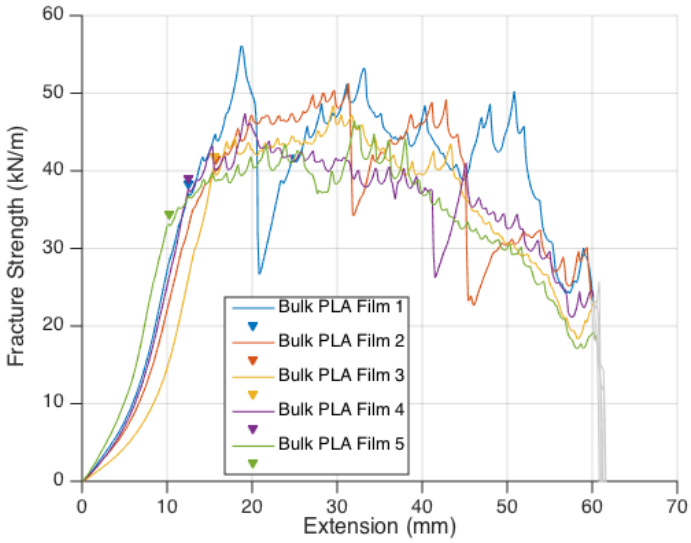

Figure 2.28: Tear test fracture strength versus extension results for bulk PLA film.

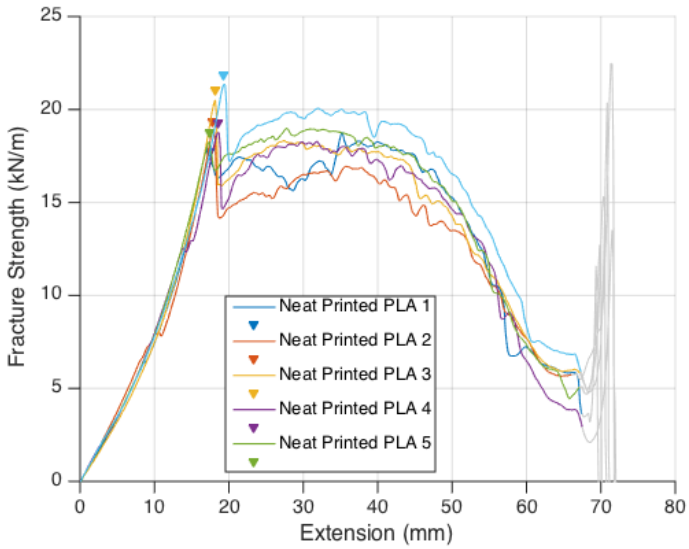

Figure 2.29: Tear test fracture strength versus extension results for neat printed PLA.

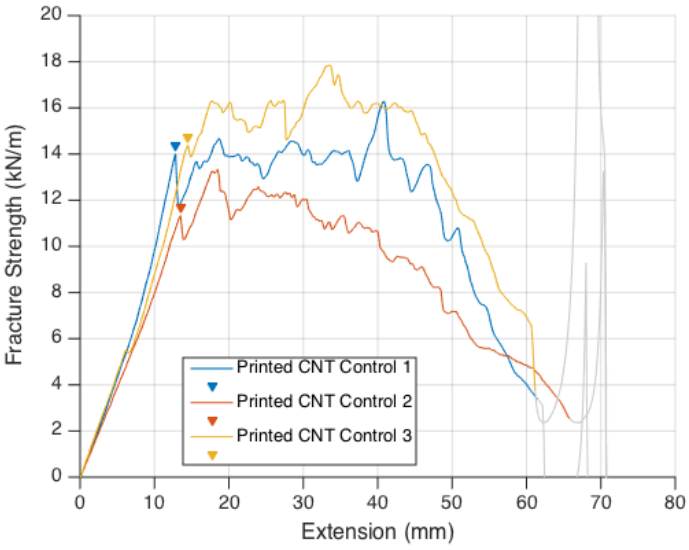

Figure 2.30: Tear test fracture strength versus extension results for CNT-coated printed PLA.

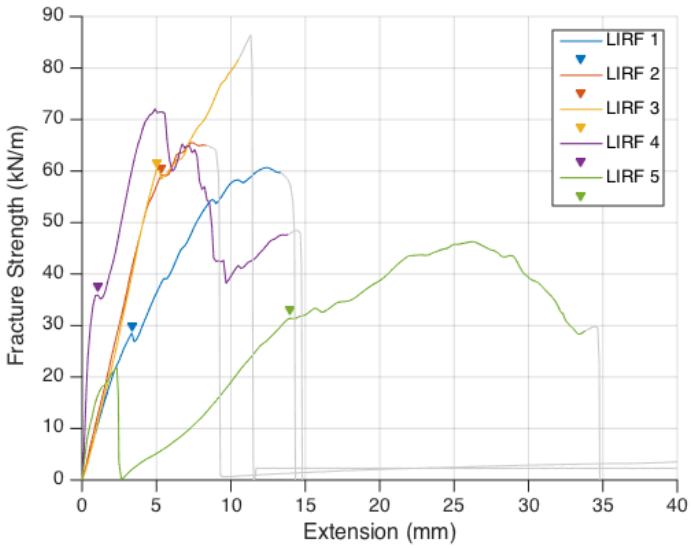

Figure 2.31: Tear test fracture strength versus extension results for CNT-coated, LIRF-welded printed PLA samples. Note the welded interface of each sample were stronger than the bulk PLA film itself and thus fractured perpendicular to the weld (tear) line.

To determine the average fracture strength value along the weld line, it is necessary to disregard the initial and final portions of the force (fracture strength) versus extension curve as specified by ASTMD1938 standards. We used MATLAB to select the first peak in the data during the linear loading of the sample tabs. This automatically selects the first slip-stick criteria as the neat film or weld line begins to fracture. The start point in the data is indicated by a triangle on each plot. For the end of test criteria, the minimum force value before the onset of tensile crazing (hardening) was determined, and data 1 mm before this point were truncated. The truncated final portions of the curve are plotted in gray. The data in between these points were averaged to determine the mean fracture strength of each tear. The average fracture energy of each sample set is plotted in Figure 2.32.

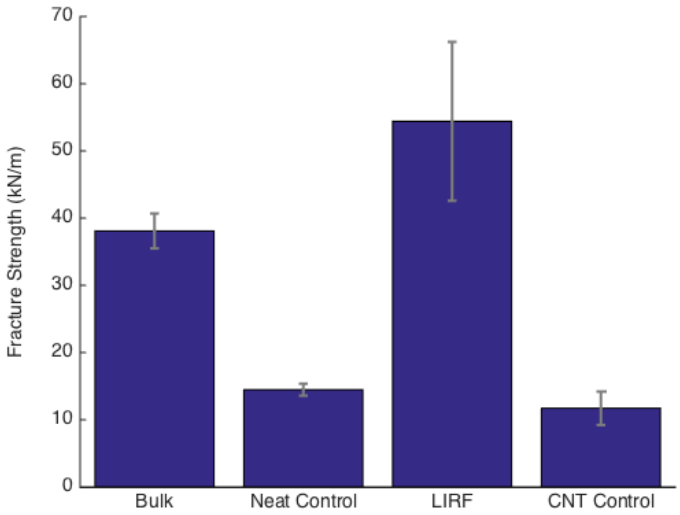

Figure 2.32: Tear test fracture strength results for each sample type. Note that the printed CNT control sample has a similar strength compared to the neat PLA sample indicating that the CNTs do not significantly impede the initial welding process during printing.

In addition, we conducted a short study analyzing the effect of nozzle temperature on the fracture strength of the neat PLA printed coupons (Figure 2.33). We did this to ensure that we used the best-case settings for the 3D-printed baseline samples. Nozzle temperatures from 200°C to 240°C were selected on the basis of the lowest temperature possible for printing the material, up to the highest temperature (240°C) where degradation of the PLA is expected to occur.

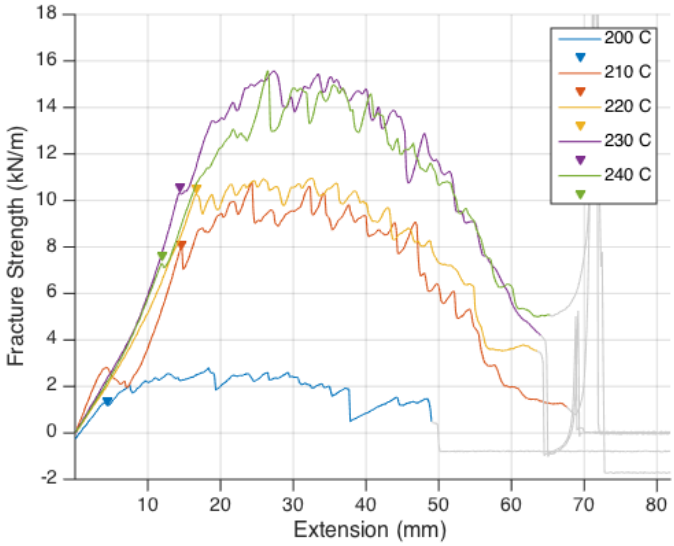

Figure 2.33: Tear test fracture strength versus extension results for nozzle temperature sweep.

As can be observed in the plots, the higher temperatures resulted in consistently stronger welds; this influenced our decision to print the control samples at the highest nozzle temperature setting of 240°C. Note that we did not use any nozzle air cooling from the fan for similar reasons; air cooling was found to reduce the fracture strength of the weld line.

2.4 Discussion

The results of these tests indicate that the LIRF welding process is a highly effective technique for strengthening the interfaces of 3D-printed parts; fracture strength increased by 275% over baseline 3D-printed parts. Both optical microscope and scanning electron microscopy (SEM) images of the fracture surfaces for the three samples (hot-pressed bulk PLA; 3D-printed neat PLA; and CNT-coated, 3D-printed, LIRF welded PLA) are shown in Figure 2.24C and Figures 2.34 to 2.41. It is clear that the bulk hot-pressed PLA sample undergoes significant plastic deformation during the propagation of the tear.

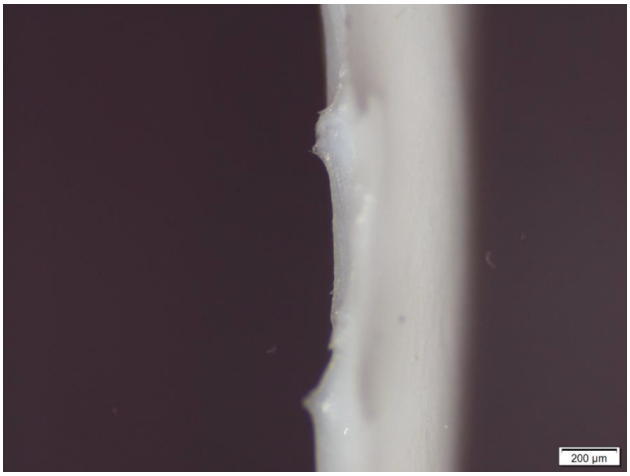

Figure 2.34: Optical microscope image of tear test fracture surface for bulk hot-pressed PLA sample (necking and crazing are clearly visible).

This plastic deformation and crazing is absent in the neat 3D-printed control sample; instead, a clean and smooth fracture surface can be seen in Figures 2.35, 2.36 and 2.37. Minor surface crazing is visible on the neat PLA printed samples at large magnifications; however, the lack of any visible bulk plastic deformation confirms the brittle fracture.

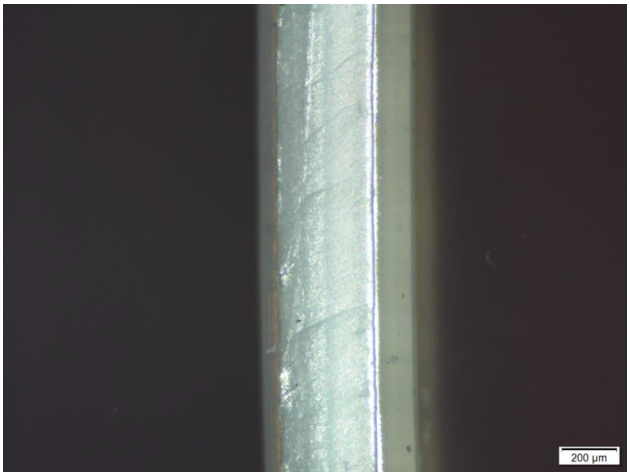

Figure 2.35: Optical microscope image of tear test fracture surface for neat 3D-printed PLA control sample (necking and crazing are absent; instead, a clean fracture surface is observed).

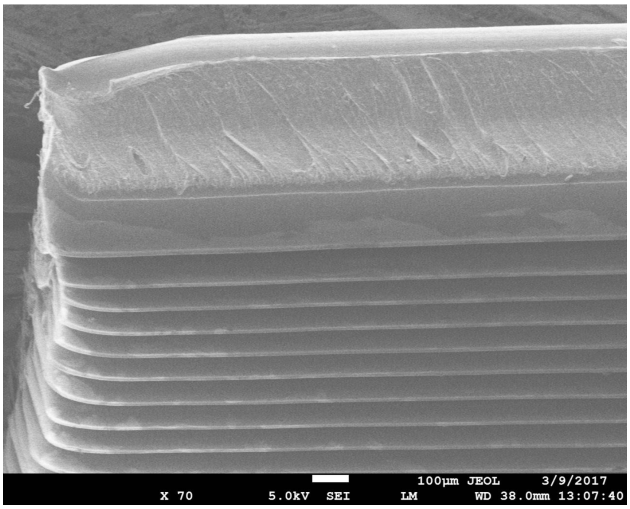

Figure 2.36: SEM image of tear test fracture surface for neat PLA 3D-printed tear samples. Note the relatively clean fracture with little to no bulk plastic deformation visible.

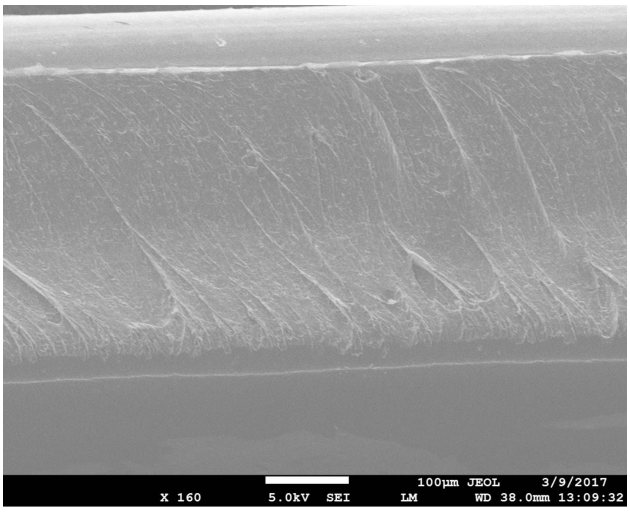

Figure 2.37: Higher magnification of 2.36. SEM image of tear test fracture surface for neat PLA 3D-printed tear samples. Shearing artifacts on the sample surface indicate the manner in which the sample was torn

In stark contrast, the fracture surfaces (Figures 2.38 to 2.41) of the LIRF-welded samples exhibit large necked zones along the tear path with significant bulk plastic deformation. The fracture surfaces of LIRF-welded samples closely resemble those of the bulk hot-pressed PLA films.

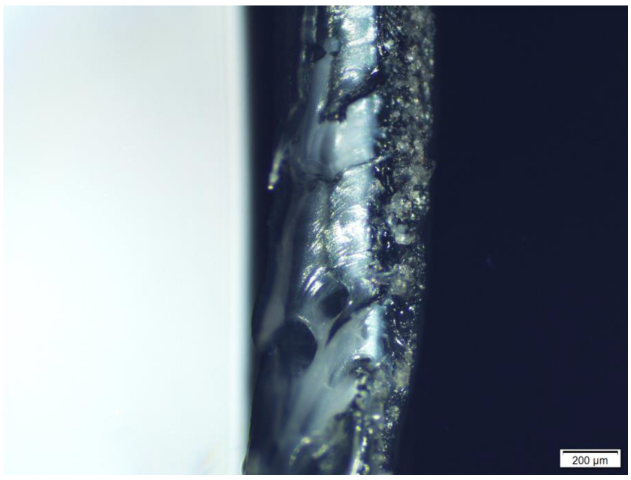

Figure 2.38: Optical microscope image of tear test fracture surface for LIRF-welded sample (necking and crazing are clearly visible).

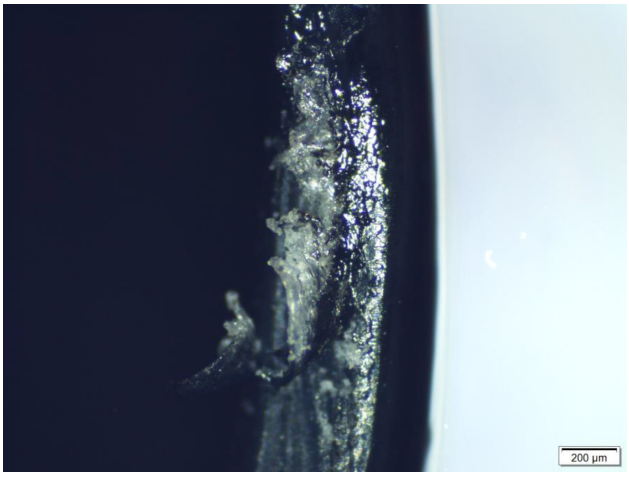

Figure 2.39: Optical microscope image of tear test fracture surface for LIRF-welded sample (necking and crazing are clearly visible).

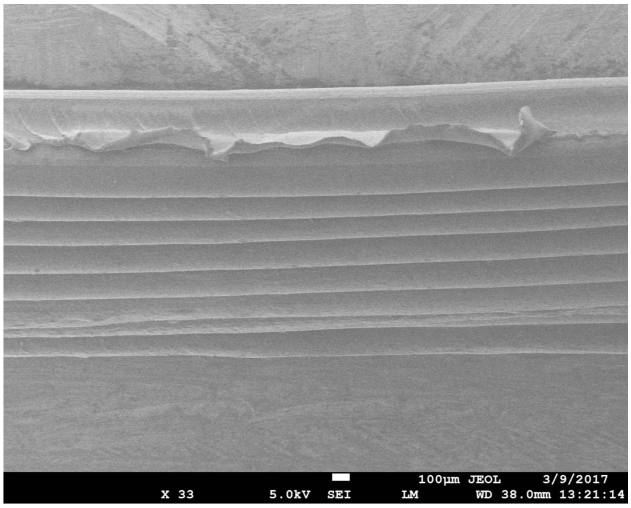

Figure 2.40: SEM image of tear test fracture surface for LIRF-welded, 3D-printed PLA tear test samples (necking and crazing are clearly visible).

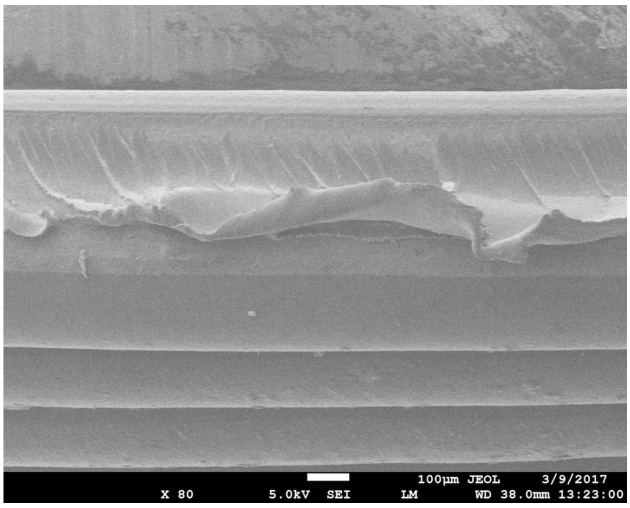

Figure 2.41: Higher magnification of 2.40. SEM image of tear test fracture surface for LIRF-welded, 3D-printed PLA tear tests. notice the large amount of bulk plastic deformation on the fracture surface which indicates the ductility restored to the sample interface after the LIRF heat treatment.

This evidence leads us to the conclusion that both the strength and ductility of the samples have been restored. The fracture strength results support this conclusion; in some of the LIRF-welded samples, the propagation of the crack along the weld line was pinned such that the crack deviated from the center line and tore diagonally or perpendicularly to the weld line. (This tendency is commonly seen in tear tests as noted in ASTM D1938 sec. 9.4.) The LIRF-welded parts outperform even the neat hot-pressed films; this suggests that the heat treatment may locally increase the crystallinity of the polymer interface or that the MWCNTs reinforce the interface after the welding process.

We highlight another important observation about the structure of the samples after the LIRF heat treatment. In the SEM images (Figures 2.40 and 2.41), one can clearly observe that the printed layers have not been structurally altered or warped after the welding has occurred. This proves that the localized heating process is capable of increasing the interlayer bond strength without sacrificing the dimensional accuracy of the part.

These enhancements in 3D-printed weld strength imply that MWCNT coatings on polymer filaments, followed by LIRF heating, can allow for 3D-printed structures with properties approaching those of conventional manufacturing. This enables load-supporting structures with complex shapes such as the 3D-printed chain link shown in Figure 2.24D. In our upcoming studies, we anticipate that this process can be extended to additive manufacturing of other thermoplastics; other electromagnetic frequencies may also be feasible for LIRF welding. Furthermore, these results indicate that conventional bulk heating of polymers to induce welding could be replaced by localized RF-responsive coatings.

3. RADIO FREQUENCY HEATING OF POLYMER NANOCOMPOSITES

3.1 Overview

Nanocomposites are becoming an important new class of industrial materials for use in high performance applications. Electrically-active nanocomposites afford unique opportunities for targeted volumetric heating upon the application of an electric field. Direct current (DC) and microwave heating methods are widely reported, however have not experienced widespread use due to the challenges and limitations of these heating methods. Radio frequency (RF) heating offers many advantages over DC and microwave heating of nanocomposite materials. Here, we give the first-ever report of RF electromagnetic heating of polymer nanocomposite materials via direct contact and capacitively-coupled electric field applicators. We present our RF heating technique for multi-walled carbon nanotube (MWCNT) thermoplastic composites and measure their broadband dielectric properties. We also demonstrate three different electric field applicator configurations and discuss their practical use in an industrial setting. Finally, we demonstrate the use of RF heating to cure an automotive-grade epoxy loaded with MWCNTs. Lap shear joints cured faster with the RF method compared to control samples cured in an oven due to the heat transfer advantages of directly heating the epoxy composite.

3.2 Introduction

Joule heating of nanocomposite materials has resulted in many unique applications for material processing, including embedded curing of composites, embedded heating elements for deicing, and localized welding of 3D printed parts [87, 88, 7]. Most work to date has focused on direct current (DC) heating [89] or microwave heating of electrically conductive nanocomposite materials [90]. Radio frequency (RF) heating, defined as approximately 3 kHz to 300 MHz, is a largely unexplored method for heating of nanocomposite

materials. Much of the historic industrial use and research on RF heating was focused on food processing [91, 92, 93, 94], RF bonding or curing of materials [95, 96], drying of raw materials [97], and biomedical hyperthermia or ablation [98, 99, 100]. Thermoset adhesives with high dielectric loss have been cured using high power RF energy [101]. To date most of the literature has focused on RF heating of nanocomposites for hyperthermia applications [102, 103, 104], or inductively-coupled RF heating of nanocomposites [105, 106]. In comparison to DC or microwave heating, the benefits of capacitively-coupled RF heating include: (i) the flexibility to directly or remotely couple electromagnetic energy to a nanocomposite material, (ii) the ability to more efficiently transfer energy to the material due to capacitive coupling, (iii) the option to use sub-percolation loading levels of nanoparticle fillers, and (iv) reduction of safety concerns compared to microwaves by decreasing stray electromagnetic radiation [107].

Perhaps the simplest method for Joule heating a conductive nanocomposite material is to connect the composite to a direct current or line frequency (50-60 Hz) voltage source. Nearly all electric heating elements used in consumer or industrial applications operate in this manner. A notable example is the work from Lee and Wardle et al. who used DC heating to cure composite panels out-of-oven with embedded CNT films [108]. There are, however, two major draw-backs associated with DC Joule heating. First, the resistive material needs to be directly connected to the circuit with conductive electrodes, and second, the material needs to have a relatively high conductivity to pass a current through the material. High frequency alternating electric fields may also be used to excite currents in conductive composite materials for heating applications. Microwave heating of nanocomposite materials utilizes electromagnetic energy between 300 MHz and 300 GHz to heat lossy dielectrics and has the benefits of being able to remotely heat the target material with high energy density [109, 110]. Even so, heating parts uniformly with microwaves is difficult, and shielding requirements present challenges for practical applications to pre-

vent the dangerous emission of microwave energy [107]. Here we demonstrate a novel technique for heating nanocomposite materials with RF energy. We measure the RF electrical properties of CNT and polylactide (PLA) melt compounded nanocomposite films and evaluate various electric filed applicators for heating the films. We show that direct contact, parallel plate, and fringing field applicator geometries are all capable of heating nanotube composites at high heating rates. A practical example of curing a high strength epoxy loaded with CNTs in a lap shear joint configuration is shown. In this case, the aluminum lap shear coupons serve as the direct contact electrodes used to apply the RF energy to the epoxy nanocomposite. Due to the volumetric heating capability of the RF method, the RF-cured lap shear samples reached green strength in 3 minutes as opposed to 5 minutes for a conventional oven curing method. We anticipate wide applicability in the industrial manufacturing sector.

3.3 Results and discussion

3.3.1 Sample preparation

Carbon nanotube polylactide (PLA) composite films (Figure 3.1) were prepared via melt compounding. Starting with a 10.0 wt% MWCNT/PLA masterbatch (Nanocyl SA, custom batch), various dilutions were melt compounded into neat PLA (NatureWorks LLC, 3D850) with a micro-conical twin screw compounder (Thermo Fisher Scientific Inc., HAAKE MiniCTW).

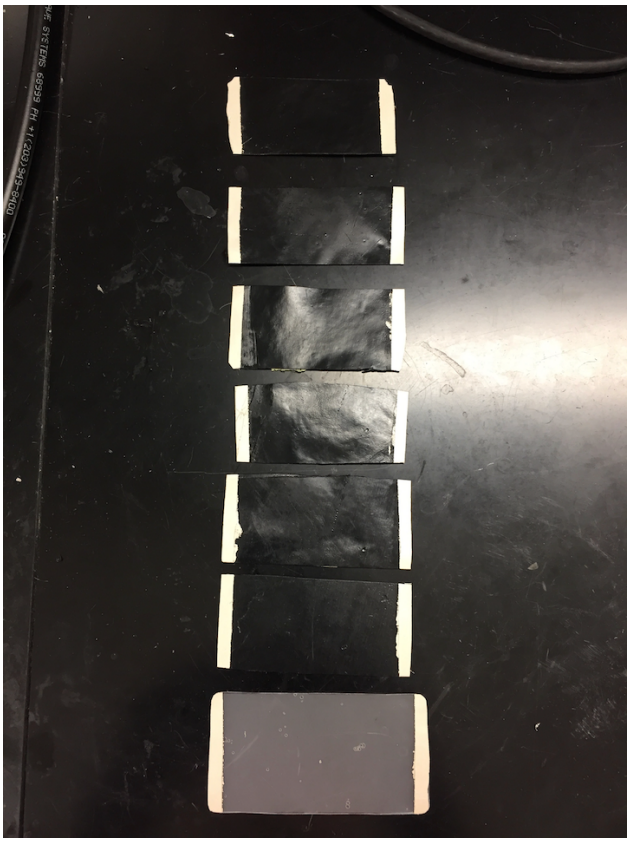

Figure 3.1: Hot pressed films used for the RF measurement and heating experiments. The samples have silver electrodes painted on the edges for direct contact RF heating.

Prior to compounding, the polymer samples were thoroughly dried per the manufacturer's specifications. Samples were melt compounded for approximately 4 minutes at 215 °C before the die was opened and the sample allowed to extrude. The nanocomposite dilutions were then hot-pressed (Carver Inc., model 3856) into uniform 0.5 mm thick films at 150 °C and 27.6 MPa. Rectangular samples 3 x 5 cm were cut from the films and silver electrodes were painted onto the edges to aid in contact to the RF applicator cables.

3.3.2 Electrical characterization

To fully understand the RF heating response of the polymer CNT composite materials, we first characterized the hot pressed films in the RF region. The complex permittivity

was measured using a capacitive sample holder consisting of two conducting cylindrical disks (Figure 3.2) and a network analyzer.

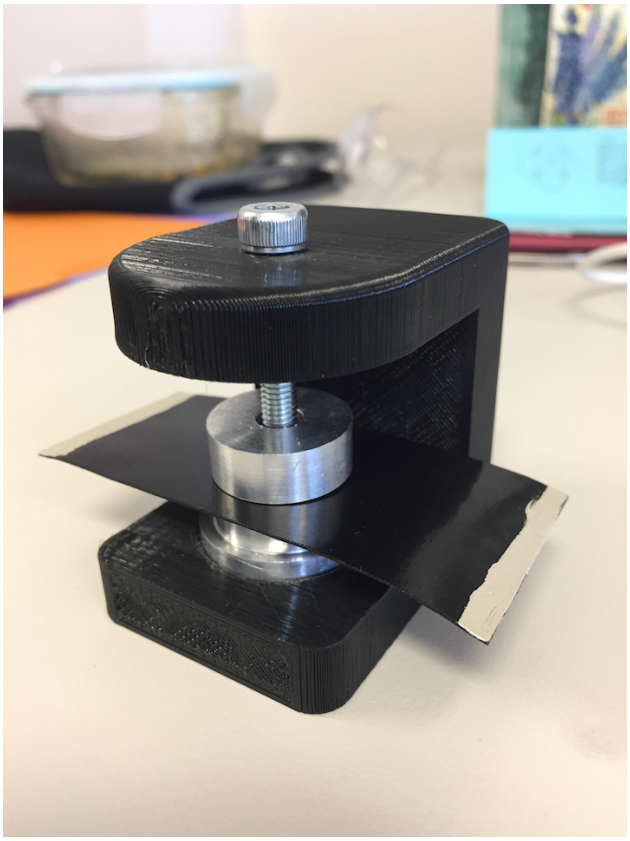

Figure 3.2: 3D printed radio frequency dielectric measurement jig for hot pressed film samples

An adapter was used to convert N-type coaxial connection from the network analyzer to two parallel prongs to connect to the capacitor disks. In the measurement, the sample under test is placed between the two disks and the scattering parameter S11 is acquired for the desired frequency range. A calibration procedure was used to account for the connecting cables and the adapter and capacitor parasitics. The capacitor impedance is obtained from the measured S11 parameter, which is then used to compute the complex

permittivity, taking into account the fringing fields.

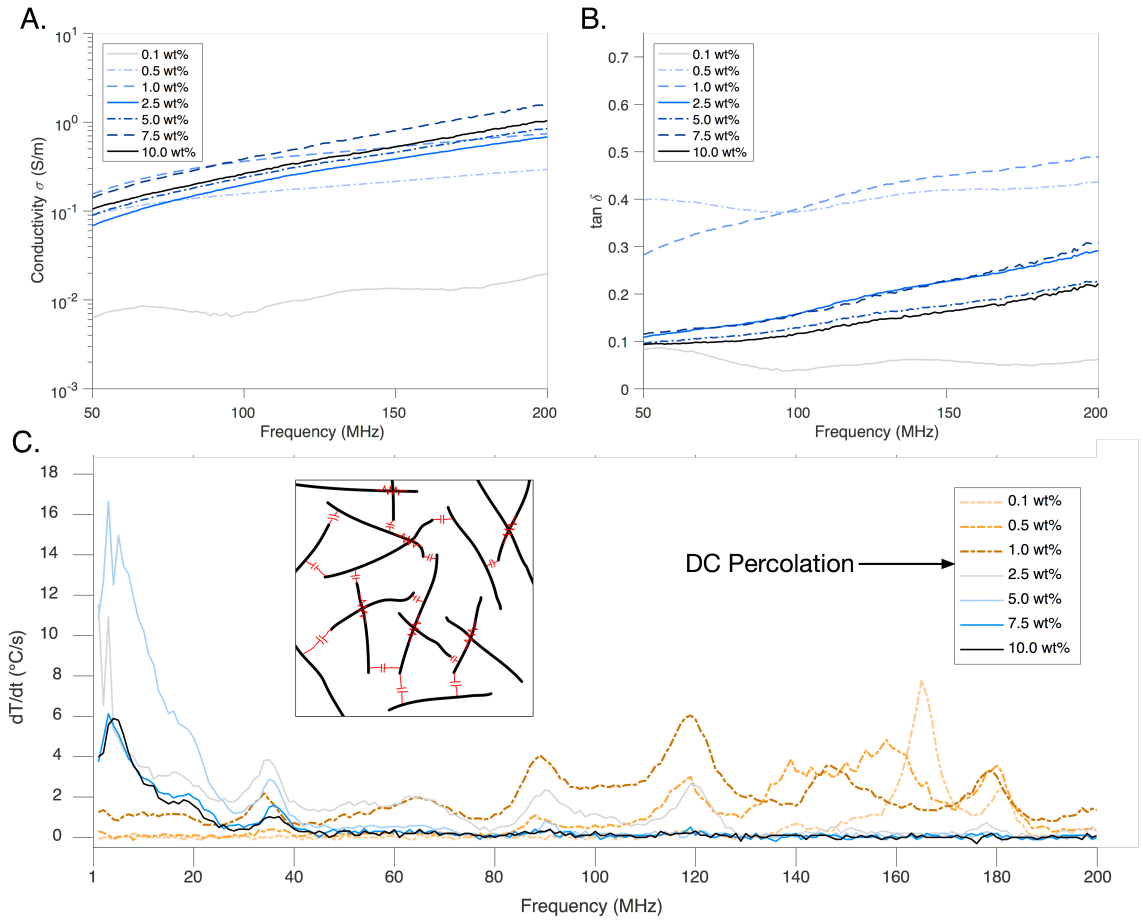

Figure 3.3: Dielectric spectroscopy results including conductivity (A) loss tangent (B) of MWCNT/PLA hot pressed films 50 to 200 MHz. Calculated heating rate dT/dt vs. frequency plot (C) for MWCNT/PLA composite films heated via direct-contact RF energy (C inset: RC CNT network illustration).

The real part of the electrical conductivity and loss tangent as a function of frequency from 50 to 200 MHz are plotted in Figure 3.3A and 3.3B (the real part of the relative permittivity is shown in Figure 3.4).

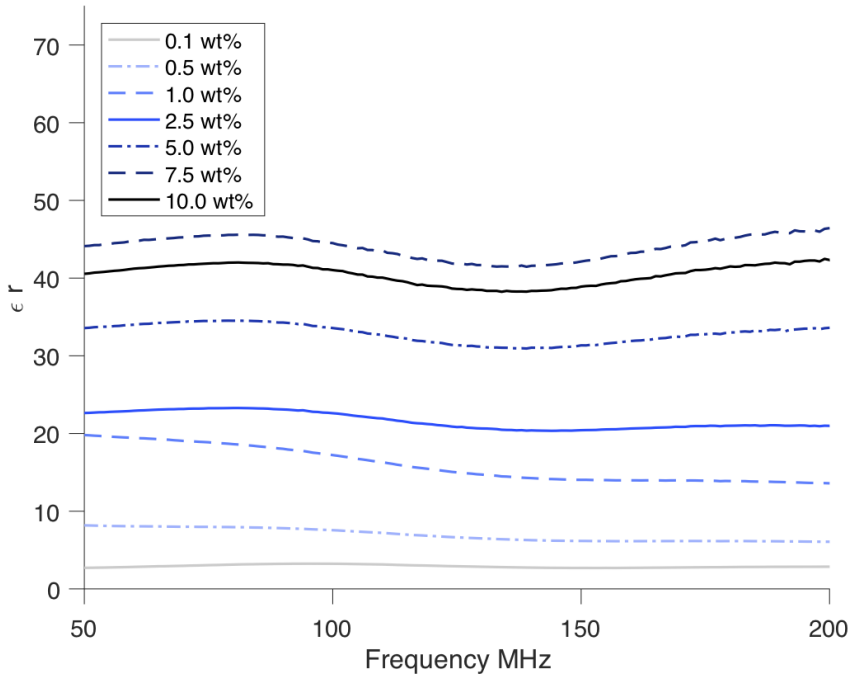

Figure 3.4: Real part of the relative permittivity vs. frequency for various weight percentages of CNT/PLA composite films.

A large increase in conductivity is observed from 0.1 wt% to 0.5 wt%. The shifted onset of a pseudoconductive network to lower loading levels is explained by the capacitive coupling of isolated carbon nanotubes that may now contribute to the materials volume conductivity. This is in contrast to DC percolation behavior where CNTs must be proximally close enough to enable electron hopping or tunneling from CNT to CNT [111]. The loss tangent of the composite films (Figure 3.3B) reveals that the 0.5 wt% and 1 wt% loaded films are the most lossy and therefore well suited for broadband radio-frequency heating across the measured spectrum [112].

3.3.3 Thermographic spectroscopy

Radio frequency power was applied to the samples with a signal generator (Rigol Inc., DSG815) and 500 W amplifier (Prana R&D, GN500D) shown in Figure 3.5.

Figure 3.5: RF signal generator and amplifier equipment

The samples were connected to the amplifier with a 50 coaxial transmission line terminated by a Type N bulkhead connector with alligator clips soldered to the center pin and ground reference. Samples were placed in a custom laminar airflow box to have a consistent advective cooling rate across all samples. The samples were directly monitored with a FLIR infrared camera system (FLIR Systems Inc., A655sc). To test the frequency

dependent heating response of the samples and the RF power equipment, a step-wise heat-cool frequency sweep was programmed into the signal generator. Frequencies from 1-200 MHz were swept such that power at 40 dBm (10 W) is applied for 2 seconds, followed by 13 seconds of cooling before moving to the next 1 MHz incremental step. The heating rates as a function of frequency were determined by selecting the points when the power is switched on and 1 second into each cycle and calculating the slope between the points as shown in Figure 3.6.

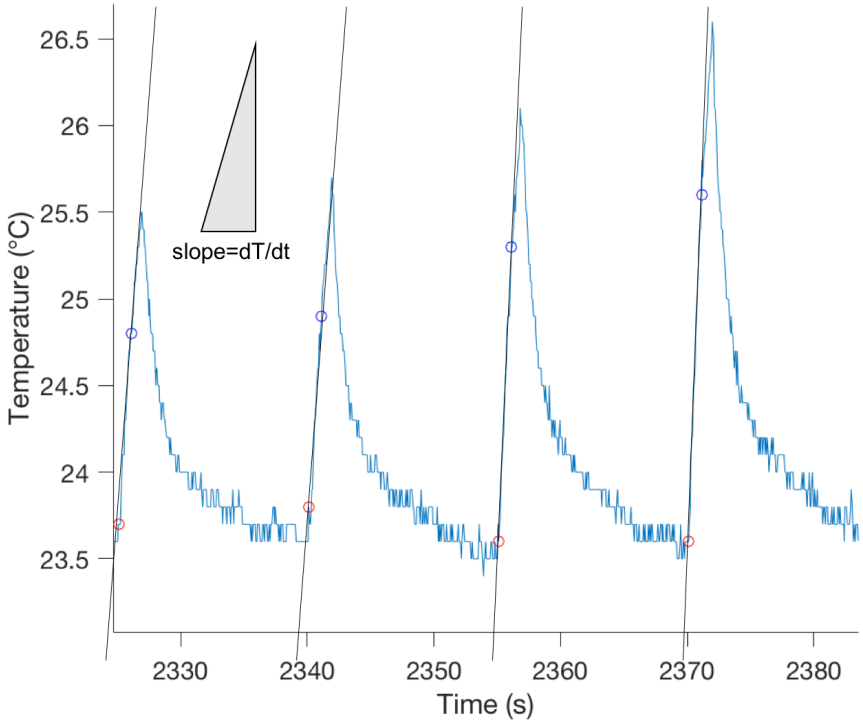

Figure 3.6: Close-up view of thermographic spectroscopy data for 0.1wt% hot pressed film sample showing how the heating rate was calculated

Heating rates as a function of frequency for the PLA/CNT composite films heated with direct contact RF power from 1 to 200 MHz are shown in Figure 3.3C. All samples from

0.1 wt% to 10 wt% efficiently couple to and heat in response to the applied RF energy. This result is surprising when compared with microwave heating of similar CNT composite films. We previously demonstrated that samples below 1 wt% heat very little in response to microwave energy, and samples above 5 wt% begin to reflect incident microwave energy and thus heat less [7]. The 5 wt% composite film achieved the highest heating rate of 16°C/s. All samples display heating rates that are highly dependent on frequency with notable resonant modes. Resonant modes common to at least two samples are centered at approximately 5 MHz, 35 MHz, 90 MHz, 120 MHz, and 180 MHz. As a general trend, the lower weight percent composite samples couple well at higher frequencies, and conversely, the higher weight percent composites couple at lower frequencies.

The two main factors that contribute to the observed resonant modes are the impedance of the composite films and the characteristics of RF amplifier circuit. The CNT composite samples follow classic percolation models, and exhibit complex capacitive impedance, especially at lower loading levels. Based on the heating rate results in Figure 3.3C, there exists a clear distinction between films above and below the percolation threshold. The higher weight percent films have a higher degree of percolation and resistive interconnects between carbon nanotubes dispersed in the matrix. The films with lower loading are below the classic DC percolation threshold value, and are therefore composed of a predominantly disjointed network of carbon nanotubes. Such a network may be represented by a combination of resistors and capacitors in series and parallel (Figure 3.3C inset). The greater the contribution from capacitive effects, the more sensitive the heating rate will be to the resonant frequency of the power supply and overall circuit. Because of this, most practical RF heating equipment will implement an automatic matching network to ensure power is effectively coupled to the load [113, 114, 115].

3.3.4 Quality factor and matching

Perhaps the most important consideration for effectively heating nanocomposite materials with RF energy is the concept of impedance matching. Nanocomposite materials pose a unique challenge for matching, largely because their electrical properties can change over many orders of magnitude with small changes in composition or processing conditions. Additionally, nanocomposites are complex materials with both resistance and capacitance (inductive component is negligible for non-magnetic nanocomposites). Maximum power is transferred from the RF source to the load when the load impedance Z_L is equal to the complex conjugate of the RF source impedance Z_S*, which is the Thévenin equivalent circuit.

$$Z_S = Z_L*$$

This implies that the real part of the impedances (the resistance R) must equal each other and the imaginary part of the impedances (the reactance X) must cancel.

$$Z = R + iX$$

$$R_S = R_L$$

$$X_S = -X_L$$

Where R_S is the source resistance, R_L is the load resistance, X_S is the source reactance, X_L is the load reactance. The resistive term is frequency independent, and is equal to the DC resistivity for a given sample geometry. It is important to note that the load impedance includes both the sample impedance, and the impedance of the cables and other circuit elements used to connect the sample to the load; it is thus a lumped sum equivalent circuit.

The complex impedance of the load Z_L may be defined as:

$$Z_L = R_L + iX_L = R_L + i(\omega L_L - \frac{1}{\omega C_L})$$

where is the angular frequency given by $\omega = 2\pi f$. When the inductive and capacitive reactances are equal, the system is said to be at resonance. The resonance frequency of a series RLC circuit is given by:

$$\omega_r = \frac{1}{\sqrt{LC}}$$

The RF source generally has a fixed resistance and reactance, and most commercial systems are designed to have an impedance of 50 Ohms. For our samples, the reactance is highly dependent on frequency, so these terms may be balanced to allow for efficient coupling by using frequency variation (as measured by heating rate in Figure 3.3C). This could be used to employ RF-based curing of CNT/epoxy systems at low loadings, where samples with sub-percolation loadings may still strongly couple to fields with the appropriately matched resonant frequency.

In contrast, most industrial RF heating systems employ an operating frequency within one of the defined industrial, scientific, and medicine (ISM) bands designated for commercial use by the International Telecommunication Union (ITU) Radio Regulations (RR). Of the available bands, 13.56 MHz, 27.12 MHz, and 40.68 MHz are commonly used for heating [107]. In these cases, efficient heating could be accomplished through impedance matching, which is typically carried out with a matching network composed of variable inductor and capacitor elements either manually or automatically controlled.

Our system can be tuned based on composition of the nanocomposite rather than through the use of a matching network alone. This is also important because even matched systems that are as efficient as possible may be unable to heat a target material with low

dielectric or resistive loss, i.e. an epoxy system that would normally require very high power levels to heat, could be made to heat at much lower power levels with the addition of a nanocomposite filler.

3.3.5 Applicator techniques

Demonstrations of both contact and non-contact RF heating were carried out on the composite films. The direct contact method is the same as that used for the thermographic spectroscopy technique. Silver electrodes were painted onto the edges of the composite films and connected to the RF amplifier with alligator clips; one electrode is grounded and the other carries the sinusoidal RF signal (Figure 3.7A). For the non-contact methods, we utilize the electric fields produced between the ground and RF signal lines to induce a time-varying electric field in the composite films resulting in resistive heating.

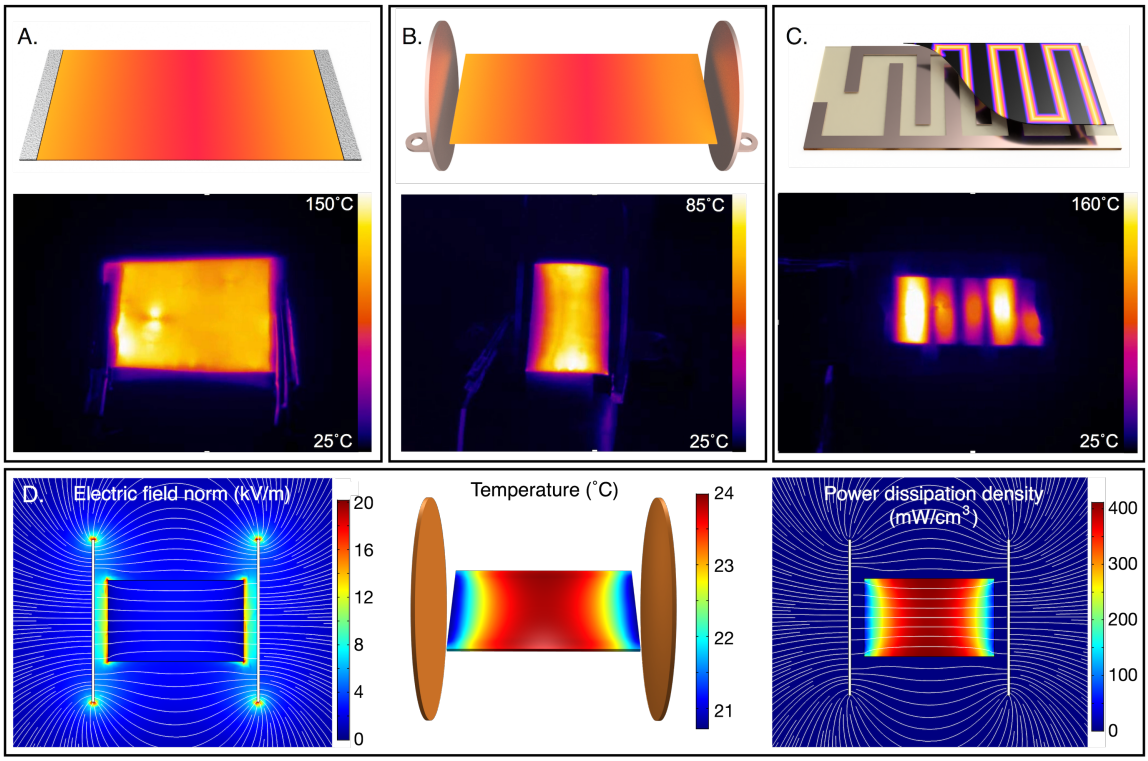

Figure 3.7: Geometry illustrations (top) and corresponding FLIR thermal image (bottom) showing the three RF electric field applicator configurations: direct contact (A) parallel plate (B) and interdigitated fringing field (C). COMSOL models (D) showing electric field strength around the sample and near the electrodes (bottom left) the heat generated in a sample (bottom middle) and the power dissipation density (bottom right).

We demonstrate both a parallel plate capacitor-like arrangement (Figure 3.7B), and a planar interdigitated fringing-field applicator (Figure 3.7C). The parallel plate system consists of two copper discs approximately 5 cm in diameter fixed to an insulating support bar. One disc is grounded the other is connected to the center pin of the coaxial cable from the RF power source. Samples are placed in-between the discs without physically touching either electrode. For the fringing field applicator, copper tape 5 mm in width was laid down on a polyetherimide sheet to create a pattern of interdigitated fingers. The copper was covered with an insulating layer of Kapton tape and soldered to the ground

and center pin of a Type N bulkhead connector. Thin composite samples were heated by placing them parallel to the interdigitated applicator within approximately 5 mm from the surface of the applicator.

In all three cases, the samples heat rapidly in response to the applied electric field with heating rates over 100°C/s observed in response to power levels of a few hundred watts. The direct contact configuration in Figure 2A shows the heat generated in a 1.0 wt% CNT PLA film at 315 W applied power at 100 MHz after 4 seconds of applied power. This is the simplest RF field application method and was generally least sensitive to factors such as film orientation in the electric field. The non-contact heating results are similarly energetic. We used a 7.5 wt% CNT PLA film and applied 100 W of power at 100 MHz; Figure 2B shows the heat generated in the film after 6 seconds. This applicator configuration would be very useful for targeted heating of a material that is embedded or otherwise inaccessible to directly contact with metallic electrodes. Another useful application could be the efficient and direct heating of a nanocomposite material in a tube furnace where indirect heating via an oven is typically implemented. Finally we show an interdigitated fringing field applicator heating a 1.0 wt% CNT PLA film at 315 W applied power at 50 MHz and the intense heat generated after 1 second (Figure 3.7C). Such a fringing field applicator is specifically useful for heating planar materials moving in reference to each other (either the material moves relative to the fringing field applicator or vice versa). The act of scanning the fringing field parallel to the field lines serves to uniformly heat the sheet or film. This configuration may find uses in heat treating nanocomposite thin films, thermographically characterizing the electrical properties of printed electronics, and processing continuous feeds of materials.

Both non-contact methods are operated in an electrically small configuration; that is the dimensions of the applicator are less than one-eighth the wavelength of the applied RF field (at 200 MHz the wavelength is approximately 1.5 m) [107]. Because of this,

the electric fields generated between the plates or interdigitated fingers cannot establish standing waves, and so are highly uniform in nature.

3.3.6 COMSOL modeling

The applicator configurations discussed were modeled in COMSOL to develop a better understanding of the electric field distribution in the samples and the coupled heat generated by the RF energy. Modeling the applicator geometry and sample to be heated can be a valuable tool for creating an efficient and effective RF heating module in a real-world application. For this geometry, we modeled the electric field with a lumped port, and assume a power input of 100 W; for a 50 Ohm system this results in a peak voltage input of 100V. The dielectric properties of the film were taken from the measurements we performed earlier. Using the COMSOL Multiphysics RF and heat modules, we calculated the electric field distribution in the film and coupled that with the material dielectric properties to determine the power dissipation and thus the temperature rise in the material. We show in Figure 3.7D the electric field distribution (left), the temperature rise (middle), and power dissipation density (right) for a capacitively-coupled parallel plate applicator. Calculating the maximum predicted electric field strength is important to ensure that the system is operated well below the dielectric breakdown voltage of air (approximately 3 MV/m) and the breakdown strength of the composite materials to be heated. Outside the sample, the maximum electric field concentrates around the sharp edges of the applicator plates and the corners of the sample. In spite of this, the maximum power dissipation and temperature rise are observed in the center of the sample for both the simulation and experiments. Another observation from the electric field lines is their relative uniformity inside the parallel applicator plates. A more uniform electric field results in more uniform and consistent heating across various samples. This is in contrast to the results we previously showed for microwave waveguide heating of composite films where heating uniformity

was highly dependent on the dielectric properties of the film [7, 116].

3.3.7 Application to rapid bonding

3.3.7.1 Lap shear adhesive samples bonded with RF

We now demonstrate an automotive- and aerospace-focused application of this technology by bonding aluminum sheets with a high performance epoxy adhesive loaded with carbon nanotubes (Figure 3.15). It is highly desirable to bond aluminum and composite parts with high-performance adhesives instead of rivets or traditional welds [117, 118, 119]. Properly selected adhesives outperform both welds and mechanical fasteners in regard to mechanical strength, impact and fatigue resistance as well as weight. Historically, the one-part epoxies used to bond vehicle components required cure temperatures of 180°C for 30 minutes to reach full strength [120]. This required the components to be placed in large ovens, draped with heater blankets, hot air guns, or infrared heaters to achieve the desired degree of cure. With our RF curing technique, the epoxy adhesive composite volumetrically generates the required heat for curing because of Joule heating of the embedded CNTs.

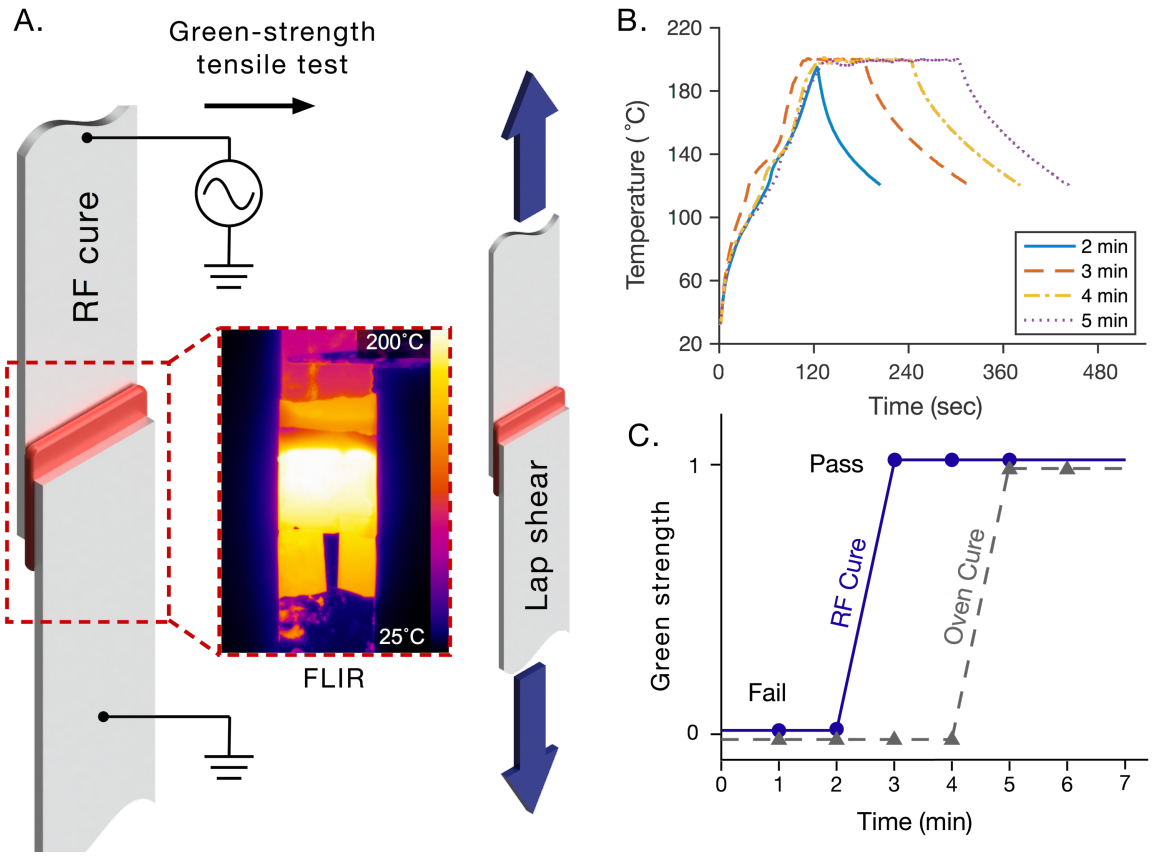

Figure 3.8: Lap shear strength sample geometry showing the RF applicator technique, and the thermal profile recorded with a FLIR camera (A). Temperature profile as a function of RF cure time recorded by the FLIR camera (B). Time to reach equivalent green strength for traditional oven cure and RF curing technique (C).

Aluminum strips (ThyssenKrupp Materials NA Inc., 7075 T6) 1mm thick and 25.4 mm wide by 152.4 mm long were bonded using a single-part high temperature cure epoxy (Betamate Flex 100, DowDuPont Inc.) loaded with MWCNTs (Cheap Tubes Inc.). The epoxy and CNTs (0.25 wt%) were mixed with a planetary centrifugal mixer (AR-100, THINKY USA, Inc.) at 2000 RPM for 15 minutes. The CNT loading level of 0.25wt% is below the classical DC percolation threshold, and yet still couples effectively with the RF power source.

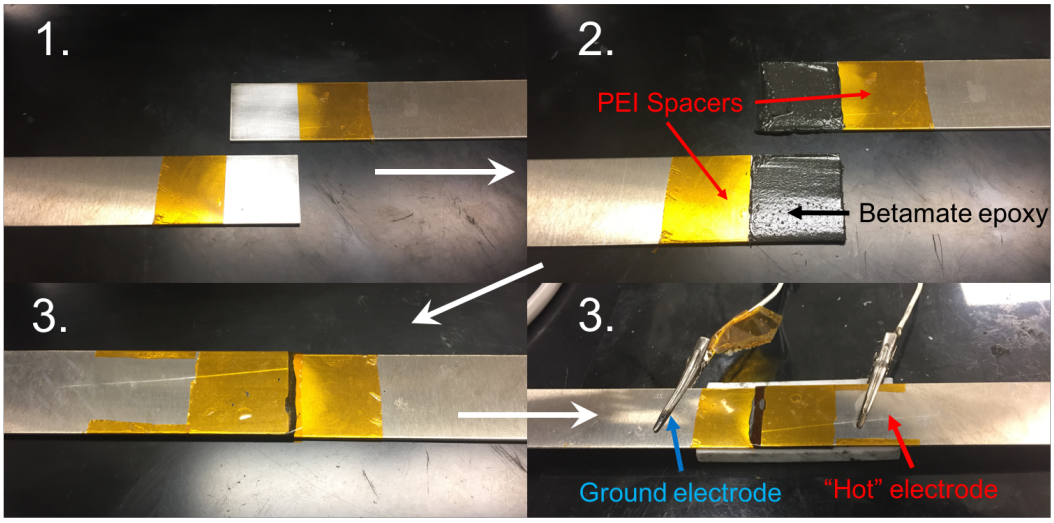

Figure 3.9: Lap shear assembly process 1. Overlap area masked with PI tape 2. Betamate/CNT epoxy composite added and PEI spacers inserted 3. Two halves pressed together and held in place with PI tape 4. Electrodes attached to each lap shear strip with alligator clips

Lap shear samples were prepared for lap shear strength according to ASTM D1002 (Figure 3.9). Polyetherimide (PEI) spacers were inserted on both edges of the lap shear samples to ensure a consistent bond line thickness was maintained for every sample. A strip of Kapton polyimide (PI) tape was used to clamp the strips in position during the curing procedure. For the RF cured samples, the prepared specimens were connected to the RF amplifier by grounding one of the aluminum strips and connecting the other to the center pin of the Type N bulkhead connector.

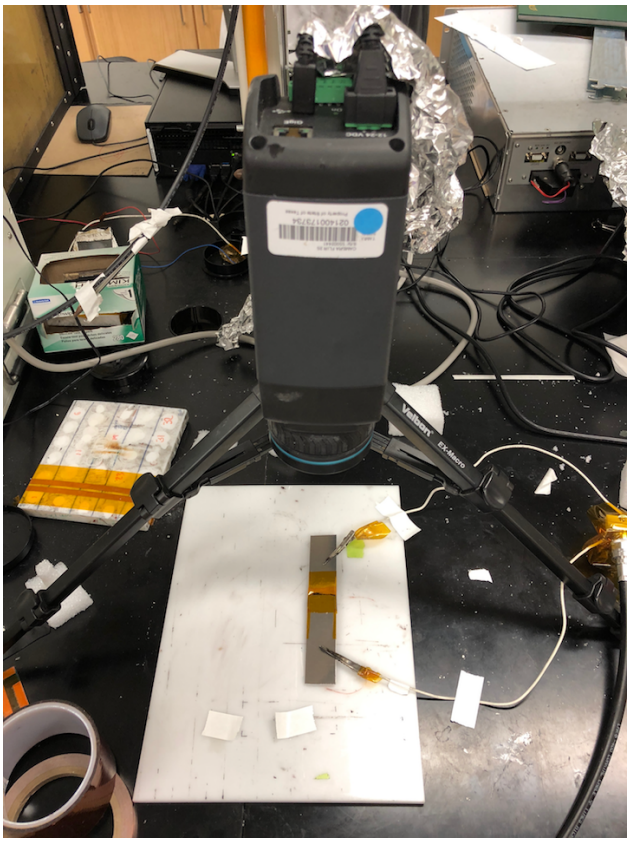

Figure 3.10: Setup for monitoring lap shear temperature with FLIR camera.

The applied power was approximately 10-100 W at 44 MHz throughout the curing process and was manually controlled by directly observing the temperature of the samples with a FLIR camera and the power level adjusted to achieve a desired thermal cure profile (Figures 3.10 and 3.8B). Our RF curing method allowed the sample to be brought up to the desired cure temperature of 200°C within 2 minutes by applying up to 100 Watts of RF power at 44 MHz.

The samples all had an initial heating rate of approximately 5°C/s, similar to the direct-contact hot pressed films shown in the previous section. The heating rate is determined by the applied RF power minus heat flux to the components being joined. The maximum heating rate is governed by the dielectric breakdown strength of the epoxy CNT composite,

the degradation temperature of the epoxy, or other thermal considerations for the components to be joined. At higher loading levels (>0.5 wt%) we did in fact observe dielectric breakdown and arcing events if the power level (and thus the electric field) was raised too high. Using low CNT filler loading levels, an adhesive with higher dielectric breakdown strength, or more sophisticated RF equipment may all help to mitigate breakdown events.

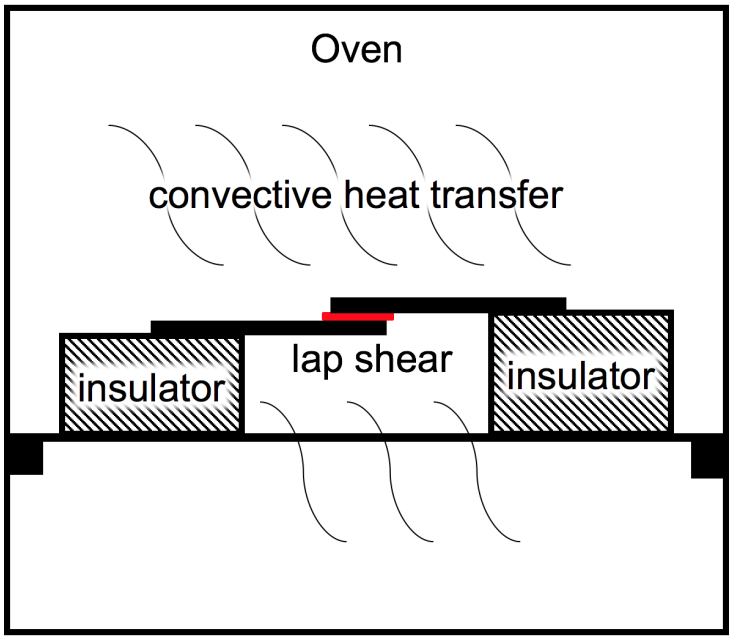

Figure 3.11: Diagram of oven control test for curing lap shear samples. Convective heat transfer dominates.

Control samples were cured in an oven according to the manufactures recommended processing conditions. The samples were suspended across thermally insulating alumina bricks to ensure convention heating dominated rather than thermal conduction through the aluminum strips (Figure 3.11). The oven was pre-heated to 200°C and samples were timed according to the total residence time in the oven, ranging from 2-6 minutes.

The green strength of the joint was assessed by curing the specimen at a specified time at 200°C, followed by immediately weighting the lap shear specimen with 8.2 kg (Figure 3.12).

Figure 3.12: Weight and tensile grip mass measured at 8.2 kg, used for the green strength test in this study

Samples that could hold the weight without measurable joint displacement were defined as having reached their green strength, conversely, if the lap shear joint failed, the specimen was defined as failing the green strength.

After 3 minutes of heating, the RF-cured sample passed a green strength test, holding an 8.2 kg mass for a minimum of 30 seconds; the sample continued to hold the weight for

30 minutes before we removed the grips (Figure 3.13 and 3.14).

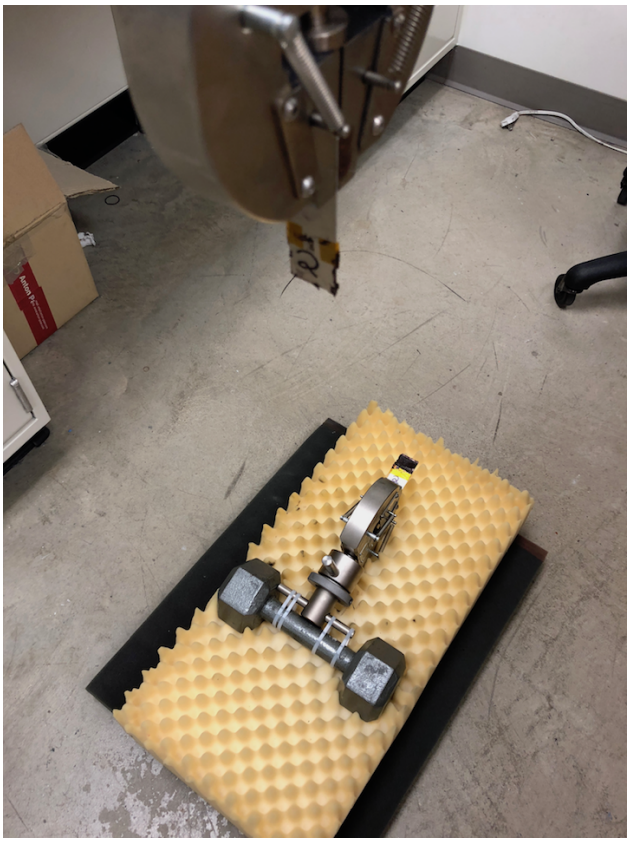

Figure 3.13: Green strength test for the 2 min RF lap shear sample, the sample failed after a few seconds of having the weight applied

Figure 3.14: Green strength test for the 3 min RF lap shear sample, the sample held the weight for approximately 30 min without failing

The remaining RF lap shear samples cured for 4 and 5 minutes each passed the green strength test (Figure 3.8C). In contrast, the control samples (cured via convective heat transfer in an oven set to 200°C) took 5 minutes to cure to green strength. After 4 minutes, the lap shear sample had begun to cure; however the sample slipped via adhesive failure after a few seconds of the grips and weight being applied.

This difference between the RF curing and oven curing process is best explained by the heat transfer mechanisms at work. In the RF curing technique, heat is generated volumetrically within the adhesive system itself via capacitively-coupled Joule heating of the sub-percolated CNT network. In the oven curing technique, the limiting factor is the

convective heat transfer to the aluminum strips and the conduction heating into the epoxy. Epoxies, as well as most adhesive systems, are poor thermal conductors and share the same rate limiting steps governed by Fouriers law. Especially in the automotive manufacturing sector where cycle times dictate which technologies are production-ready, volumetric RF curing of nanocomposite epoxies offers great incentives for rapid curing of adhesive joints.

Besides using less active filler material, the low loading levels of CNTs ensure the adhesive maintains its inherent mechanical properties, and is not significantly embrittled. This is also advantageous from a cost perspective by limiting the amount of nanomaterial filler necessary to achieve sufficient heating performance. Additional advantages for industrial applications include a large reduction in capital equipment costs typically associated with large ovens, custom tooling, and other heating elements. This heating method is highly efficient from an energy perspective since heat is generated directly within the target material; similar to induction heating, excessive heat losses are thus minimized [121].

3.3.7.2 Example: RF bonding of model truck

In Figure 3.15, we show an example of a model truck being bonded together with the RF technique we developed. The truck bed was removed with a metal cut-off wheel (Figure 3.15B) and prepared with the CNT-loaded Betamate epoxy.

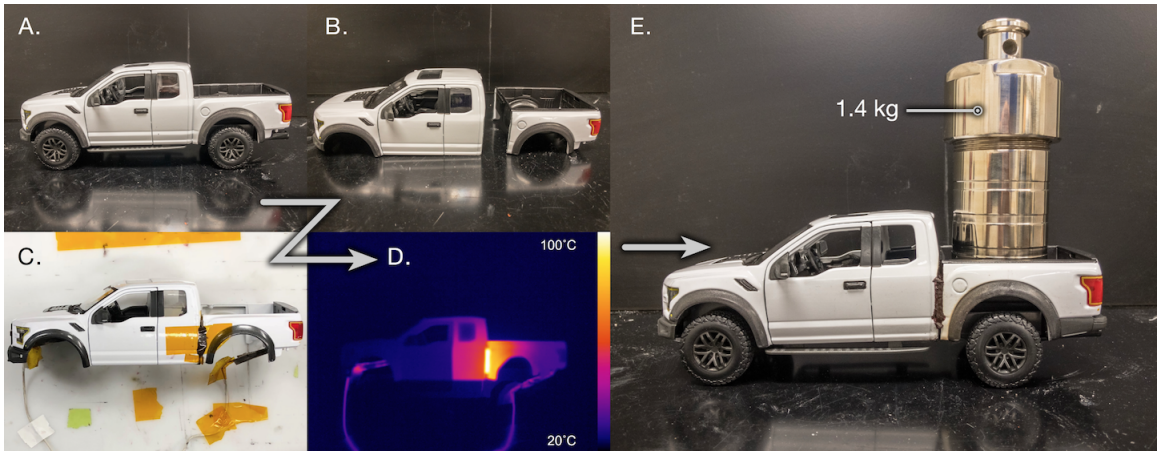

Figure 3.15: A model truck (A) was bisected by (B) cutting the truck bed off. (C) The truck and bed interface was filled with CNT loaded Betamate epoxy and connected to the RF source. (D) The interface containing the epoxy rapidly heated and the temperature was monitored with the FLIR camera. (E) The finished, welded truck was able to support weight (1.4 kg) in the truck bed.

We grounded the truck body and connected the truck bed to be bonded to the hot side of the RF source (Figure 3.15C). After a few minutes of heating (Figure 3.15D) the truck was fully bonded together to the green strength (Figure 3.16) and was able to support a 1.4 kg load in the truck bed (Figure 3.15E).

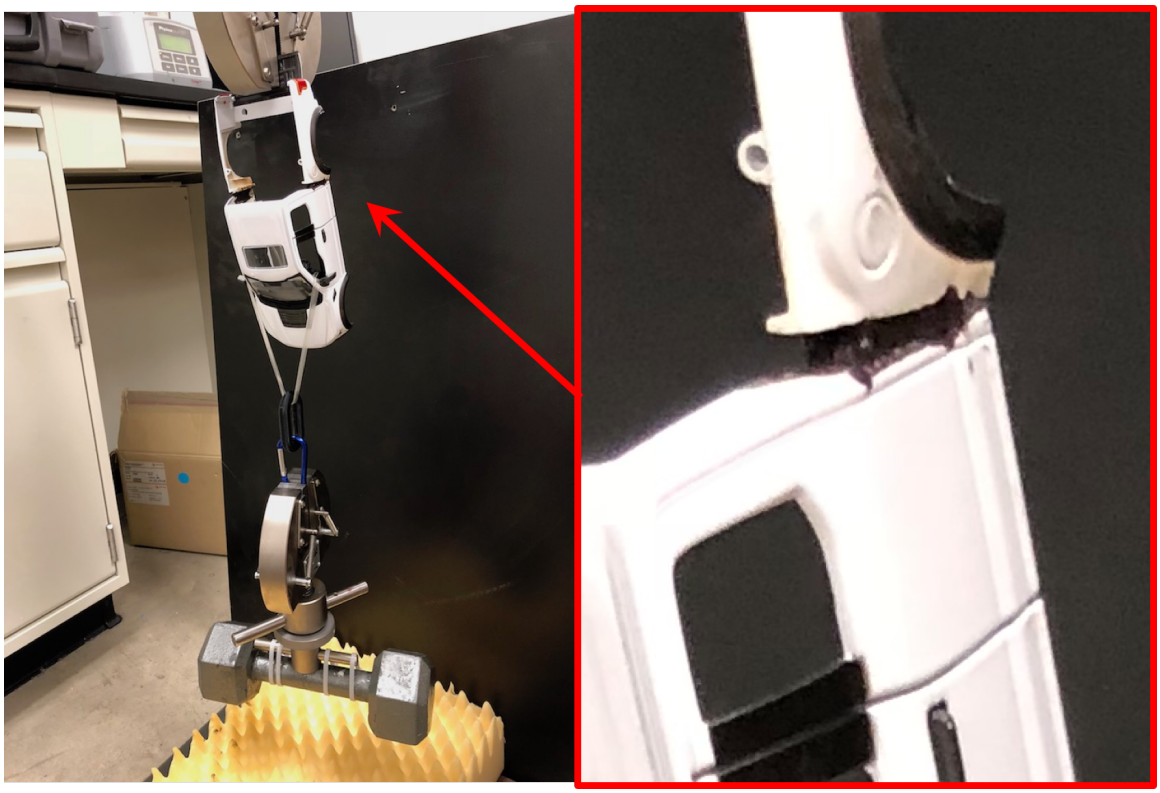

Figure 3.16: Cured truck halves being tested for green strength

It is clear from the FLIR images that heat emanates locally from the composite epoxy, this allowed the plastic components to be left on the model without melting them (this would not be possible with curing in an oven at 200°C). Such a technique may be applied on a full scale vehicle production line with robotic assembly equipment. Certain parts of the vehicle to be bonded could be connected to an RF power supply while the rest of the body is grounded. This would eliminate costly tooling, IR heaters, induction heaters, or ovens conventionally used to cure these epoxy bonds. Instead the components to be bonded are the electrodes and part of the circuit used to bond the heat-generating epoxy composite.

3.4 Conclusion

We highlight the advantages of RF heating and demonstrate for the first time the use of RF energy to heat polymer nanocomposites. By characterizing the dielectric properties of the material we are able to understand the mechanism for RF heating of the CNT composite materials used in this study. Various electric field applicator configurations including direct contact, parallel plate, and interdigitated fringing field applicators have been demonstrated by heating PLA/CNT composite films. We also have highlighted the practical use of this technique for bonding epoxy lap shear samples, and show that RF heating was able to achieve green strength two minutes faster than an oven-cured counterpart.

4. DIELECTRIC BARRIER DISCHARGE APPLICATOR FOR 3D PRINTING

4.1 Overview

Material Extrusion (ME) 3D printing is a revolutionary technique for manufacturing polymer parts; however, it has historically suffered from poor interlayer bonding, which is related to Z-strength. Many methods have been proposed to address the mechanical deficiencies of 3D printed parts, but most fall short of a production-ready solution. Here we report the use of a dielectric barrier discharge (DBD) plasma mounted concentrically around the nozzle of a 3D printer for *in-situ* welding of ME 3D printed parts. To our knowledge, this is the first report of a DBD plasma being used as a non-contact means to induce Joule heating in electrically-active composite materials. Our polymer welding process is accomplished by coupling the electromagnetic power from the DBD plasma into the interfaces of the 3D printed layers by adding a conformal layer of carbon nanotube polymer composite to the printer filament. The current passing through the part results in resistive heating of the layers and thermal welding of the interfaces. We show that parts printed with this method have isotropic strength, and are equivalent to their injection molded counterparts.

4.2 Introduction

Atmospheric dielectric barrier discharge (DBD) plasma was first discovered by Siemens in 1857 [122]. Originally used for the production of ozone, DBD plasmas have found many practical commercial uses, including water and air purification, surface treatments, aerodynamic flow control, lasers, lamps, and plasma displays [123, 124, 125]. A DBD consists of a high voltage potential applied to a conductive electrode separated by a solid dielectric layer and an air gap in between a ground electrode. The dielectric serves to limit current between the electrodes, suppressing hard arc discharges in favor of distributed filamentary

plasma or Townsend discharges. A unique feature of DBD plasmas is their ability to operate at atmospheric pressures in ambient air. The other defining feature of DBD plasmas is the low temperature of the plasma gas, which can be cool to the touch [126]. Much work has been devoted to developing DBD plasmas with low gas temperatures and current levels intentionally engineered to minimize electrical heating in the substrate. In this work, we seek to accomplish the opposite: we use an atmospheric non-thermal DBD plasma to heat a polymer nanocomposite.

To our knowledge, this is the first report of DBD plasma being used to intentionally heat an electrically active material. The DBD serves as a non-contact conductive electrode, which enables a high voltage kilohertz electric field to pass a current through a thermoplastic composite containing carbon nanotubes. The DBD plasma enables uniform heating of the grounded thermoplastic nanocomposite part without having to physically contact the material with the high voltage electrode. Furthermore, we extend this concept to 3D printing for the purpose of increasing the mechanical properties of printed parts by welding the interfaces of the extruded layers while the part is being printed.

We have previously shown that microwave energy can be used to weld the interfaces of 3D printed parts, increasing their interlayer strength significantly [7]. In that work, we embedded CNTs on the surface of 3D printer filament with an ink coating process. The coating remains at the interfaces of the 3D printed part, which allowed us to heat and weld the interfaces of the part with microwave energy. Microwaves, however, pose a challenge for uniformly heating materials with arbitrary shapes, and strict shielding requirements for safety limit the use to 3D printers with Faraday cage enclosures. Furthermore, microwave equipment, such as waveguides and horn antennas, are prohibitively large to mount on a 3D printer for *in-situ* welding. Higher microwave frequencies could be used to miniaturize the size of the components; however, the price of these components becomes prohibitive for commercial use.

In addition to microwaves, we have also shown that radio frequency (RF) electromagnetic energy may be used to heat polymer nanocomposites. RF electromagnetic heating has the benefits of lower shielding requirements both for safety and electromagnetic interference of the printer electronics. It may be operated in an electrically small capacitive applicator configuration to minimize far-field transmission, and the heating is localized to the vicinity of the hot electrode plane, making uniform controllable heating possible. Although direct-current (DC) has been used to heat nanocomposite materials, the electrodes must physically contact the surface of the part. In the context of ME 3D printing, we need a non-contact electrode to ensure the surface finish and mechanical integrity of the printed part is not compromised during the print.

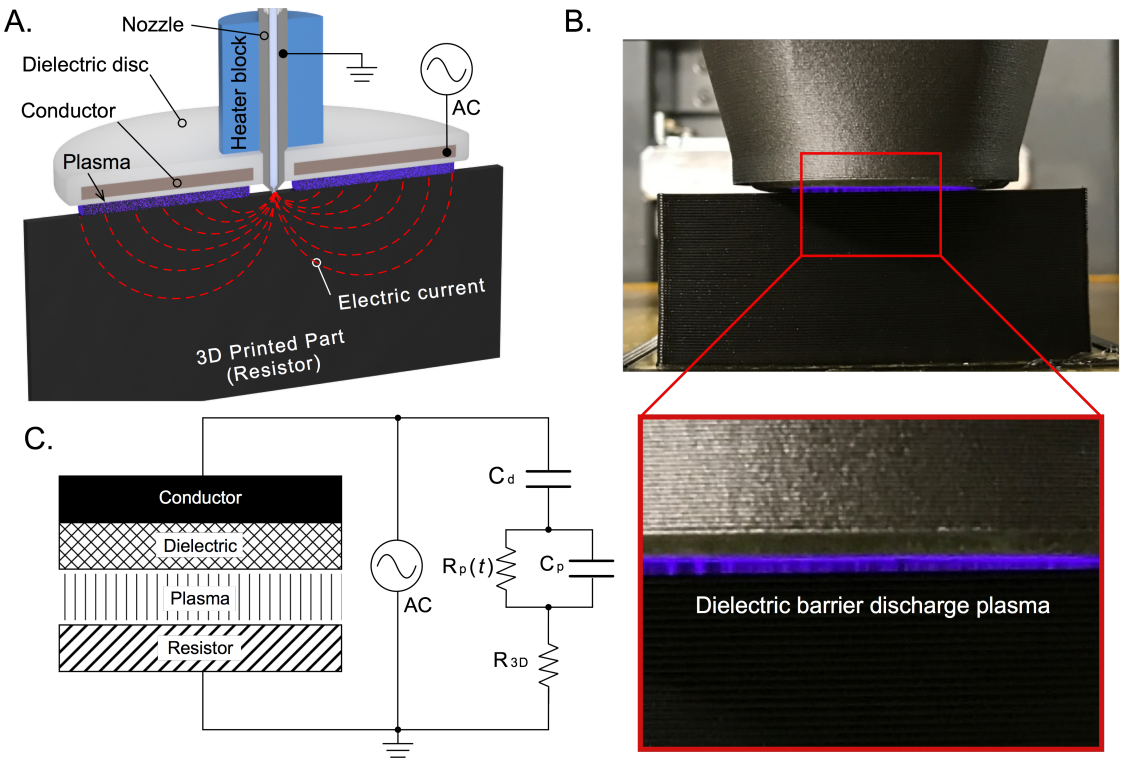

Figure 4.1: Illustration of the DBD nozzle applicator concept for a 3D printer (A). Image of the DBD plasma interacting with the 3D printed part (B). Equivalent circuit model for the system (C).

We have developed a novel concentric DBD plasma applicator disc positioned around the nozzle of a 3D printer (Figure 4.1A). The disc consists of a metallic electrode embedded in a dielectric disc with a hole in the center for the 3D printer nozzle. As a part is printed, a high voltage kilohertz RF signal excites a DBD plasma between the bottom of the disc and the 3D printed layer below it (Figure 4.1B). The nozzle serves as the ground electrode completing the circuit (Figure 4.1C) and the current pathway. In a large block of material, this fringing electric field produces a hemi-toroidal heating zone both ahead of and behind the deposited layer. Our process serves a three-fold purpose: plasma functionalization of the polymer surface to increase initial wetting of the polymer interfaces, preheating the layer ahead of the print to above the polymer glass transition temperature (Tg), and post-heating the deposited polymer bead to achieve time at temperature required for complete bonding. By performing these steps while the part is printed, we eliminate time-consuming post processing treatments; instead parts are ready for functional end-use applications right off the print bed. This is important for the commercial viability of this technology and its efficacy for use in a production environment.

4.3 Results and discussion

4.3.1 Heating mechanism

The mechanism for heating is best understood by analyzing an equivalent circuit model of the system. As shown in Figure 4.1C, an AC current source is connected in series to the high voltage plane in the applicator disc. The dielectric barrier layer used in the disc has a characteristic capacitance Cd associated with it given by the material properties of the dielectric, and the geometry of the disc. In between the disc and the 3D printed part is an air gap, typically between 0.5-2 mm where the plasma forms. In the simplest case, DBD plasmas may be modeled with an equivalent circuit consisting of a resistor Rp and capacitor Cp in parallel. In reality, the resistor is a transient element that is switching on

and off at a rate consistent with the driving frequency of the power source. The resistance of the plasma is based on the composition of the atmosphere and the power associated with the DBD. The resistance of the plasma results in some heating of the air, as well as light emissions from excited gaseous species. The DBD plasma couples directly to the 3D printed part, which is resistive (R_{3D}) based on the small amount of CNTs added to the thermoplastic feedstock filament.

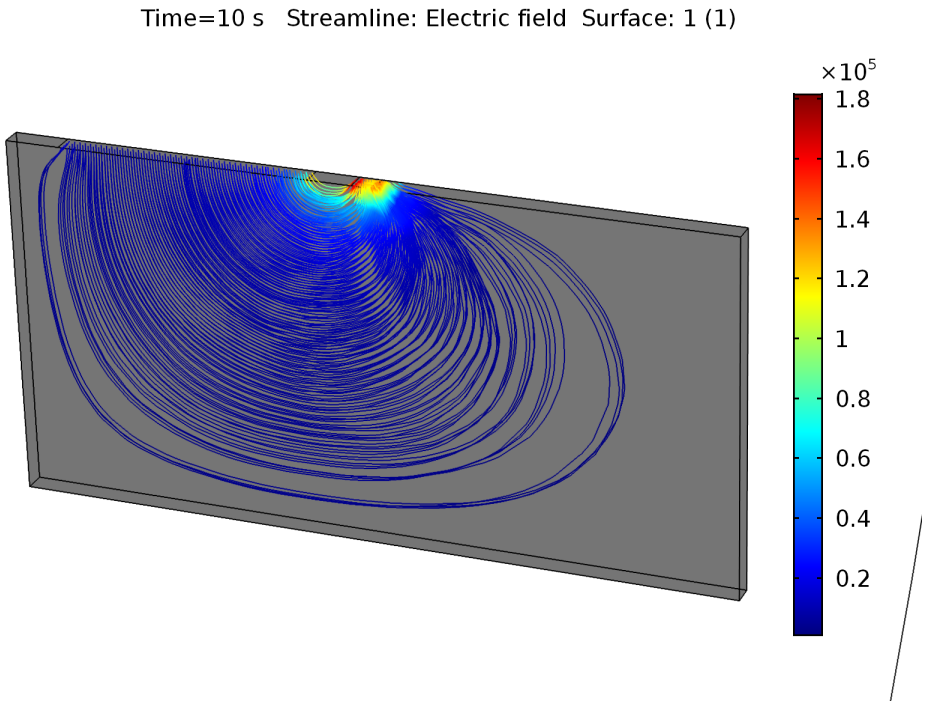

Figure 4.2: COMSOL simulation of the predicted electric field lines and current path back to the grounded nozzle in a 3D printed wall, similar to the tensile coupons printed for mechanical testing

To illustrate the exact electric field pattern and resultant stationary heat profile generated in the part, we modeled a 3D printed wall using a lumped sum approximation for the electrical properties of the material (scaling issues prevent the full simulation of the

electric field in the part since the CNT coating is on the order of microns while the part is several centimeters large). In Figure 4.2 it is clear that the predicted heating pattern is in line with the illustrations in Figure 4.1A.

The composition of the nanocomposite material is selected such that the electric current from the DBD plasma couples efficiently to the printed layers resulting in significant Joule heating. The current flowing through the 3D printed part flows to the nearest ground path, in this case the 3D printer nozzle which is electrically grounded to back to the AC current source. Based on this circuit configuration, our technology may be defined as an asymmetric resistive-dielectric barrier discharge [127].

4.3.2 Electrical characterization

To determine the power delivered by the DBD disc system, we used a high frequency oscilloscope along with a voltage probe connected the the high voltage line of the disc and a current probe connected to the ground return path from the part. Results of the measurements are shown in Figure 4.3.

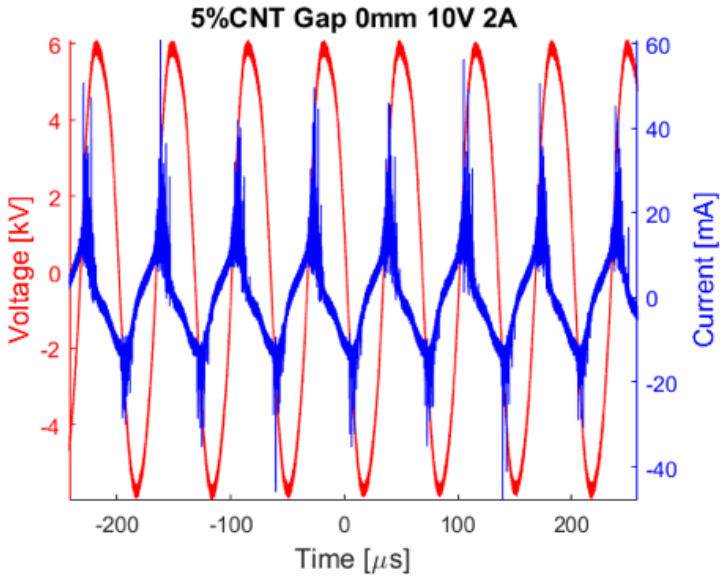

Figure 4.3: Voltage and current plots of the DBD disc coupled to a CNT nanocomposite film.

The voltage potential of the disc is approximately 12 kV peak to peak, with a frequency of approximately 15 kHz.

4.3.3 Plasma spectroscopic characterization

Spectral data of the DBD applicator was recorded both on a fixed plasma applicator and *in-situ* while a part was printed (Figure 4.4 and 4.5).

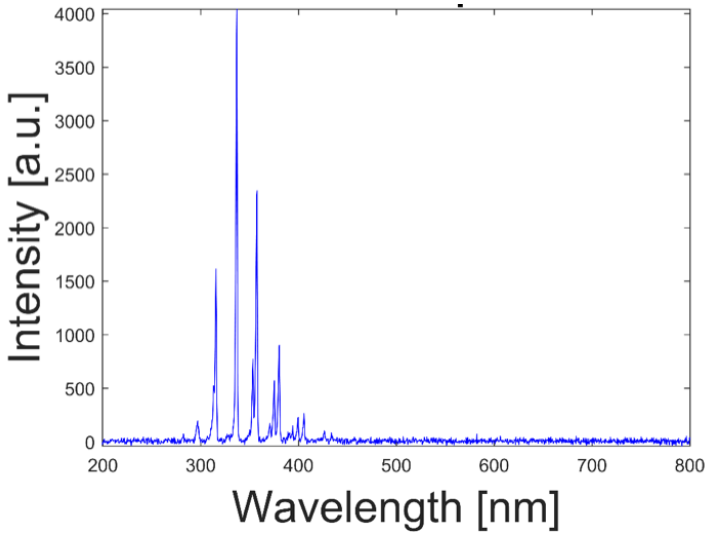

Figure 4.4: Spectra of the DBD plasma measured *in-situ* while a part was being printed

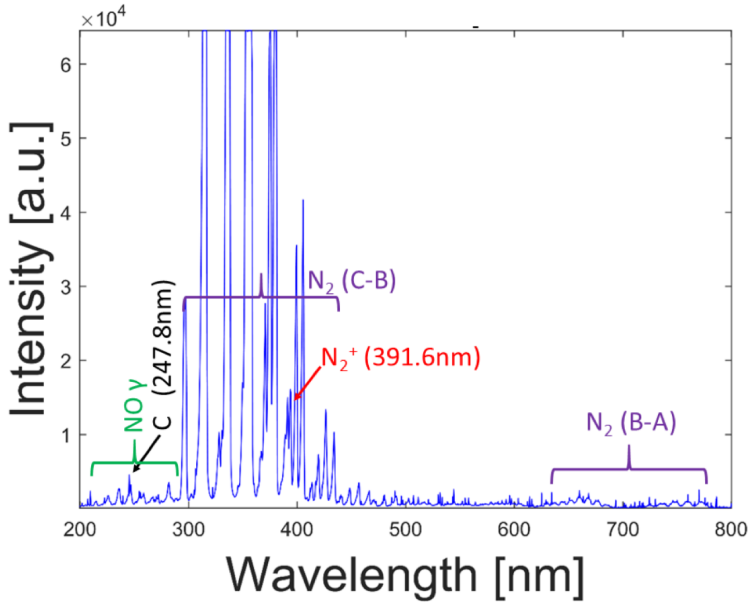

Figure 4.5: Spectra of the DBD plasma measured on a bench-top system. Each peak is assigned to a specific ionized gas species

The majority of the spectra is dominated by the 2nd positive system of N_2, which is common in air discharges. To determine the effective temperature of the plasma, we analyzed the spectroscopic data to approximate the rotational and vibrational temperatures of the gas species. From a thermodynamics perspective, the rotational temperature of the plasma is more closely related to the physical temperature of the plasma gas species near the 3D printed layer.

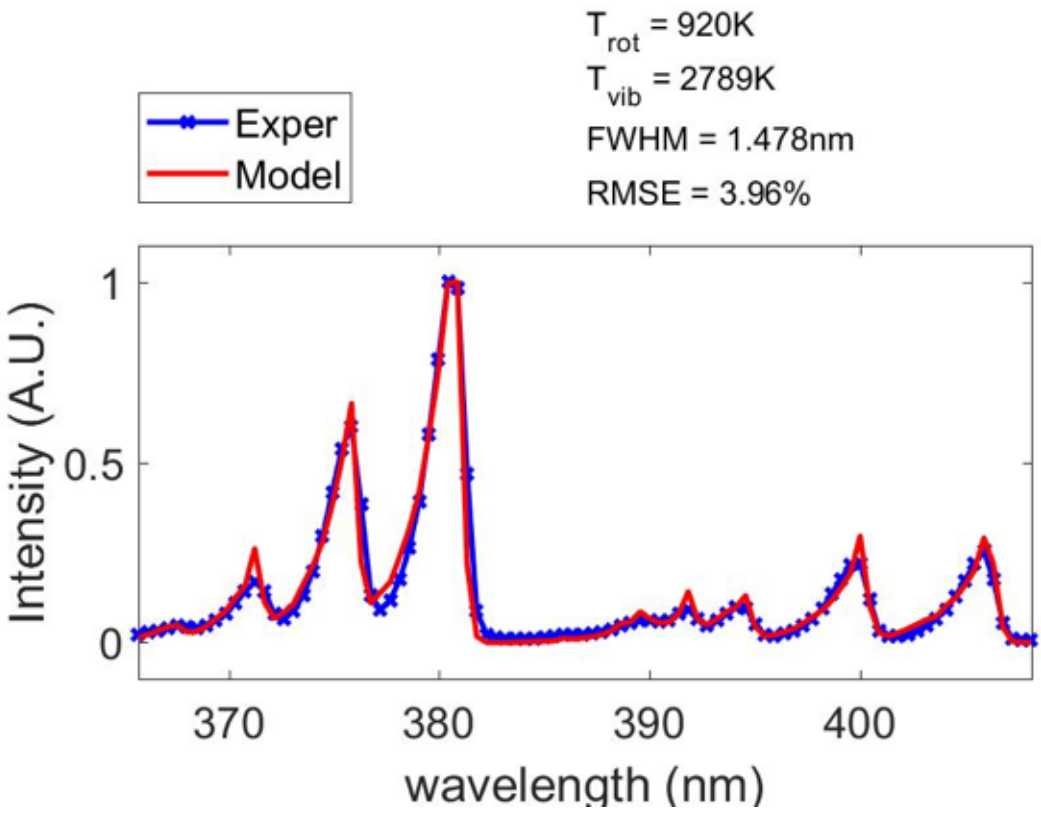

Figure 4.6: Temperature of the DBD plasma measured on a bench-top system. A curve fitting program was used to estimate the plasma rotational and vibrational temperatures

A spectrum is shown in Figure 4.6 with a simulated N_2 2nd positive system with N_2+.

The best match for temperature from a curve-fitting program indicates that the rotational temperature of the discharge is Trot=920 K, and the vibrational temperature is T_{vib}=2789 K.

4.3.4 Plasma surface functionalization

In addition to the heating effect of the electrical current on the part, we investigated the effect of the plasma on the surface chemistry of the 3D printed layers. It is well known that DBD plasmas may be used to modify and functionalize the surface of various materials including polymers [128, 129]. Plasma functionalization has been directly correlated to an increase in adhesion strength for epoxy-bonded lap shear joints [130]. Narahara et al. reported the use of an atmospheric pressure helium plasma plume for treating the layers of 3D printed parts [26]. Although they noticed an increase in surface free energy of the PLA printed layers, it only resulted in modest improvements in interlayer strength. We propose that the plasma treatment may aid in promoting the initial step of the polymer welding process: wetting. We performed X-ray Photoelectron Spectroscopy (XPS) on 3D printed polyamide samples to investigate the effects of the DBD plasma on the polymer and resolve the change in surface chemistry associated with wettability of the polymer interface.

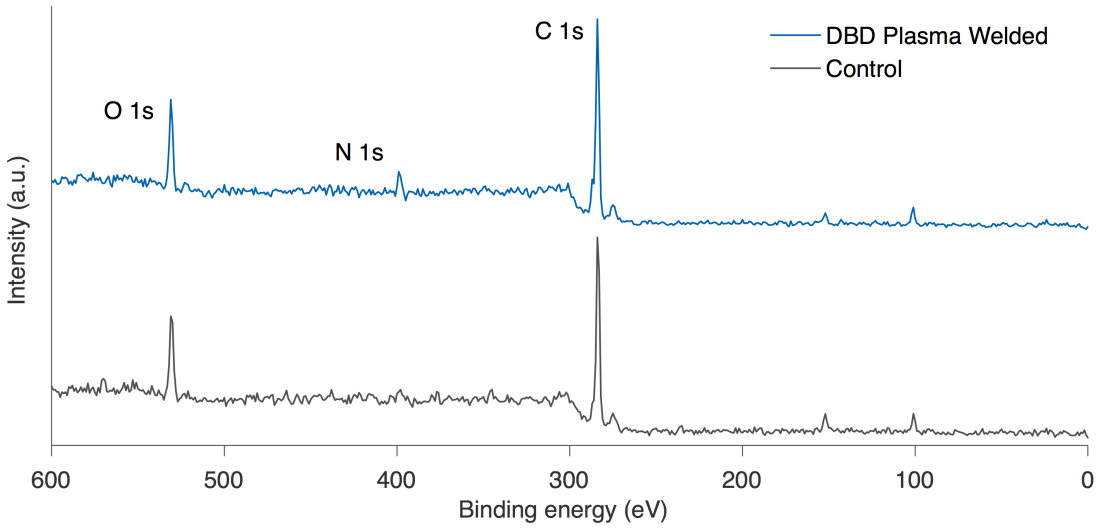

Figure 4.7: XPS data: intensity vs. binding energy for control 3D printed polyamide samples, and samples with the *in-situ* DBD plasma treatment

The carbon (C1s), nitrogen (N1s), and oxygen (O1s) peaks are indicated on the graph in Figure 4.7. Notably, the nitrogen peak for the plasma treated sample is more pronounced compared to the control sample. The peaks were resolved for percent atomic composition of the various functional groups on the surface. It was found that before and after the plasma treatment the carbon peak decreased from 88.2% down to 81.6%, the oxygen peak increased from 11.8% up to 12.7%, and the nitrogen peak increased from null to 5.7%. This indicates that the surface chemistry of the polyamide changes quite dramatically with an increase in functional groups associated with high surface energy and favorable wettability of the surface as the next polymer layer is extruded on top of it.

Although the data suggests that conditions for polymer bonding will be more favorable in the presence of the DBD plasma, it is unlikely that surface chemistry alone can account for the isotropic strength properties seen in our samples. A full polymer weld requires entanglement of the polymer chains across the weld interface. Thus, in addition to the

initial wetting of the polymer interfaces, polymer mobility initiated by thermal energy is required for a sufficient amount of time to reach full bond-line strength.

4.3.5 Joule heating and welding of the interfaces

We propose that the thermal effects from the DBD Joule heating dominate the interfacial welding kinetics, and in turn the dramatic improvements we see in the interlayer strength. To characterize these thermal effects, we employ the use of *in-situ* thermography measurements (Figure 4.8A) of the mechanical test coupons [131].

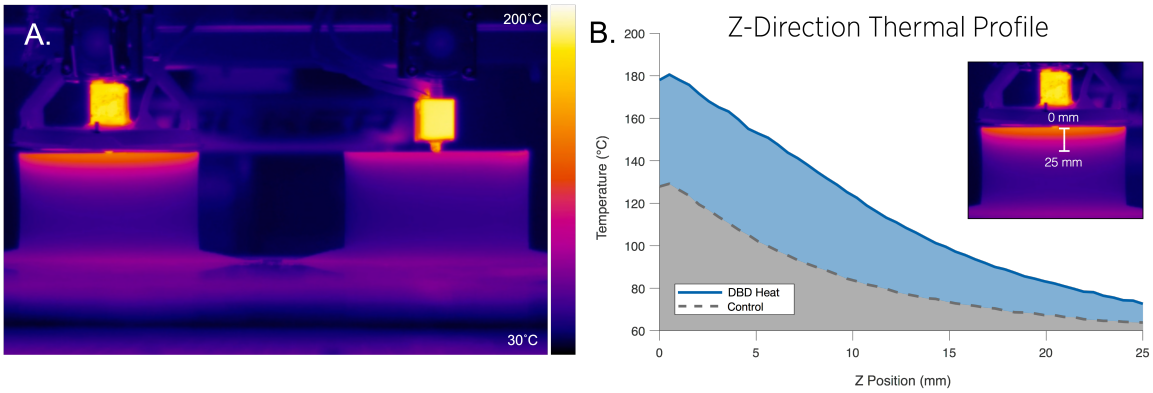

Figure 4.8: FLIR infrared thermal image of 3D printed test coupons printed side-by-side, the left coupon has the DBD plasma system while the right is the control sample (A) and temperature vs. depth plot of each coupon in Figure 4.8A with and without DBD plasma heat, temperature is plotted for the top 25 mm of each sample

To simplify the thermal analysis of the DBD applicator, we approximate its effect on the printed layers as a one-dimensional heat source (Q_{DBD}) with a given penetration depth governed by the power output of the plasma and a residence time based on the print speed and dimensions of the disc.

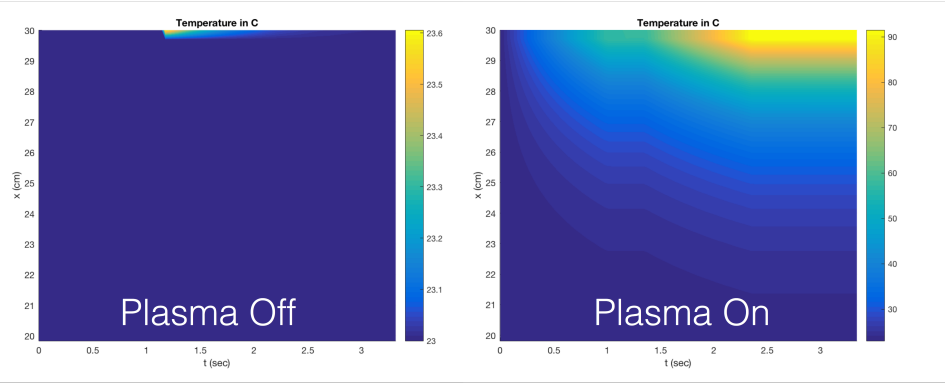

Figure 4.9: Simple 1D heat transfer model plotted in MATLAB for the residual nozzle heat alone (left) and with a simulated plasma disc heat source (right)

In order to compare our physical measurements to the predicted heating of the DBD system, we created a MATLAB script where various disc geometries, power levels, and print speeds (residence times) could be evaluated. The results of an 80 mm disc (two 30 mm line sources separated by the central gap for the nozzle) and 1 mm nozzle diameter are shown in Figure 4.9. The Y axis corresponds to the Z height of a printed coupon, and the X axis corresponds to a one-dimensional temporal fixed frame of reference extruded plot, or alternatively in a moving frame of reference: the width of the printed part. This model does not account for the thermal mass of a polymer trace deposited. Future models may include this heat source for better accuracy.

4.3.6 Thermal analysis of mechanical samples

For the mechanical test coupons used to test tensile strength, we also measured the thermal profile and compare that to a control sample printed at the same time (the Stacker printer has 4 available print heads for simultaneous printing). The results of these measurements are shown in Figure 4.8B, where we plot a 25 mm line temperature profile of the sample starting at the top of the sample near the newly printed layer. This thermal profile is a good measure of the time at temperature history of the part which governs the

polymer interdiffusion across the printed layers [97]. In comparison to the control coupon printed with identical settings, the DBD heated part has a surface temperature 50°C hotter at 180°C, which is above the Tg of the PA (160°C). This demonstrates the success of our method at accomplishing the preheating of the polymer layer to above the Tg prior to the deposition of the next layer. Not only is the surface temperature increased, we see that the depth of heating is significant compared to the control sample. The DBD heated part has the same temperature of the surface of the control sample nearly 10 mm deep into the part. This demonstrates a vast increase of the time above the critical temperature required to form a complete bond between successive layers. It is generally accepted that the bond strength between thermally welded layers follows an Arrhenius relationship governed by the activation energy of the polymer and is correlated to the inverse fourth power of time.

$$\phi(T,t) = K_0\, exp\Big(-\frac{E_a}{RT}\Big)t^{\frac{1}{4}}$$

where ϕ is the degree of the bond as a function of time, K_0 is the proportionality factor, E_a is the activation energy, R is the gas constant, T is the temperature, and t is the weld time. We have succeeded in increasing both the weld temperature and weld time without overheating the part such that the dimensional tolerances or surface finish were compromised. This correlates directly to an increase in mechanical properties.

4.3.7 Mechanical properties

To assess mechanical enhancement, mechanical test coupons with a thickness of 3.5 mm were printed both with and without the application of DBD welding. ASTM D638 tensile dogbones were routed out of the test coupons with a CNC mill to ensure geometric consistency between all samples. In addition to 3D printed control samples, we prepared injection molded dogbone samples with the same polymer used to produce the thermoplastic filament feedstock.

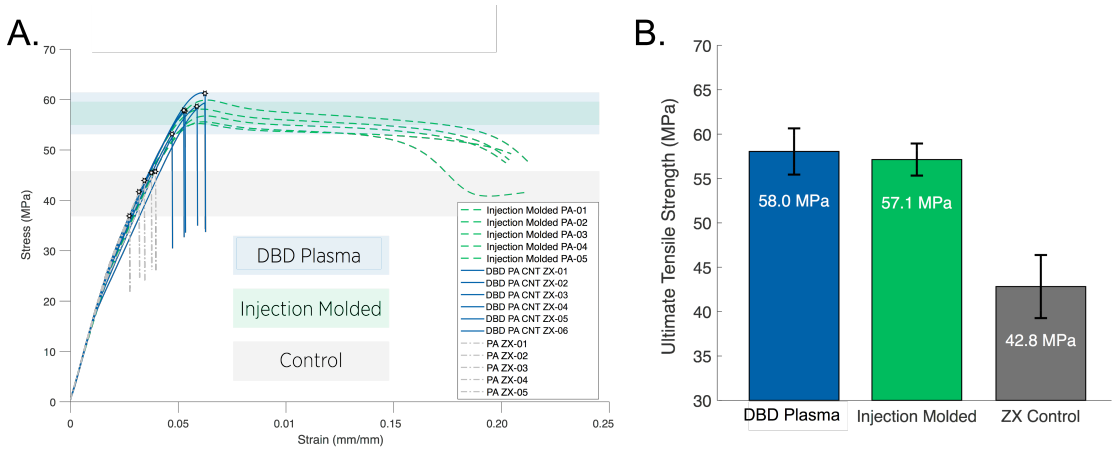

Figure 4.10: Tensile stress-strain plots for the dogbones tested with and without DBD heating as well as a comparison to injection molded samples

Results of the tensile tests are shown in Figure 4.10A; the DBD-welded samples exhibit tensile strength values statistically equivalent to the injection molded samples and 35% higher than the 3D printed control samples (Figure 4.10B). To our knowledge, this is the first report of isotropic tensile strength values for ME 3D printed parts that do not employ post-processing or adhesive bonding techniques.

4.4 Conclusion

In conclusion, we have successfully demonstrated the use of DBD plasma as a non-contact electromagnetic heating source for nanocomposite materials. We have applied this concept to an *in-situ* disc attachment for a 3D printer nozzle to heat and plasma treat the layers of a 3D printed part while it is being built. The results are exceptional, with the Z-strength matching that of injection molded counterparts. This DBD welding process is a promising method for enabling material extrusion 3D printed components to be strong enough for both functional prototypes and production-ready end-use parts.

5. SUMMARY

In this dissertation, we sought to describe the interaction between electromagnetic energy and functional nanocomposites and apply these phenomena to polymer processing. We used microwave energy to target and heat CNT-rich interfaces of 3D printed parts. After the microwave heat treatment, 3D printed PLA samples were shown to improve the weld fracture strength by 275%. This work was expanded upon with the use of an *in-situ* electric field applicator mounted on a 3D printer nozzle. By heat treating the parts during the printing process, tensile samples showed strength values equal to their injection molded counterparts. Additionally, we showed that industrial adhesives can be heated with radio frequency electromagnetic fields when carbon nanotubes are incorporated into the adhesive. Samples cured with the RF field reached green strength in three minutes as opposed to five minutes for oven-cured control samples. These applications show the promise of coupling electromagnetic energy to nanocomposites for industrial manufacturing applications.

REFERENCES

[1] R. J. Young and P. A. Lovell, *Introduction to polymers*. CRC press, 2011.

[2] T. Zehev and C. G. Gogos, *Principles of polymer processing*. John Wiley & Sons, NY, 1979.

[3] B. N. Turner, R. Strong, and S. A. Gold, "A review of melt extrusion additive manufacturing processes: I. process design and modeling," *Rapid Prototyping Journal*, vol. 20, no. 3, pp. 192–204, 2014.

[4] B. N. Turner and S. A. Gold, "A review of melt extrusion additive manufacturing processes: Ii. materials, dimensional accuracy, and surface roughness," *Rapid Prototyping Journal*, vol. 21, no. 3, pp. 250–261, 2015.

[5] K. V. Wong and A. Hernandez, "A review of additive manufacturing," *ISRN Mechanical Engineering*, vol. 2012, pp. 1–10, 2012.

[6] J. R. Tumbleston, D. Shirvanyants, N. Ermoshkin, R. Janusziewicz, A. R. Johnson, D. Kelly, K. Chen, R. Pinschmidt, J. P. Rolland, A. Ermoshkin, *et al.*, "Continuous liquid interface production of 3d objects," *Science*, vol. 347, no. 6228, pp. 1349–1352, 2015.

[7] C. B. Sweeney, B. A. Lackey, M. J. Pospisil, T. C. Achee, V. K. Hicks, A. G. Moran, B. R. Teipel, M. A. Saed, and M. J. Green, "Welding of 3d-printed carbon nanotube–polymer composites by locally induced microwave heating," *Science Advances*, vol. 3, no. 6, p. e1700262, 2017.

[8] Y. H. Kim and R. P. Wool, "A theory of healing at a polymer-polymer interface," *Macromolecules*, vol. 16, no. 7, pp. 1115–1120, 1983.

[9] P. G. de Gennes, "Reptation of a polymer chain in the presence of fixed obstacles," *The Journal of Chemical Physics*, vol. 55, no. 2, pp. 572–579, 1971.

[10] L. Li, Q. Sun, C. Bellehumeur, and P. Gu, "Investigation of bond formation in fdm process," *Solid Freeform Fabrication Proceedings,(403)*, vol. 400407, 2002.

[11] J. E. Seppala, S. H. Han, K. E. Hillgartner, C. S. Davis, and K. B. Migler, "Weld formation during material extrusion additive manufacturing," *Soft Matter*, vol. 13, no. 38, pp. 6761–6769, 2017.

[12] J. F. Rodríguez, J. P. Thomas, and J. E. Renaud, "Mechanical behavior of acrylonitrile butadiene styrene (abs) fused deposition materials. experimental investigation," *Rapid Prototyping Journal*, vol. 7, no. 3, pp. 148–158, 2001.

[13] C. S. Davis, K. E. Hillgartner, S. H. Han, and J. E. Seppala, "Mechanical strength of welding zones produced by polymer extrusion additive manufacturing," *Additive Manufacturing*, vol. 16, pp. 162–166, 2017.

[14] Y. Song, Y. Li, W. Song, K. Yee, K.-Y. Lee, and V. Tagarielli, "Measurements of the mechanical response of unidirectional 3d-printed pla," *Materials & Design*, vol. 123, no. Supplement C, pp. 154 – 164, 2017.

[15] N. Aliheidari, R. Tripuraneni, A. Ameli, and S. Nadimpalli, "Fracture resistance measurement of fused deposition modeling 3d printed polymers," *Polymer Testing*, vol. 60, pp. 94–101, 2017.

[16] M. S. Hossain, J. Ramos, D. Espalin, M. Perez, and R. Wicker, "Improving tensile mechanical properties of fdm-manufactured specimens via modifying build parameters," in *International Solid Freeform Fabrication Symposium: An Additive Manufacturing Conference. Austin, TX*, vol. 2013, pp. 380–392, 2013.

[17] J. Chacón, M. Caminero, E. García-Plaza, and P. Núñez, "Additive manufacturing of pla structures using fused deposition modelling: Effect of process parameters on mechanical properties and their optimal selection," *Materials & Design*, vol. 124, pp. 143–157, 2017.

[18] E. Ulu, E. Korkmaz, K. Yay, O. B. Ozdoganlar, and L. B. Kara, "Enhancing the structural performance of additively manufactured objects through build orientation optimization," *Journal of Mechanical Design*, vol. 137, no. 11, p. 111410, 2015.

[19] A. Qattawi, B. Alrawi, A. Guzman, *et al.*, "Experimental optimization of fused deposition modelling processing parameters: a design-for-manufacturing approach," *Procedia Manufacturing*, vol. 10, pp. 791–803, 2017.

[20] G. C. Onwubolu and F. Rayegani, "Characterization and optimization of mechanical properties of abs parts manufactured by the fused deposition modelling process," *International Journal of Manufacturing Engineering*, vol. 2014, 2014.

[21] S. C. Partain *et al.*, *Fused deposition modeling with localized pre-deposition heating using forced air*. PhD thesis, Montana State University-Bozeman, College of Engineering, 2007.

[22] A. K. Ravi, A. Deshpande, and K. H. Hsu, "An in-process laser localized pre-deposition heating approach to inter-layer bond strengthening in extrusion based polymer additive manufacturing," *Journal of Manufacturing Processes*, vol. 24, pp. 179–185, 2016.

[23] V. Kishore, C. Ajinjeru, A. Nycz, B. Post, J. Lindahl, V. Kunc, and C. Duty, "Infrared preheating to improve interlayer strength of big area additive manufacturing (baam) components," *Additive Manufacturing*, vol. 14, pp. 7–12, 2017.

[24] C. E. Duty, C. E. Duty, V. Kunc, V. Kunc, B. Compton, B. Compton, B. Post, B. Post, D. Erdman, D. Erdman, *et al.*, "Structure and mechanical behavior of big area additive manufacturing (baam) materials," *Rapid Prototyping Journal*, vol. 23, no. 1, pp. 181–189, 2017.

[25] J. T. Belter and A. M. Dollar, "Strengthening of 3d printed fused deposition manufactured parts using the fill compositing technique," *PloS one*, vol. 10, no. 4, p. e0122915, 2015.

[26] H. Narahara, Y. Shirahama, and H. Koresawa, "Improvement and evaluation of the interlaminar bonding strength of fdm parts by atmospheric-pressure plasma," *Procedia CIRP*, vol. 42, pp. 754–759, 2016.

[27] M. Noeske, J. Degenhardt, S. Strudthoff, and U. Lommatzsch, "Plasma jet treatment of five polymers at atmospheric pressure: surface modifications and the relevance for adhesion," *International Journal of Adhesion and Adhesives*, vol. 24, no. 2, pp. 171–177, 2004.

[28] J. Mikulak, C. Deckard, and R. Zinniel, "Core-shell consumable materials for use in extrusion-based additive manufacturing systems," Sept. 13 2012. US Patent App. 13/419,669.

[29] P. Toal, L. Holmes, R. Rodriguez, and E. Wetzel, "Microstructured monofilament via thermal drawing of additively manufactured preforms," *Additive Manufacturing*, vol. 16, pp. 12–23, 2017.

[30] R. Brennan, C. Moorehead, V. Blair, and K. Limmer, "Energy coupled to matter for magnetic alignment of rare earth–doped alumina," *Materials and Manufacturing Processes*, pp. 1–6, 2016.

[31] P. Pötschke, S. M. Dudkin, and I. Alig, "Dielectric spectroscopy on melt processed polycarbonatemultiwalled carbon nanotube composites," *Polymer*, vol. 44, no. 17, pp. 5023–5030, 2003.

[32] M. Mehdizadeh, *Microwave/RF applicators and probes: for material heating, sensing, and plasma generation*. William Andrew, 2015.

[33] A. Collins, *Nanotechnology cookbook: practical, reliable and jargon-free experimental procedures*. Elsevier, 2012.

[34] Y. Xia, Y. Xiong, B. Lim, and S. E. Skrabalak, "Shape-controlled synthesis of metal nanocrystals: Simple chemistry meets complex physics?," *Angewandte Chemie International Edition*, vol. 48, no. 1, pp. 60–103, 2009.

[35] E. Yasun, H. Kang, H. Erdal, S. Cansiz, I. Ocsoy, Y.-F. Huang, and W. Tan, "Cancer cell sensing and therapy using affinity tag-conjugated gold nanorods," *Interface Focus*, vol. 3, no. 3, p. 20130006, 2013.

[36] K. L. Kelly, E. Coronado, L. L. Zhao, and G. C. Schatz, "The optical properties of metal nanoparticles: the influence of size, shape, and dielectric environment," 2003.

[37] S. Link and M. A. El-Sayed, "Shape and size dependence of radiative, non-radiative and photothermal properties of gold nanocrystals," *International Reviews in Physical Chemistry*, vol. 19, no. 3, pp. 409–453, 2000.

[38] J. Chen, D. Wang, J. Xi, L. Au, A. Siekkinen, A. Warsen, Z.-Y. Li, H. Zhang, Y. Xia, and X. Li, "Immuno gold nanocages with tailored optical properties for targeted photothermal destruction of cancer cells," *Nano Letters*, vol. 7, no. 5, pp. 1318–1322, 2007.

[39] Z. Zhu, E. Senses, P. Akcora, and S. A. Sukhishvili, "Programmable light-controlled shape changes in layered polymer nanocomposites," *ACS Nano*, vol. 6, no. 4,

pp. 3152–3162, 2012.

[40] J. P. Kottmann, O. J. Martin, D. R. Smith, and S. Schultz, "Plasmon resonances of silver nanowires with a nonregular cross section," *Physical Review B*, vol. 64, no. 23, p. 235402, 2001.

[41] S. Oldenburg, R. Averitt, S. Westcott, and N. Halas, "Nanoengineering of optical resonances," *Chemical Physics Letters*, vol. 288, no. 2, pp. 243–247, 1998.

[42] N. J. Hogan, A. S. Urban, C. Ayala-Orozco, A. Pimpinelli, P. Nordlander, and N. J. Halas, "Nanoparticles heat through light localization," *Nano Letters*, vol. 14, no. 8, pp. 4640–4645, 2014.

[43] S. Link, C. Burda, M. Mohamed, B. Nikoobakht, and M. A. El-Sayed, "Laser photothermal melting and fragmentation of gold nanorods: energy and laser pulse-width dependence," *The Journal of Physical Chemistry A*, vol. 103, no. 9, pp. 1165–1170, 1999.

[44] S. Link, C. Burda, M. Mohamed, B. Nikoobakht, and M. El-Sayed, "Femtosecond transient-absorption dynamics of colloidal gold nanorods: Shape independence of the electron-phonon relaxation time," *Physical Review B*, vol. 61, no. 9, p. 6086, 2000.

[45] A. O. Govorov and H. H. Richardson, "Generating heat with metal nanoparticles," *Nano Today*, vol. 2, no. 1, pp. 30–38, 2007.

[46] A. O. Govorov, W. Zhang, T. Skeini, H. Richardson, J. Lee, and N. A. Kotov, "Gold nanoparticle ensembles as heaters and actuators: melting and collective plasmon resonances," *Nanoscale Research Letters*, vol. 1, no. 1, p. 84, 2006.

[47] X. Huang, I. H. El-Sayed, W. Qian, and M. A. El-Sayed, "Cancer cell imaging and photothermal therapy in the near-infrared region by using gold nanorods," *Journal*

of the American Chemical Society, vol. 128, no. 6, pp. 2115–2120, 2006.

[48] E. Boisselier and D. Astruc, "Gold nanoparticles in nanomedicine: preparations, imaging, diagnostics, therapies and toxicity," *Chemical Society Reviews*, vol. 38, no. 6, pp. 1759–1782, 2009.

[49] D. Boyer, P. Tamarat, A. Maali, B. Lounis, and M. Orrit, "Photothermal imaging of nanometer-sized metal particles among scatterers," *Science*, vol. 297, no. 5584, pp. 1160–1163, 2002.

[50] P. K. Jain, X. Huang, I. H. El-Sayed, and M. A. El-Sayed, "Noble metals on the nanoscale: optical and photothermal properties and some applications in imaging, sensing, biology, and medicine," *Accounts of Chemical Research*, vol. 41, no. 12, pp. 1578–1586, 2008.

[51] P. Matteini, F. Ratto, F. Rossi, S. Centi, L. Dei, and R. Pini, "Chitosan films doped with gold nanorods as laser-activatable hybrid bioadhesives," *Advanced Materials*, vol. 22, no. 38, pp. 4313–4316, 2010.

[52] P. Matteini, F. Ratto, F. Rossi, and R. Pini, "Emerging concepts of laser-activated nanoparticles for tissue bonding," *Journal of Biomedical Optics*, vol. 17, no. 1, pp. 0107011–0107019, 2012.

[53] P. Matteini, F. Ratto, F. Rossi, M. de Angelis, L. Cavigli, and R. Pini, "Hybrid nanocomposite films for laser-activated tissue bonding," *Journal of Biophotonics*, vol. 5, no. 11-12, pp. 868–877, 2012.

[54] S. R. Sershen, G. A. Mensing, M. Ng, N. J. Halas, D. J. Beebe, and J. L. West, "Independent optical control of microfluidic valves formed from optomechanically responsive nanocomposite hydrogels," *Advanced Materials*, vol. 17, no. 11, pp. 1366–1368, 2005.

[55] S. Maity, K. A. Kozek, W.-C. Wu, J. B. Tracy, J. R. Bochinski, and L. I. Clarke, "Anisotropic thermal processing of polymer nanocomposites via the photothermal effect of gold nanorods," *Particle & Particle Systems Characterization*, vol. 30, no. 2, pp. 193–202, 2013.

[56] S. Maity, W.-C. Wu, C. Xu, J. B. Tracy, K. Gundogdu, J. R. Bochinski, and L. I. Clarke, "Spatial temperature mapping within polymer nanocomposites undergoing ultrafast photothermal heating via gold nanorods," *Nanoscale*, vol. 6, no. 24, pp. 15236–15247, 2014.

[57] V. Viswanath, S. Maity, J. R. Bochinski, L. I. Clarke, and R. E. Gorga, "Thermal annealing of polymer nanocomposites via photothermal heating: effects on crystallinity and spherulite morphology," *Macromolecules*, vol. 46, no. 21, pp. 8596–8607, 2013.

[58] H. Zhang, D. Fortin, H. Xia, and Y. Zhao, "Fast optical healing of crystalline polymers enabled by gold nanoparticles," *Macromolecular Rapid Communications*, vol. 34, no. 22, pp. 1742–1746, 2013.

[59] B. Nearingburg and A. Elias, "Characterization of surface plasmon energy transduction in gold nanoparticle/polymer composites by photo-dsc," *Thermochimica Acta*, vol. 512, no. 1, pp. 247–253, 2011.

[60] H. Zhang, D. Han, Q. Yan, D. Fortin, H. Xia, and Y. Zhao, "Light-healable hard hydrogels through photothermally induced melting–crystallization phase transition," *Journal of Materials Chemistry A*, vol. 2, no. 33, pp. 13373–13379, 2014.

[61] Z. Cao, R. Wang, L. Hao, W. Jiao, F. Yang, Q. Wang, W. Liu, B. Zhang, X. Lu, and X. He, "Interfacial healing of carbon fiber composites in the presence of gold nanoparticles as localized nano-heaters," *RSC Advances*, vol. 5, no. 8, pp. 5680–5685, 2015.

[62] S. Maity, L. N. Downen, J. R. Bochinski, and L. I. Clarke, "Embedded metal nanoparticles as localized heat sources: An alternative processing approach for complex polymeric materials," *Polymer*, vol. 52, no. 7, pp. 1674–1685, 2011.

[63] S. Maity, J. R. Bochinski, and L. I. Clarke, "Metal nanoparticles acting as light-activated heating elements within composite materials," *Advanced Functional Materials*, vol. 22, no. 24, pp. 5259–5270, 2012.

[64] H. Zhang and Y. Zhao, "Polymers with dual light-triggered functions of shape memory and healing using gold nanoparticles," *ACS Applied Materials & Interfaces*, vol. 5, no. 24, pp. 13069–13075, 2013.

[65] O. Ivanova, C. Williams, and T. Campbell, "Additive manufacturing (AM) and nanotechnology: promises and challenges," *Rapid Prototyping Journal*, vol. 19, no. 5, pp. 353–364, 2013.

[66] Q. Sun, G. Rizvi, C. Bellehumeur, and P. Gu, "Experimental study of the cooling characteristics of polymer filaments in fdm and impact on the mesostructures and properties of prototypes," *Proceedings of the Solid Freeform Fabrication Proceedings, Austin, TX, USA*, pp. 4–6, 2003.

[67] C. Bellehumeur, L. Li, Q. Sun, and P. Gu, "Modeling of bond formation between polymer filaments in the fused deposition modeling process," *Journal of Manufacturing Processes*, vol. 6, no. 2, pp. 170–178, 2004.

[68] Q. Sun, G. Rizvi, C. Bellehumeur, and P. Gu, "Effect of processing conditions on the bonding quality of fdm polymer filaments," *Rapid Prototyping Journal*, vol. 14, no. 2, pp. 72–80, 2008.

[69] E. Vazquez and M. Prato, "Carbon nanotubes and microwaves: interactions, responses, and applications," *Acs Nano*, vol. 3, no. 12, pp. 3819–3824, 2009.

[70] R. H. Baughman, A. A. Zakhidov, and W. A. De Heer, "Carbon nanotubes–the route toward applications," *Science*, vol. 297, no. 5582, pp. 787–792, 2002.

[71] V. K. Rangari, M. S. Bhuyan, and S. Jeelani, "Microwave processing and characterization of epon 862/cnt nanocomposites," *Materials Science and Engineering: B*, vol. 168, no. 1, pp. 117–121, 2010.

[72] F. G. Brunetti, M. A. Herrero, J. d. M. Munoz, A. Diaz-Ortiz, J. Alfonsi, M. Meneghetti, M. Prato, and E. Vázquez, "Microwave-induced multiple functionalization of carbon nanotubes," *Journal of the American Chemical Society*, vol. 130, no. 25, pp. 8094–8100, 2008.

[73] T. Imholt, C. A. Dyke, B. Hasslacher, J. M. Pérez, D. Price, J. A. Roberts, J. Scott, A. Wadhawan, Z. Ye, and J. M. Tour, "Nanotubes in microwave fields: light emission, intense heat, outgassing, and reconstruction," *Chemistry of Materials*, vol. 15, no. 21, pp. 3969–3970, 2003.

[74] A. Mashal, B. Sitharaman, X. Li, P. K. Avti, A. V. Sahakian, J. H. Booske, and S. C. Hagness, "Toward carbon-nanotube-based theranostic agents for microwave detection and treatment of breast cancer: Enhanced dielectric and heating response of tissue-mimicking materials," *IEEE Transactions on Biomedical Engineering*, vol. 57, no. 8, pp. 1831–1834, 2010.

[75] K. R. Paton and A. H. Windle, "Efficient microwave energy absorption by carbon nanotubes," *Carbon*, vol. 46, no. 14, pp. 1935–1941, 2008.

[76] H. C. Shim, J.-W. Song, Y. K. Kwak, S. Kim, and C.-S. Han, "Preferential elimination of metallic single-walled carbon nanotubes using microwave irradiation," *Nanotechnology*, vol. 20, no. 6, p. 065707, 2009.

[77] N. D. Kim, A. Metzger, V. Hejazi, Y. Li, A. Kovalchuk, S.-K. Lee, R. Ye, J. A. Mann, C. Kittrell, R. Shahsavari, *et al.*, "Microwave heating of functionalized graphene nanoribbons in thermoset polymers for wellbore reinforcement," *ACS Applied Materials & Interfaces*, vol. 8, no. 20, pp. 12985–12991, 2016.

[78] M. Zhang, S. Fang, A. A. Zakhidov, S. B. Lee, A. E. Aliev, C. D. Williams, K. R. Atkinson, and R. H. Baughman, "Strong, transparent, multifunctional, carbon nanotube sheets," *Science*, vol. 309, no. 5738, pp. 1215–1219, 2005.

[79] C. Wang, T. Chen, S. Chang, S. Cheng, and T. Chin, "Strong carbon-nanotube–polymer bonding by microwave irradiation," *Advanced Functional Materials*, vol. 17, no. 12, pp. 1979–1983, 2007.

[80] T. Wu, Y. Pan, E. Liu, and L. Li, "Carbon nanotube/polypropylene composite particles for microwave welding," *Journal of Applied Polymer Science*, vol. 126, no. S2, 2012.

[81] S. Poyraz, L. Zhang, A. Schroder, and X. Zhang, "Ultrafast microwave welding/reinforcing approach at the interface of thermoplastic materials," *ACS Applied Materials & Interfaces*, vol. 7, no. 40, pp. 22469–22477, 2015.

[82] M. A. Saed, "A method of moments solution of a cylindrical cavity placed between two coaxial transmission lines," *IEEE Transactions on Microwave Theory and Techniques*, vol. 39, no. 10, pp. 1712–1717, 1991.

[83] E. Vargas, M. L. Pantoya, M. A. Saed, and B. L. Weeks, "Advanced susceptors for microwave heating of energetic materials," *Materials & Design*, vol. 90, pp. 47–53, 2016.

[84] T. Ge, G. S. Grest, and M. O. Robbins, "Tensile fracture of welded polymer interfaces: miscibility, entanglements, and crazing," *Macromolecules*, vol. 47, no. 19,

pp. 6982–6989, 2014.

[85] J. Vogel, M. R. Kessler, S. Sundararajan, and D. Grewell, "Activation energy for diffusion and welding of pla films," *Polymer Engineering & Science*, vol. 52, no. 8, pp. 1693–1700, 2012.

[86] H. Zhang, D. Fortin, H. Xia, and Y. Zhao, "Fast optical healing of crystalline polymers enabled by gold nanoparticles," *Macromolecular Rapid Communications*, vol. 34, no. 22, pp. 1742–1746, 2013.

[87] M. G. Odom, C. B. Sweeney, D. Parviz, L. P. Sill, M. A. Saed, and M. J. Green, "Rapid curing and additive manufacturing of thermoset systems using scanning microwave heating of carbon nanotube/epoxy composites," *Carbon*, vol. 120, pp. 447–453, 2017.

[88] D. Janas and K. K. Koziol, "Rapid electrothermal response of high-temperature carbon nanotube film heaters," *Carbon*, vol. 59, pp. 457–463, 2013.

[89] H. Koerner, G. Price, N. A. Pearce, M. Alexander, and R. A. Vaia, "Remotely actuated polymer nanocompositesstress-recovery of carbon-nanotube-filled thermoplastic elastomers," *Nature Materials*, vol. 3, no. 2, pp. 115–120, 2004.

[90] M. Zhang, S. Fang, A. A. Zakhidov, S. B. Lee, A. E. Aliev, C. D. Williams, K. R. Atkinson, and R. H. Baughman, "Strong, transparent, multifunctional, carbon nanotube sheets," *Science*, vol. 309, no. 5738, pp. 1215–1219, 2005.

[91] F. Marra, L. Zhang, and J. G. Lyng, "Radio frequency treatment of foods: Review of recent advances," *Journal of Food Engineering*, vol. 91, no. 4, pp. 497–508, 2009.

[92] V. Orsat and G. S. V. Raghavan, *17 - Radio-Frequency Processing*. London: Academic Press, 2005.

[93] P. Piyasena, C. Dussault, T. Koutchma, H. Ramaswamy, and G. Awuah, "Radio frequency heating of foods: principles, applications and related propertiesa review," *Critical Reviews in Food Science and Nutrition*, vol. 43, no. 6, pp. 587–606, 2003.

[94] Y. Zhao, B. Flugstad, E. Kolbe, J. W. Park, and J. H. Wells, "Using capacitive (radio frequency) dielectric heating in food processing and preservation–a review," *Journal of Food Process Engineering*, vol. 23, no. 1, pp. 25–55, 2000.

[95] M. Sano, H. Oguma, M. Sekine, Y. Sekiguchi, and C. Sato, "High-frequency welding of glass–fibre-reinforced polypropylene with a thermoplastic adhesive layer: Effects of ceramic type and long-term exposure on lap shear strength," *International Journal of Adhesion and Adhesives*, vol. 59, pp. 7–13, 2015.

[96] J. Leighton, T. Brantley, and E. Szabo, "Rr welding of pvc and other thermoplastic compounds," *Journal of Vinyl and Additive Technology*, vol. 15, no. 3, pp. 188–192, 1993.

[97] S. Avramidis and R. Zwick, "Exploratory radio-frequency/vacuum drying of three bc coastal softwoods," *Forest Products Journal (USA)*, 1992.

[98] G. S. Gazelle, S. N. Goldberg, L. Solbiati, and T. Livraghi, "Tumor ablation with radio-frequency energy," *Radiology*, vol. 217, no. 3, pp. 633–646, 2000.

[99] S. N. Goldberg, M. Ahmed, G. S. Gazelle, J. B. Kruskal, J. C. Huertas, E. F. Halpern, B. S. Oliver, and R. E. Lenkinski, "Radio-frequency thermal ablation with nacl solution injection: effect of electrical conductivity on tissue heating and coagulationphantom and porcine liver study," *Radiology*, vol. 219, no. 1, pp. 157–165, 2001.

[100] C. P. Pavlovich, M. M. Walther, P. L. Choyke, S. E. Pautler, R. Chang, W. M. Linehan, and B. J. Wood, "Percutaneous radio frequency ablation of small renal

tumors: initial results," *The Journal of Urology*, vol. 167, no. 1, pp. 10–15, 2002.

[101] C. Li and R. Dickie, "Bonding adhesive joints with radio-frequency dielectric heating," *International Journal of Adhesion and Adhesives*, vol. 11, no. 4, pp. 241–246, 1991.

[102] C. J. Gannon, P. Cherukuri, B. I. Yakobson, L. Cognet, J. S. Kanzius, C. Kittrell, R. B. Weisman, M. Pasquali, H. K. Schmidt, R. E. Smalley, *et al.*, "Carbon nanotube-enhanced thermal destruction of cancer cells in a noninvasive radiofrequency field," *Cancer*, vol. 110, no. 12, pp. 2654–2665, 2007.

[103] S. J. Corr, M. Raoof, B. T. Cisneros, A. W. Orbaek, M. A. Cheney, J. J. Law, N. C. Lara, A. R. Barron, L. J. Wilson, and S. A. Curley, "Radiofrequency electric-field heating behaviors of highly enriched semiconducting and metallic single-walled carbon nanotubes," *Nano Research*, vol. 8, no. 9, pp. 2859–2870, 2015.

[104] N. C. Lara, A. A. Haider, J. C. Ho, L. J. Wilson, A. R. Barron, S. A. Curley, and S. J. Corr, "Water-structuring molecules and nanomaterials enhance radiofrequency heating in biologically relevant solutions," *Chemical Communications*, vol. 52, no. 85, pp. 12630–12633, 2016.

[105] N. S. Satarkar, D. Johnson, B. Marrs, R. Andrews, C. Poh, B. Gharaibeh, K. Saito, K. W. Anderson, and J. Z. Hilt, "Hydrogel-mwcnt nanocomposites: Synthesis, characterization, and heating with radiofrequency fields," *Journal of Applied Polymer Science*, vol. 117, no. 3, pp. 1813–1819, 2010.

[106] Z. He, N. Satarkar, T. Xie, Y.-T. Cheng, and J. Z. Hilt, "Remote controlled multishape polymer nanocomposites with selective radiofrequency actuations," *Advanced Materials*, vol. 23, no. 28, pp. 3192–3196, 2011.

[107] M. Mehdizadeh, *Microwave/RF applicators and probes: for material heating, sensing, and plasma generation*. William Andrew, 2015.

[108] J. Lee, I. Y. Stein, S. S. Kessler, and B. L. Wardle, "Aligned carbon nanotube film enables thermally induced state transformations in layered polymeric materials," *ACS Applied Materials & Interfaces*, vol. 7, no. 16, pp. 8900–8905, 2015.

[109] F. Qin and C. Brosseau, "A review and analysis of microwave absorption in polymer composites filled with carbonaceous particles," *Journal of Applied Physics*, vol. 111, no. 6, p. 4, 2012.

[110] J. Menéndez, A. Arenillas, B. Fidalgo, Y. Fernández, L. Zubizarreta, E. G. Calvo, and J. M. Bermúdez, "Microwave heating processes involving carbon materials," *Fuel Processing Technology*, vol. 91, no. 1, pp. 1–8, 2010.

[111] C. Gau, C.-Y. Kuo, and H. Ko, "Electron tunneling in carbon nanotube composites," *Nanotechnology*, vol. 20, no. 39, p. 395705, 2009.

[112] E. Grant, B. J. Halstead, *et al.*, "Dielectric parameters relevant to microwave dielectric heating," *Chemical Society Reviews*, vol. 27, no. 3, pp. 213–224, 1998.

[113] R. Neophytou and A. Metaxas, "Characterisation of radio frequency heating systems in industry using a network analyser," *IEE Proceedings-Science, Measurement and Technology*, vol. 144, no. 5, pp. 215–222, 1997.

[114] R. Neophytou and A. Metaxas, "Combined tank and applicator design of radio frequency heating systems," *IEE Proceedings-Microwaves, Antennas and Propagation*, vol. 146, no. 5, pp. 311–318, 1999.

[115] R. Neophytou and A. Metaxas, "Determination of resonant modes of rf heating systems, using eigenvalue analysis," *Journal of Microwave Power and Electromagnetic Energy*, vol. 35, no. 1, pp. 3–14, 2000.

[116] M. Haile, C. B. Sweeney, B. A. Lackey, O. Sarwar, R. Henderson, M. A. Saed, M. J. Green, and J. C. Grunlan, "Ultrafast and highly localized microwave heating in carbon nanotube multilayer thin films," *Advanced Materials Interfaces*, 2017.

[117] R. W. Messler, *Joining of materials and structures: from pragmatic process to enabling technology*. Butterworth-Heinemann, 2004.

[118] M. Alfano, F. Furgiuele, L. Pagnotta, and G. Paulino, "Analysis of fracture in aluminum joints bonded with a bi-component epoxy adhesive," *Journal of Testing and Evaluation*, vol. 39, no. 2, pp. 296–303, 2010.

[119] A. J. Kinloch, *Adhesion and adhesives: science and technology*. Springer Science & Business Media, 2012.

[120] K. Whitfield, "Lotus bonds with aluminum," Apr 2004. Automotive Designs & Production, Available at `https://www.adandp.media/articles/lotus-bonds-with-aluminum`.

[121] V. Rudnev, D. Loveless, and R. L. Cook, *Handbook of Induction Heating*. CRC Press, 2017.

[122] W. Siemens, "Ueber die elektrostatische induction und die verzögerung des stroms in flaschendrähten," *Annalen der Physik*, vol. 178, no. 9, pp. 66–122, 1857.

[123] U. Kogelschatz, B. Eliasson, and W. Egli, "From ozone generators to flat television screens: history and future potential of dielectric-barrier discharges," *Pure and Applied Chemistry*, vol. 71, no. 10, pp. 1819–1828, 1999.

[124] T. C. Corke, C. L. Enloe, and S. P. Wilkinson, "Dielectric barrier discharge plasma actuators for flow control," *Annual Review of Fluid Mechanics*, vol. - 42, no. - 1, pp. 505 – 529, 2010.

[125] S. P. Wilkinson, E. J. Siochi, G. Sauti, T.-B. Xu, M. A. Meador, and H. Guo, "Evaluation of dielectric-barrier-discharge actuator substrate materials," 2014.

[126] H. Ayan, D. Staack, G. Fridman, A. Gutsol, Y. Mukhin, A. Starikovskii, A. Fridman, and G. Friedman, "Application of nanosecond-pulsed dielectric barrier discharge for biomedical treatment of topographically non-uniform surfaces," *Journal of Physics D-Applied Physics*, vol. 42, no. 12, p. 5, 2009.

[127] R. Brandenburg, "Dielectric barrier discharges: progress on plasma sources and on the understanding of regimes and single filaments," *Plasma Sources Science & Technology*, vol. 26, no. 5, 2017.

[128] B. Hergelova, A. Zahoranova, D. Kovacik, M. Stupavska, and M. Cernak, "Polylactic acid surface activation by atmospheric pressure dielectric barrier discharge plasma," *Open Chemistry*, vol. 13, no. 1, pp. 564–569, 2015.

[129] M. Simor, J. Rahel, P. Vojtek, M. Cernak, and A. Brablec, "Atmospheric-pressure diffuse coplanar surface discharge for surface treatments," *Applied Physics Letters*, vol. 81, no. 15, pp. 2716–2718, 2002.

[130] M. Noeske, J. Degenhardt, S. Strudthoff, and U. Lommatzsch, "Plasma jet treatment of five polymers at atmospheric pressure: surface modifications and the relevance for adhesion," *International Journal of Adhesion and Adhesives*, vol. 24, no. 2, pp. 171–177, 2004.

[131] J. E. Seppala, K. E. Hillgartner, C. S. Davis, and K. D. Migler, "Thermography and weld strength characterization of thermoplastic extrusion 3d printing," 2016.

[132] F. Qin and C. Brosseau, "A review and analysis of microwave absorption in polymer composites filled with carbonaceous particles," *Journal of Applied Physics*, vol. 111, no. 6, p. 4, 2012.

[133] Z. Liu, J. Wang, V. Kushvaha, S. Poyraz, H. Tippur, S. Park, M. Kim, Y. Liu, J. Bar, H. Chen, *et al.*, "Poptube approach for ultrafast carbon nanotube growth," *Chemical Communications*, vol. 47, no. 35, pp. 9912–9914, 2011.

[134] S. Poyraz, L. Zhang, A. Schroder, and X. Zhang, "Ultrafast microwave welding/reinforcing approach at the interface of thermoplastic materials," *ACS Applied Materials & Interfaces*, vol. 7, no. 40, pp. 22469–22477, 2015.

[135] F. Irin, B. Shrestha, J. E. Cañas, M. A. Saed, and M. J. Green, "Detection of carbon nanotubes in biological samples through microwave-induced heating," *Carbon*, vol. 50, no. 12, pp. 4441–4449, 2012.

[136] F. Bourdiol, D. Dubuc, K. Grenier, F. Mouchet, L. Gauthier, and E. Flahaut, "Quantitative detection of carbon nanotubes in biological samples by an original method based on microwave permittivity measurements," *Carbon*, vol. 81, pp. 535–545, 2015.

[137] S. Li, F. Irin, F. O. Atore, M. J. Green, and J. E. Cañas-Carrell, "Determination of multi-walled carbon nanotube bioaccumulation in earthworms measured by a microwave-based detection technique," *Science of the Total Environment*, vol. 445, pp. 9–13, 2013.

[138] T. Imholt, C. A. Dyke, B. Hasslacher, J. M. Pérez, D. Price, J. A. Roberts, J. Scott, A. Wadhawan, Z. Ye, and J. M. Tour, "Nanotubes in microwave fields: light emission, intense heat, outgassing, and reconstruction," *Chemistry of Materials*, vol. 15, no. 21, pp. 3969–3970, 2003.

[139] T. Kuang, L. Chang, F. Chen, Y. Sheng, D. Fu, and X. Peng, "Facile preparation of lightweight high-strength biodegradable polymer/multi-walled carbon nanotubes nanocomposite foams for electromagnetic interference shielding," *Carbon*, vol. 105, pp. 305–313, 2016.

[140] S. J. Risch, "Food packaging history and innovations," *Journal of Agricultural and Food Chemistry*, vol. 57, no. 18, pp. 8089–8092, 2009.

[141] S. Azoubel and S. Magdassi, "Controlling adhesion properties of swcnt–pet films prepared by wet deposition," *ACS Applied Materials & Interfaces*, vol. 6, no. 12, pp. 9265–9271, 2014.

[142] A. Saib, L. Bednarz, R. Daussin, C. Bailly, X. Lou, J.-M. Thomassin, C. Pagnoulle, C. Detrembleur, R. Jérôme, and I. Huynen, "Carbon nanotube composites for broadband microwave absorbing materials," *IEEE Transactions on Microwave Theory and Techniques*, vol. 54, no. 6, pp. 2745–2754, 2006.

[143] T. Zhao, C. Hou, H. Zhang, R. Zhu, S. She, J. Wang, T. Li, Z. Liu, and B. Wei, "Electromagnetic wave absorbing properties of amorphous carbon nanotubes," *Scientific Reports*, vol. 4, 2014.

[144] K. Ariga, J. P. Hill, and Q. Ji, "Layer-by-layer assembly as a versatile bottom-up nanofabrication technique for exploratory research and realistic application," *Physical Chemistry Chemical Physics*, vol. 9, no. 19, pp. 2319–2340, 2007.

[145] G. Decher and J. B. Schlenoff, *Multilayer thin films: sequential assembly of nanocomposite materials*. John Wiley & Sons, 2006.

[146] C. Cho, K. L. Wallace, P. Tzeng, J.-H. Hsu, C. Yu, and J. C. Grunlan, "Outstanding low temperature thermoelectric power factor from completely organic thin films enabled by multidimensional conjugated nanomaterials," *Advanced Energy Materials*, vol. 6, no. 7, 2016.

[147] F. Wu, J. Li, Y. Su, J. Wang, W. Yang, N. Li, L. Chen, S. Chen, R. Chen, and L. Bao, "Layer-by-layer assembled architecture of polyelectrolyte multilayers and

graphene sheets on hollow carbon spheres/sulfur composite for high-performance lithium–sulfur batteries," *Nano Letters*, vol. 16, no. 9, pp. 5488–5494, 2016.

[148] G. Rydzek, Q. Ji, M. Li, P. Schaaf, J. P. Hill, F. Boulmedais, and K. Ariga, "Electrochemical nanoarchitectonics and layer-by-layer assembly: From basics to future," *Nano Today*, vol. 10, no. 2, pp. 138–167, 2015.

[149] S. W. Lee, N. Yabuuchi, B. M. Gallant, S. Chen, B.-S. Kim, P. T. Hammond, and Y. Shao-Horn, "High-power lithium batteries from functionalized carbon-nanotube electrodes," *Nature Nanotechnology*, vol. 5, no. 7, pp. 531–537, 2010.

[150] J. A. Lichter, K. J. Van Vliet, and M. F. Rubner, "Design of antibacterial surfaces and interfaces: polyelectrolyte multilayers as a multifunctional platform," *Macromolecules*, vol. 42, no. 22, pp. 8573–8586, 2009.

[151] P. Gentile, M. E. Frongia, M. Cardellach, C. A. Miller, G. P. Stafford, G. J. Leggett, and P. V. Hatton, "Functionalised nanoscale coatings using layer-by-layer assembly for imparting antibacterial properties to polylactide-co-glycolide surfaces," *Acta Biomaterialia*, vol. 21, pp. 35–43, 2015.

[152] M. A. Priolo, K. M. Holder, T. Guin, and J. C. Grunlan, "Recent advances in gas barrier thin films via layer-by-layer assembly of polymers and platelets," *Macromolecular Rapid Communications*, vol. 36, no. 10, pp. 866–879, 2015.

[153] K.-H. Lee, J. Hong, S. J. Kwak, M. Park, and J. G. Son, "Spin self-assembly of highly ordered multilayers of graphene-oxide sheets for improving oxygen barrier performance of polyolefin films," *Carbon*, vol. 83, pp. 40–47, 2015.

[154] M. Leistner, A. A. Abu-Odeh, S. C. Rohmer, and J. C. Grunlan, "Water-based chitosan/melamine polyphosphate multilayer nanocoating that extinguishes fire on polyester-cotton fabric," *Carbohydrate Polymers*, vol. 130, pp. 227–232, 2015.

[155] M. Haile, S. Fomete, I. D. Lopez, and J. C. Grunlan, "Aluminum hydroxide multilayer assembly capable of extinguishing flame on polyurethane foam," *Journal of Materials Science*, vol. 51, no. 1, pp. 375–381, 2016.

[156] Q. Cao, H.-s. Kim, N. Pimparkar, J. P. Kulkarni, C. Wang, M. Shim, K. Roy, M. A. Alam, and J. A. Rogers, "Medium-scale carbon nanotube thin-film integrated circuits on flexible plastic substrates," *Nature*, vol. 454, no. 7203, pp. 495–500, 2008.

[157] B. Kumar, Y. Park, M. Castro, J. Grunlan, and J.-F. Feller, "Fine control of carbon nanotubes–polyelectrolyte sensors sensitivity by electrostatic layer by layer assembly (elbl) for the detection of volatile organic compounds (voc)," *Talanta*, vol. 88, pp. 396–402, 2012.

[158] H. J. Park, K. A. Oh, M. Park, and H. Lee, "Electrical properties and conductivity mapping of thin multilayered films containing different types of carbon nanotubes," *The Journal of Physical Chemistry C*, vol. 113, no. 30, pp. 13070–13076, 2009.

[159] Y. T. Park, A. Y. Ham, and J. C. Grunlan, "High electrical conductivity and transparency in deoxycholate-stabilized carbon nanotube thin films," *The Journal of Physical Chemistry C*, vol. 114, no. 14, pp. 6325–6333, 2010.

[160] Y. T. Park, A. Y. Ham, and J. C. Grunlan, "Heating and acid doping thin film carbon nanotube assemblies for high transparency and low sheet resistance," *Journal of Materials Chemistry*, vol. 21, no. 2, pp. 363–368, 2011.

[161] A. A. Mamedov, N. A. Kotov, M. Prato, D. M. Guldi, J. P. Wicksted, and A. Hirsch, "Molecular design of strong single-wall carbon nanotube/polyelectrolyte multilayer composites," *Nature Materials*, vol. 1, no. 3, pp. 190–194, 2002.

[162] N. I. Kovtyukhova and T. E. Mallouk, "Ultrathin anisotropic films assembled from individual single-walled carbon nanotubes and amine polymers," *The Journal of*

Physical Chemistry B, vol. 109, no. 7, pp. 2540–2545, 2005.

[163] K. J. Loh, J. Kim, J. P. Lynch, N. W. S. Kam, and N. A. Kotov, "Multifunctional layer-by-layer carbon nanotube–polyelectrolyte thin films for strain and corrosion sensing," *Smart Materials and Structures*, vol. 16, no. 2, p. 429, 2007.

[164] M. K. Gheith, T. C. Pappas, A. V. Liopo, V. A. Sinani, B. S. Shim, M. Motamedi, J. P. Wicksted, and N. A. Kotov, "Stimulation of neural cells by lateral currents in conductive layer-by-layer films of single-walled carbon nanotubes," *Advanced Materials*, vol. 18, no. 22, pp. 2975–2979, 2006.

[165] G. P. Moriarty, S. De, P. J. King, U. Khan, M. Via, J. A. King, J. N. Coleman, and J. C. Grunlan, "Thermoelectric behavior of organic thin film nanocomposites," *Journal of Polymer Science Part B: Polymer Physics*, vol. 51, no. 2, pp. 119–123, 2013.

[166] V. Petrov and V. Gagulin, "Microwave absorbing materials," *Inorganic Materials*, vol. 37, no. 2, pp. 93–98, 2001.

[167] Y. T. Park, A. Y. Ham, and J. C. Grunlan, "High electrical conductivity and transparency in deoxycholate-stabilized carbon nanotube thin films," *The Journal of Physical Chemistry C*, vol. 114, no. 14, pp. 6325–6333, 2010.

[168] Y. T. Park, A. Y. Ham, Y.-H. Yang, and J. C. Grunlan, "Fully organic ito replacement through acid doping of double-walled carbon nanotube thin film assemblies," *RSC Advances*, vol. 1, no. 4, pp. 662–671, 2011.

[169] E. Vazquez and M. Prato, "Carbon nanotubes and microwaves: interactions, responses, and applications," *Acs Nano*, vol. 3, no. 12, pp. 3819–3824, 2009.

[170] L. Xiao, Z. Chen, C. Feng, L. Liu, Z.-Q. Bai, Y. Wang, L. Qian, Y. Zhang, Q. Li, K. Jiang, *et al.*, "Flexible, stretchable, transparent carbon nanotube thin film loud-

speakers," *Nano Letters*, vol. 8, no. 12, pp. 4539–4545, 2008.

[171] K. Suzuki, S. Sakakibara, M. Okada, Y. Neo, H. Mimura, Y. Inoue, and T. Murata, "Study of carbon-nanotube web thermoacoustic loud speakers," *Japanese Journal of Applied Physics*, vol. 50, no. 1S2, p. 01BJ10, 2011.

[172] Y. Wei, X. Lin, K. Jiang, P. Liu, Q. Li, and S. Fan, "Thermoacoustic chips with carbon nanotube thin yarn arrays," *Nano Letters*, vol. 13, no. 10, pp. 4795–4801, 2013.

[173] M. Buzaglo, M. Shtein, S. Kober, R. Lovrinčić, A. Vilan, and O. Regev, "Critical parameters in exfoliating graphite into graphene," *Physical Chemistry Chemical Physics*, vol. 15, no. 12, pp. 4428–4435, 2013.

[174] D. Owens, "Mechanism of corona–induced self-adhesion of polyethylene film," *Journal of Applied Polymer Science*, vol. 19, no. 1, pp. 265–271, 1975.

[175] E. Vargas, M. L. Pantoya, M. A. Saed, and B. L. Weeks, "Advanced susceptors for microwave heating of energetic materials," *Materials & Design*, vol. 90, pp. 47–53, 2016.

APPENDIX A

ULTRAFAST AND HIGHLY LOCALIZED MICROWAVE HEATING IN CARBON NANOTUBE MULTILAYER THIN FILMS*

A.1 Overview

Carbon nanotubes have emerged as highly effective materials for microwave absorbing applications due to their high electrical conductivity, large aspect ratio, and high temperature stability against oxidation and corrosion. Ultrathin films are fabricated through layer-by-layer deposition of carbon nanotubes and poly(diallyldimethyl ammonium chloride) from aqueous suspensions under ambient conditions. The number of immersion cycles controls the assembled thickness of these coatings, which provides an effective means of precisely tailoring their electrical properties and thermal response to microwaves. Films of thickness below 200 nm are capable of heating to high temperatures when irradiated with low microwave power, reaching over 130°C in 30 s, at less than 10 W forward power, and rapidly cooling when the power is removed. In contrast to metal thin films, the multilayer carbon nanotube films are active microwave absorbers over a wide range of thickness, making them interesting for applications such as electromagnetic interference shielding and microwave welding.

A.2 Introduction

One of the lesser known properties of carbon nanotubes (CNT) is their exceptional ability to absorb microwave radiation.[132] This peculiar phenomenon has been used for CNT detection, electromagnetic shielding, and CNT growth and cross-linking.[133, 134,

*Reprinted with permission from M. Haile, C. B. Sweeney, B. A. Lackey, O. Sarwar, R. Henderson, M. A. Saed, M. J. Green, J. C. Grunlan. Ultrafast and Highly Localized Microwave Heating in Carbon Nanotube Multilayer Thin Films. Adv. Mater. Interfaces 2017, 4, 1700371. Copyright 2017 John Wiley & Sons, Inc.

135, 136, 137, 138, 139] Due to their versatility, chemical resistance, and absorption efficiencies, even at low loading levels, CNT are excellent materials for microwave-absorbing (MWA) applications. There is growing demand for MWA materials in the fields of radar detection, electromagnetic shielding and electronics. Upon exposure to microwave fields, carbon nanotubes efficiently attenuate incident propagating waves and evolve tremendous heat. This ability to heat as powerful microwave susceptors could be useful in food packaging, where coatings are used to heat and brown foods during microwave cooking. Conventional MWA materials such as aluminum present some health concerns.[140]

Polymer composites incorporating CNT offer a wide range of applications and the possibility of tuning desirable properties, including MWA, by varying nanotube loading. Although many studies have observed the microwave absorbing behavior of CNT bulk nanocomposites, there is little research on how such composites behave when their thickness is on the scale of nanometers.[132, 141, 142, 143] The present work investigates the microwave absorption of thin films composed of anionically stabilized carbon nanotubes and a polycation, deposited layer-by-layer (LbL). LbL assembly involves the bottom-up fabrication of thin films by alternately exposing a substrate to positively and negatively charged materials in aqueous suspensions. Film thickness is controlled by the number of deposition cycles, with each positive and negative layer pair referred to as a bilayer (BL).[144, 145] This is a powerful coating technique, capable of coating many substrates to impart a variety of properties such as energy generation,[146, 147, 148, 149] antimicrobial,[150, 151] gas barrier,[152, 153] and flame retardancy.[154, 155] LbL assembly provides an elegant approach to constructing thin CNT composites on complex substrates with high loading and exceptional electrical conductivity.[156, 157, 158, 159, 160, 161, 162, 163, 164, 165] In the present study, CNT-based films were deposited on polyester (poly(ethylene terephthalate), PET) substrates using LbL assembly under ambient conditions and aqueous suspensions. These sub-300 nm thick coatings provide an

attractive alternative to common MWA coatings, such as magnetic materials or ceramic ferroelectrics, which require more complex processing and add undesirable mass.[166]

A.3 Methods

Multilayer thin films composed of either single-walled (SWNT) or multiwall carbon nanotubes (MWNT), stabilized by deoxycholate, were paired with poly(diallyldimethylammonium chloride) [PDDA] and deposited according to a previously reported procedure.[158] Substrates were first dipped in the polycationic solution containing PDDA, depositing one positively charged layer (Figure A.1).

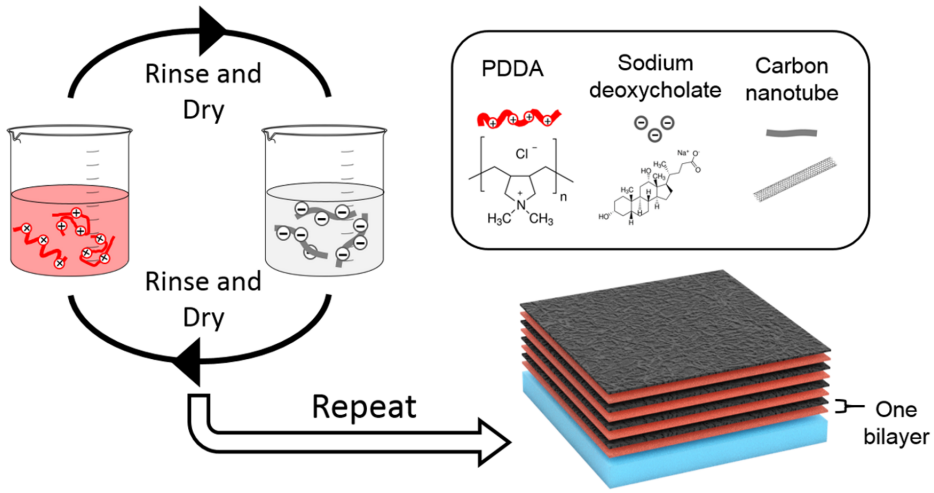

Figure A.1: Schematic of the LbL process for fabricating CNT thin films. The substrate is alternately dipped into a cationic PDDA and an anionic DOC stabilized CNT mixture, with rinsing and drying in between. These steps deposit one bilayer and are repeated to grow a film of desired number of bilayers (i.e., thickness).

After rinsing and drying, the substrate was dipped in the anionic suspension containing CNT and sodium deoxycholate (DOC), depositing one negatively charged layer that was rinsed and dried. This cycle was repeated until the desired number of bilayers was

achieved. PDDA / MWNT and PDDA / SWNT film thicknesses, as a function of the number of bilayers deposited, are shown in Figure A.2.

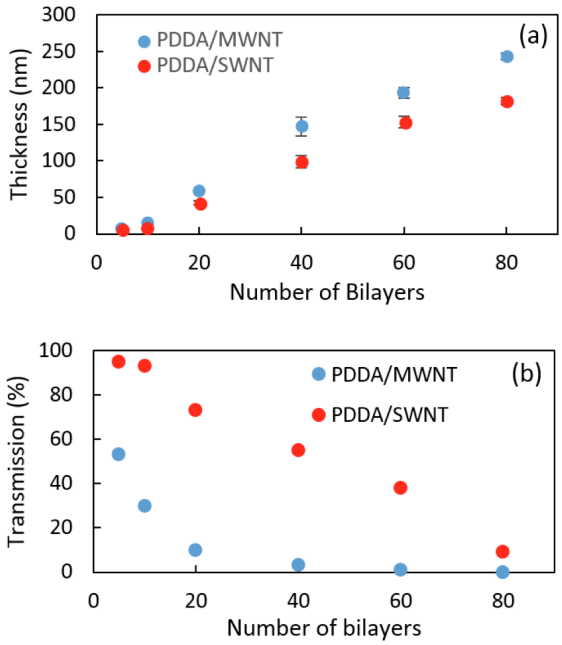

Figure A.2: (a) Film thickness as a function of bilayers deposited as determined by ellipsometry for 5 BL and 10 BL and by profilometry for films of 20 BL or more. (b) Transmission of the films measured by UV-Vis spectrometry, integrated from 400-750 nm.

Both assemblies exhibit linear growth beyond 20 BL, depositing on average 3.1 and 2.3 nm per bilayer, respectively. The growth per bilayer is thinner and nonlinear at 10 BL, which is typical of multilayer thin films as they are establishing a coherent base layer. These recipes were deposited on PET for the microwave experiments, and on silicon for determining thickness via ellipsometry and profilometry.

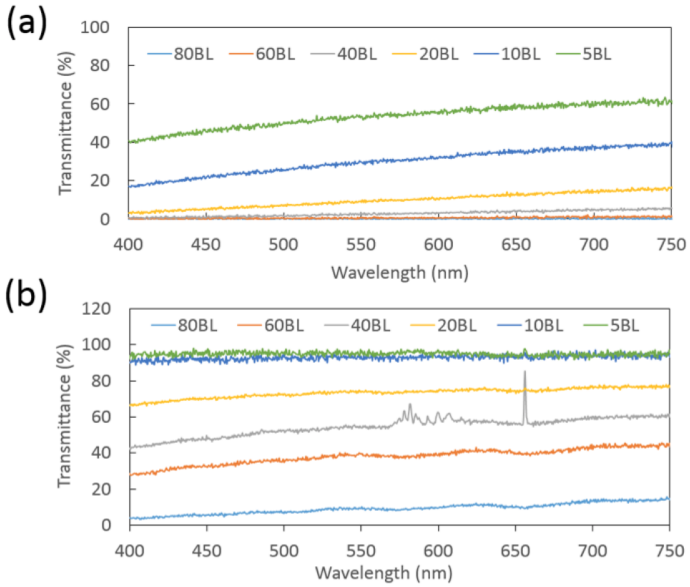

Figure A.3: UV-vis spectra for (a) PDDA / MWNT and (b) PDDA / SWNT films.

Each substrate results in a similar thickness value for a given number of bilayers, as reported in earlier studies.[157, 160, 167, 168] The transparency of these films on PET was measured using UVvis spectroscopy (Figure A.3, Supporting Information). Although both coating recipes had comparable thicknesses, PDDA / MWNT films were generally much more opaque than PDDA / SWNT films, with only 53% transmittance at 5 BL and less than 10% transmittance at 20 BL and above. PDDA / SWNT exhibited over 90% visible light transmittance at 10 BL and below. Very low transmittances of less than 50% were only achieved at 60 BL and above.

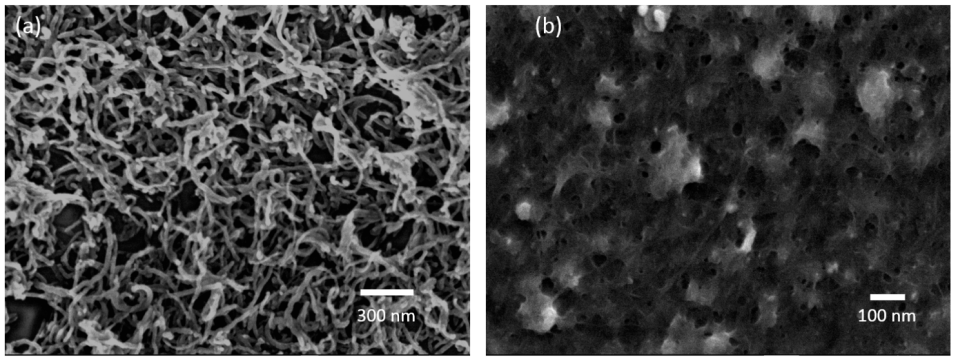

Figure A.4: SEM micrographs of the surface of (a) [PDDA / (MWNT+DOC)]40 and (b) [PDDA / (SWNT+DOC)]40 films.

Differences in nanotube loading were seen between the two CNT types, when scanning electron microscopy was used to observe the surface morphology of the 40 BL films. The PDDA / MWNT film has a considerably rougher surface, due to larger nanotube size, and has a considerably higher concentration of CNT than that of the PDDA / SWNT film (Figure A.4). Thermogravimetric analysis performed on PDDA / CNT delaminated films indicates that the concentration of MWNT and SWNT are 71.6 and 15.6 wt%, respectively (Table S1, Supporting Information).

A.4 Results

In an effort to observe the thermal response of these microwave-absorbing LbL films, coated PET samples were exposed to microwaves in a waveguide assembly while temperatures were recorded using a forward-looking infrared (FLIR) camera (A655sc). Each sample was irradiated for 30 s at 10 W forward power. The heating curves for both SWNT and MWNT films (Figure A.5) demonstrate these films ability to rapidly attenuate microwave energy, converting it to radiant heat.

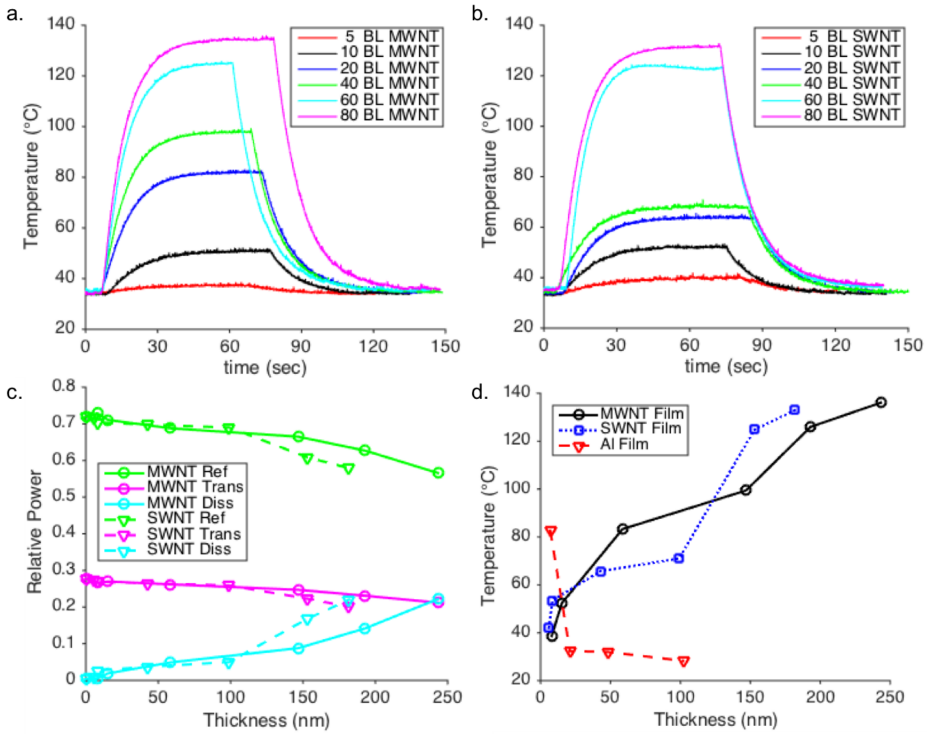

Figure A.5: FLIR temporal plots of the maximum temperature recorded of the a) PDDA / MWNT and b) PDDA / SWNT films during microwave heating at 10 W. c) Relative power curves of the LbL films measured with a two-port coaxial method: reflected, transmitted, and dissipated (absorbed). d) Maximum temperature versus film thickness for MWNT, SWNT, and Al films.

The films rapidly respond to the applied microwave field to reach temperatures over 130°C. This result suggests that the PDDA / CNT films are excellent microwave susceptors, capable of efficiently converting incident microwave power into thermal energy via Joule heating. To better understand the mechanism for this rapid heating response, the microwave absorbing properties of the LbL films on PET were measured using a microwave network analyzer (Agilent E5071C) and a two port coaxial transmission line technique. Round discs of each film thickness were fitted into a coaxial adapter while ensuring that air gaps were eliminated. The network analyzer measures the scattering parameters (S_{11} and S_{21}) by detecting the incident, reflected, and transmitted microwave signals. The ratios

of the reflected and transmitted powers to the incident power are equal to $|S_{11}|^2$ and $|S_{21}|^2$, respectively. The power absorbed by the sample and dissipated as heat, normalized to the incident power, is calculated using Equation (1)

$$\frac{P_{diss}}{P_{inc}} = 1 - |S_{11}|^2 - |S_{21}|^2$$

(1) It is worth noting that the goal of this coaxial measurement is to assess the microwave absorption capabilities of the LbL thin films as a function of thickness. It also demonstrates that such extremely thin films have excellent conductivities, allowing for efficient microwave absorption. The focus here is on microwave power dissipated in the sample rather than reflected power. Designing a specific radar absorber requires minimizing both reflected power and transmitted power using free space experiments. Typical design techniques (e.g., frequency selective structures, metasurfaces, matching layers) using the LbL thin films described here could contribute to optimized radar absorbers.

Higher temperatures are achieved with a higher number of bilayers for both the PDDA / SWNT and PDDA / MWNT assemblies, as predicted by the dissipated power trends observed during coaxial measurements. Notably, the jump in heating rate from 40 to 60 SWNT bilayers is clearly visible in both the relative power measurements (Figure A.5c) and the heating curve in Figure A.5b. The rate at which the samples cool upon the cessation of microwave heating is also remarkable. Cooling of over 100°C in less than 30 s is observed for some samples, indicating that the high temperature is localized in the nanocoating and is quickly transferred to the still-cool substrate and air.

In Figure A.5d, the maximum temperature as a function of film thickness at 30 s of heating is shown for both PDDA / SWNT and PDDA / MWNT films. Both nanotube films display a similarly increasing maximum temperature as film thickness is increased by adding more bilayers. This positive correlation between film thickness and heating re-

sponse appears logical; however, this trend is not typical for MWA thin film susceptors. In order to demonstrate this trend more clearly, we compared the LbL films directly with aluminum thin films, which are commonly used commercially. The thermal response of sputtered aluminum films on PET is plotted for comparison in Figure A.5d. For the aluminum films, a decreasing maximum temperature is observed as film thickness is increased from 7 to 100 nm. This inverse relationship of thickness to heat evolved clearly indicates that the aluminum films are highly reflective to incident microwaves, which means thicknesses below 20 nm are useful as microwave susceptors. In contrast, the PDDA / CNT assemblies have a wide range of thicknesses displaying different heating profiles, providing greater flexibility for tuning their heating response.

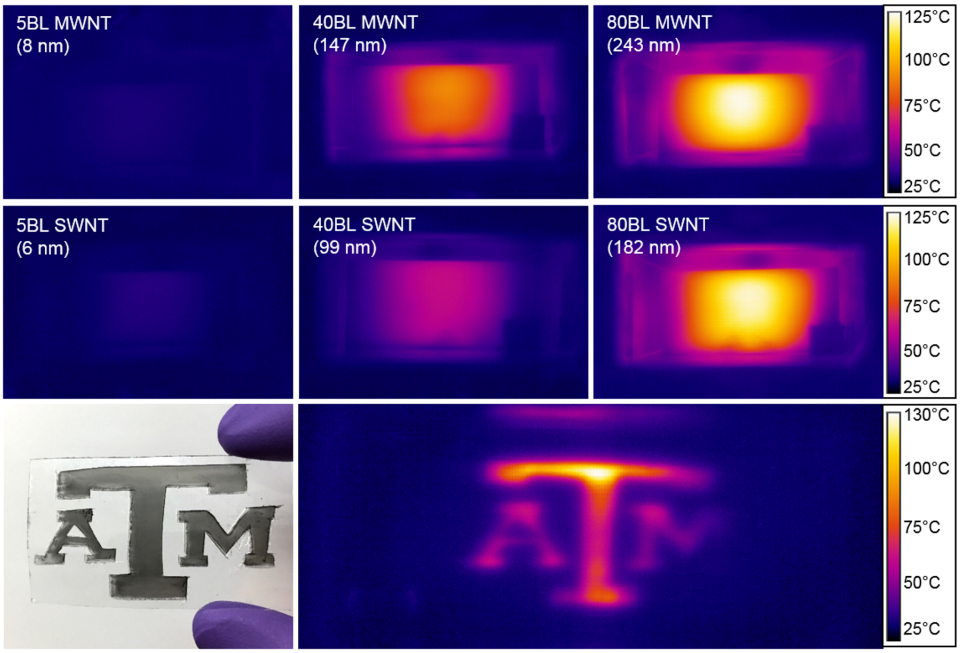

Figure A.6: FLIR images of the MWNT (top) and SWNT-based (middle) LbL films of increasing thickness in the microwave waveguide at 10 W after 30 s of heating. A patterned logo (bottom) made with the carbon nanotube LbL process demonstrates the ability to remotely heat discrete areas of interest.

The spatial heating profiles of the nanotube films were recorded for each sample, as shown in Figure A.6. The electric field, and thus deposited power, in the waveguide are maximized at the center. No difference in the spatial heating profile is observed for the MWNT or SWNT-based films, which suggests the same thermal heating mechanism is responsible in each case. The exact nature of the heating response of CNT and their composites to microwave irradiation is still not well understood. It is generally accepted that incident microwave radiation interacts with carbon nanotubes through electric field coupling, causing the excitation of electrons and electric currents in the film that leads to Joule heating concentrated at resistive lattice defect sites and nanotubenanotube junctions.[169] It is believed that the observed rapid heating and cooling rates stem from CNT-related heating phenomena reported in prior studies. For instance, it is well known that nanotube films can rapidly heat (and cool) from a stimulated direct current (DC) biased audio signal to produce a thermoacoustic effect.[170, 171, 172] The CNT film loudspeakers are able to drive audio signals up to many hundreds of kilohertz due to their low heat capacity and thermal cycling efficiency. Further studies involving wide-band terahertz spectroscopy of CNT films in response to stimulated electric currents, ranging from DC to the gigahertz region, may be helpful in elucidating the exact mechanisms responsible for the rapid heating observed. Regardless of the exact heating mechanism, this work demonstrates the efficient frequency upconversion from S-band (24 GHz) microwave energy to long wave infrared (2040 THz) radiant thermal energy in these carbon nanotube-based thin film assemblies.

A.5 Conclusions

In this report, both SWNT and MWNT-based layer-by-layer films of varying thicknesses were prepared and exposed to microwave energy. The microwave response of these thin CNT films (<300 nm) was outstanding, evolving significant heat in low-power fields. High localized temperatures at the coated surfaces were achieved without appre-

ciably heating the bulk PET substrate. The ease of deposition and process scalability, bolstered by the useful range of film thicknesses that respond to incident microwaves, confirm the utility and advantage these films have over current susceptors materials. By selectively depositing carbon nanotube susceptor films, precise control of material interface temperatures may be realized by an applied external electric field. This spatial temperature control could be used for material bonding, curing, and thermally driven microstructure evolution. Beyond susceptors, these multilayer films could be used in designing radar absorbing structures for stealth vehicles and aircraft, electromagnetic interference (EMI) shielding films, as well as antennas for radio frequency identification tags.

A.6 Experimental

Materials: MWNTs (2030 nm outer diameter and 1030 μm length, C 95 wt%) were provided by Cheap Tubes Inc. (Cambridgeport, VT). SWNTs (0.71.3 nm diameter, (7,6) chirality, C 70 wt%) werepurchased from SouthWest NanoTechnologies (Norman, OK). PDDA (Mw 200 000 g mol1) and DOC were purchased from Sigma-Aldrich (St. Louis, MO). Sulfuric acid (H2SO4, 98%), hydrogen peroxide (H2O2, 30%), and methanol (99.8%) were also purchased from Sigma-Aldrich and used as received. P-doped, single side polished (1 0 0) silicon wafers (University Wafer, South Boston, MA), with a thickness of 500 μm, were used as substrates for elipsometer and profilometer thickness measurements. Films for microwave testing were deposited on 179 μm thick PET film (ST505, Dupont-Teijin) purchased from Tekra (New Berlin, WI). Layer-by-Layer Assembly: All solutions were prepared using 18.2 M Ω cm deionized water. A cationic 0.25 wt% PDDA aqueous solution was prepared by diluting a 20 wt% PDDA solution with deionized water. The anionic solution was prepared by dissolving 0.05 wt% CNTs in deionized water containing 2 wt% DOC, followed by a three-step ultrasonication process to remove large nanotube bundles: 30 min of bath sonication, then 20 min using a tip sonicator, and a final 30 min

of additional bath sonication.[173] Single-side polished (1 0 0) silicon wafers (University Wafer, South Boston, MA) were cleaned by immersion into a piranha solution (4:1 mixture of H2SO4 and H2O2; caution: dangerous oxidizing agent) and sonicating for 30 min, followed by thoroughly rinsing with deionized water and drying with filtered air. 175 μm thick PET (trade name ST505 by DuPont Teijin, Tekra Corp., New Berlin, WI) film was cut to size, followed by rinsing with methanol and water. The cleaned PET substrates were then corona treated with a BD-20C Corona Treater (Electro-Technic Products Inc., Chicago, IL). Corona treatment oxidizes the surface of PET, increasing the surface energy and allowing for positively charged polymers to better adhere.[174] PDDA / CNT assemblies were deposited on a given substrate according to the procedure shown in Figure A.1, using automated rinsing, dipping, and drying. Substrates were immersed into the cationic PDDA solution for 5 min, then rinsed with deionized water and dried using filtered air. Immersion into the DOC-stabilized CNT suspension for 5 min came next, followed by rinsing and drying. These four steps comprised one cycle, yielding one BL. Dipping times were 1 min for every subsequent cycle until the desired number of bilayers was deposited. All samples were stored in a drybox for a minimum of 12 h prior to testing. Film thickness was measured on silicon wafers with a P-6 profilometer (KLA-Tencor, Milpitas, CA) and alpha-SE Ellipsometer (J.A. Woollam Co., Inc., Lincoln, NE). Coated PET samples were mounted on aluminum stubs in preparation for surface images that were acquired with a field emission scanning electron microscope (Model JSM-7500F, JEOL, Tokyo, Japan). Electrical Characterization: DC electrical conductivity of the prepared PDDA / CNT films was measured with a four-point-probe (Signatone HR4-620850FN). Samples 3 cm Œ 5 cm were centered on a four point- probe stand (Lucas Labs) and measured using a differential voltage system (two Keithley 6514 electrometers, Keithley 2000 digital multimeter) with current sourced by a Keithley 6221. Starting at the lowest possible current for each sample, voltage drops were measured at three increasing decades to ensure the linear Ohmic be-

havior of the samples. Volume resistivity (inverse conductivity) was calculated according to the following formula:

$$\rho = \frac{\pi}{ln2} * \frac{V}{I} * t * k$$

where ρ is the resistivity in ω m, V is the voltage drop in volts, I is the current in amperes, t is the thickness in meters, and k is a correction factor for geometry based on the probe spacing to sample diameter. For the sample geometry tested, k is taken to be 0.983 (short sample dimension [3 cm] divided by probe spacing 0.15875 cm and correction applied from lookup table).

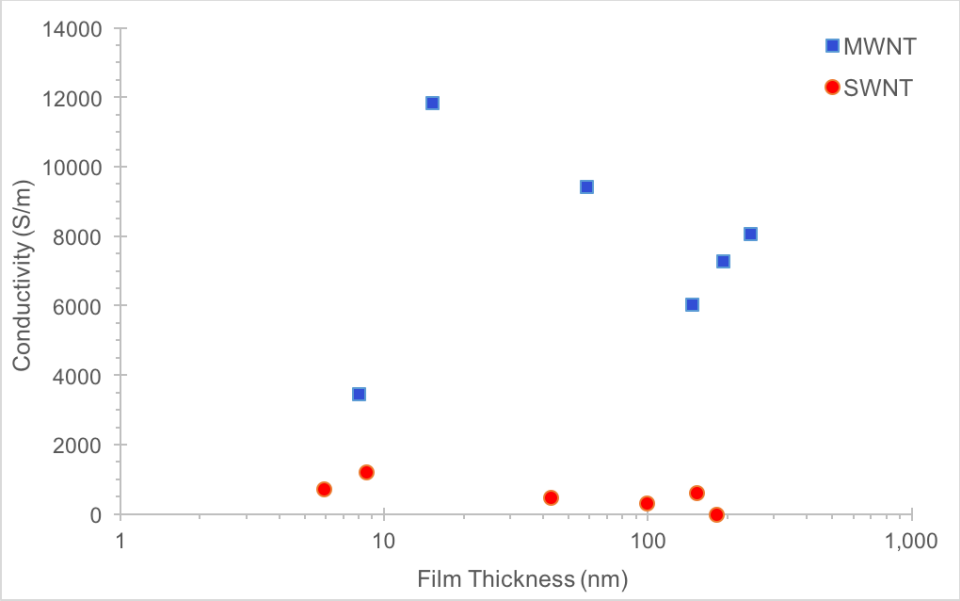

Figure A.7: DC conductivity measurements, made with a 4-point probe, for MWNT (square marker) and SWNT-based (circle marker) films as a function of thickness.

Results are plotted in Figure A.7. Microwave dielectric properties of the films were measured using a coaxial technique using a microwave network analyzer (Agilent E5071C) that measures the scattering (S) parameters of two-port networks. The measurement tech-

nique uses a disk shaped sample sandwiched between two transmission lines. The parts of the dielectric disk that are outside the coaxial lines are completely enclosed with a conductor. For convenience, two 7 mm Amphenol Precision Connectors (APC-7) were used as the sample holder. The APC-7 connector has an inner conductor diameter of 3 mm, outer conductor diameter of 7 mm, and flange diameter of 14.8 mm. The films to be measured were prepared by laminating both faces with clear packing tape to insulate and protect the surfaces from the coaxial sample holder. A disc punch was used to punch out samples 14.8 mm in diameter, ensuring the films would fit precisely in the sample holder with minimal air gaps at the edges. All power measurements were carried out at 2.45 GHz to match the frequency used for the waveguide heating experiments. Microwave Heating: PDDA / CNT films were heated in a rectangular waveguide (AMCSS-284-F/F-12-B, AMC LLC) powered by a solid state microwave source (GMP 150, Opthos Instruments Inc.) operated at 2.45 GHz at various power levels. Spatial temperature measurements were carried out using an infrared camera system (A655sc, FLIR Systems Inc.) calibrated to measure temperatures of a sample located behind a brass mesh covering the open end of the waveguide.[175] The samples were inserted into the waveguide at the location of a maximum of the electric field standing wave, 57.9 mm from the brass mesh. This ensures the samples were exposed to the strongest and most uniform electric field in the waveguide. A diagram of the instrument setup is shown in Figure A.8.

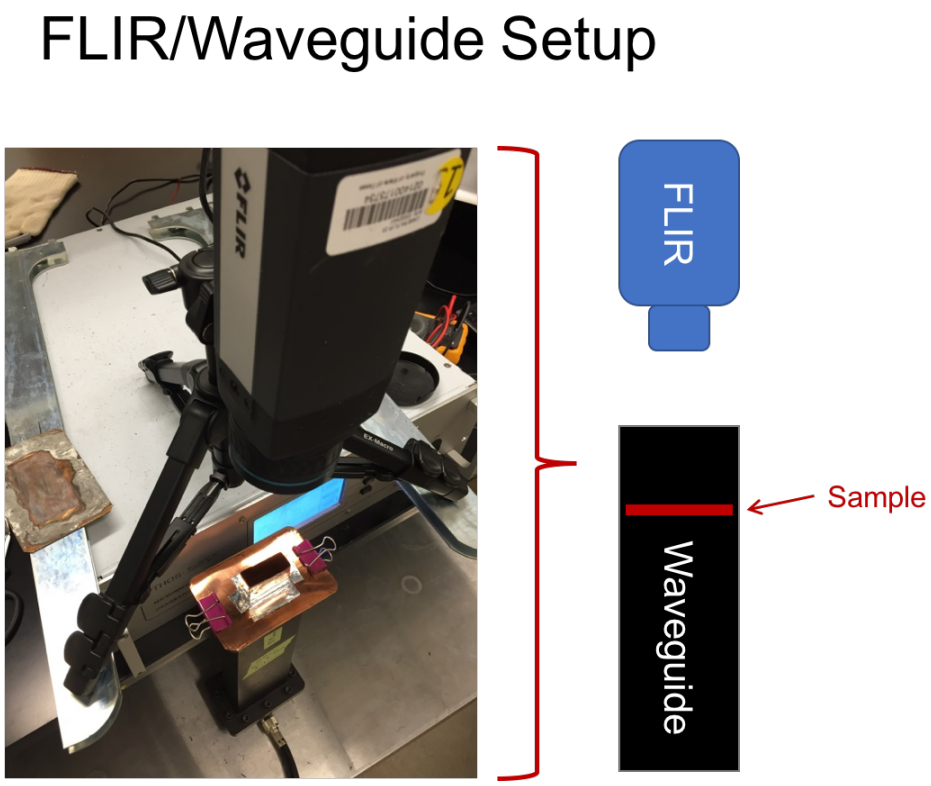

Figure A.8: FLIR and waveguide heating setup. The waveguide (rectangular WR284, AMC Microwave Inc.) is connected with coaxial cable to the solid state microwave source. The FLIR camera views the sample from above. The sample is placed on a Teflon block suspended at the maximum electric field intensity.

Various power levels were used to heat the samples and their temperature response was recorded using the FLIR supplied software (ReseachIR MAX). Aluminum-coated films were deposited onto PET using a PVD 75 Metal Sputter (Lesker Company, Jefferson Hills, PA). Thickness of aluminum films was determined by profilometry of coated silicon concurrently sputtered alongside PET samples.